

AD-A207 198

# TWO-PHOTON ABSORPTION CHARACTERIZATION OF HgCdTe

DTIC  
ELECTE  
APR 07 1989  
S D

DISTRIBUTION STATEMENT A  
Approved for public release  
Distribution Unlimited

Interim Annual Report  
Prepared for the U.S. Army  
Night Vision and Electro-Optics  
Laboratory  
Contract #DAAB07-87-C-FO94  
by  
Professor Chris L. Littler  
Department of Physics  
University of North Texas *State*  
Denton, Texas

89 4 07 061

REPORT DOCUMENTATION PAGE				Form Approved OMB No 0704-0188	
1. REPORT SECURITY CLASSIFICATION Unclassified			1b. RESTRICTIVE MARKINGS		
2a. SECURITY CLASSIFICATION AUTHORITY			3. DISTRIBUTION/AVAILABILITY OF REPORT Approved for public release: Distribution is Unlimited		
2b. DECLASSIFICATION/DOWNGRADING SCHEDULE			5. MONITORING ORGANIZATION REPORT NUMBER(S) NA		
4. PERFORMING ORGANIZATION REPORT NUMBER(S) NA			7a. NAME OF MONITORING ORGANIZATION Center for Night Vision and Electro-Optics		
6a. NAME OF PERFORMING ORGANIZATION Univ. of North Texas		6b. OFFICE SYMBOL (if applicable) AMSEL-RD-NV-IT		7b. ADDRESS (City, State, and ZIP Code) ATTN: AMSEL-RD-NV-IRT Fort Belvoir, VA 22060-5677	
6c. ADDRESS (City, State, and ZIP Code) Fort Belvoir, VA 22060-5677			9. PROCUREMENT INSTRUMENT IDENTIFICATION NUMBER DAAB07-87-C-F094		
8a. NAME OF FUNDING/SPONSORING ORGANIZATION CNVEO		8b. OFFICE SYMBOL (if applicable) AMSEL-RD-NV-IT		10. SOURCE OF FUNDING NUMBERS	
				PROGRAM ELEMENT NO. 661102A	PROJECT NO. 1L16110 2A31B
				TASK NO H0	WORK UNIT ACCESSION NO 007-CJ
11. TITLE (Include Security Classification) Two Photon Characterization					
12. PERSONAL AUTHOR(S) David G. Seiler					
13a. TYPE OF REPORT Interim Annual		13b. TIME COVERED FROM 8/87 TO 8/88		14. DATE OF REPORT (Year, Month, Day) 1/89	
15. PAGE COUNT 94					
16. SUPPLEMENTARY NOTATION					
17. COSATI CODES			18. SUBJECT TERMS (Continue on reverse if necessary and identify by block number)		
FIELD 17	GROUP 05	SUB-GROUP	Defect characterization; Magneto-Optical measurements; Two Photon Spectroscopy; Narrow band gap semiconductors. II-VI compounds.		
19. ABSTRACT (Continue on reverse if necessary and identify by block number)					
<p>Magneto-Optical measurements of <math>Hg_{1-x}Cd_xTe</math> alloys have provided a new means of studying impurities and defects in this important II-VI material. Two-photon magnetoabsorption (TMPA) has been used to accurately determine the temperature dependence of the energy gap of various HgCdTe alloys, revealing behavior that deviates from currently accepted models. In addition, magneto-optical techniques have been used to detect the presence of both shallow and deep impurities/defects and accurately determine their activation energies, thus providing information necessary for understanding the electrical and optical properties of the material.</p> <p><i>Keywords:</i></p>					
20. DISTRIBUTION/AVAILABILITY OF ABSTRACT <input type="checkbox"/> UNCLASSIFIED/UNLIMITED <input checked="" type="checkbox"/> SAME AS RPT. <input type="checkbox"/> DTIC USERS			21. ABSTRACT SECURITY CLASSIFICATION Unclassified		
22a. NAME OF RESPONSIBLE INDIVIDUAL Frederick F. Carlson			22b. TELEPHONE (Include Area Code) 703-664-5036		22c. OFFICE SYMBOL AMSEL-RD-NV-IT

**Annual Report**

August 28, 1987 - August 27, 1988

First Year (Twelve Months)

Contract DAAB07-87-C-FO94

With the U.S. Army Night Vision and Electro-Optics Center

Fort Belvoir, Virginia 22060-5677

Contract Monitor: Mr. Fred Carlson



**"Two-Photon Absorption Characterization"**

**Principal Investigators:**

Dr. Chris L. Littler

Dr. David G. Seiler

Department of Physics

University of North Texas

Denton Texas, 76203

Accession For	
NTIS	CRA&I <input checked="" type="checkbox"/>
DTIC	TAB <input type="checkbox"/>
Unannounced	<input type="checkbox"/>
Justification	
By	
Distribution	
Availability	
Dist	Available for Special
A-1	

The views, opinions, and/or findings contained in this report are those of the authors and should not be construed as an official Department of the Army position, policy, or decision, unless designated by other documentation.

## **TWO-PHOTON ABSORPTION CHARACTERIZATION OF HgCdTe**

<b>I. Summary of Program Goals</b>	<b>2</b>
<b>II. Discussion of Tasks</b>	
Task (a). Experimental Facility	3
Task (b). Investigation of Two-Photon Absorption	4
Task (c). Identification of Impurity Levels	6
Task (e)	
Task (f) Investigation of Lifetimes	9
<b>III. References</b>	<b>12</b>
<b>IV. Tables and Figures</b>	<b>13</b>
<b>V. Appendix</b>	<b>41</b>

Annual Report

August 28, 1987 - August 27, 1988

First Year(Twelve Months)

Contract DAAB07-87-C-FO94

"Two-Photon Absorption Characterization"

Principal Investigators:

Dr. Chris L. Littler

Dr. David G. Seiler

University of North Texas

The principal goal of the program is to develop two-photon absorption spectroscopy(TPAS) as a tool for characterizing HgCdTe, to identify impurity and defect levels in the forbidden energy gap of HgCdTe, and determine the effect of these impurities on the lifetime of minority carriers by the use of time-resolved spectroscopic studies. The specific tasks to be started in the first year from section 3.0 of the statement of work are:

- a. Build an experimental facility specifically designed for the characterization of HgCdTe, with special emphasis given to infrared laser systems, variable low temperature apparatus, and high magnetic fields.
- b. Investigate TPAS at energies below the bandgap for HgCdTe and identify all observable sub-band gap energy levels.
- c. Identify impurity related energy levels and correlate with specific impurities.
- e. Investigate the time-resolved behavior of HgCdTe to two-photon absorption excitation. Use information obtained to estimate the "generic lifetime" of the charge carriers.
- f. Analyze "lifetime" data to determine surface and bulk recombination probabilities.

Referring to the interim Time Phase Task Schedule (Table 1) included in this report, it can be seen that all first year tasks have been started on time and, good progress is being made in each task. Specifically, the highlights of the last year's progress is summarized by task as follows:

**Task (a)** An experimental facility specifically designed to study HgCdTe has been completed and is fully operational. A schematic diagram of the experimental layout is detailed in Figure 1. The specific equipment purchased and installed during the first year were: an Apollo model 150 CO<sub>2</sub> laser, an Apollo model 125 far infrared laser system, and a 120 kG superconducting solenoid mounted in a Janis 16CNDT supervaritemp dewar. The solenoid has magnetic field modulation coils capable of producing AC magnetic fields of  $\pm 500$  gauss peak-to-peak. The CO<sub>2</sub> laser is grating tunable and is capable of producing continuous wave powers greater than 100 watts for any of the available laser frequencies. The laser can be operated in any one of four modes: continuous wave, electronically pulsed, electronically chopped, and Q-switched. The variable temperature cryostat containing the superconducting solenoid is capable of producing sample temperatures between 1.8 K and 300 K, controllable to  $\pm 0.5$ K. In addition, during the first year a Spex model 1404 0.85 meter double spectrometer was purchased and installed. This piece of equipment will be used during the second year of the program to study two-photon-induced luminescence from HgCdTe samples.

Sample holders for the low temperature cryostat have been designed to allow for rapid sample change and cooldown. The sample is mounted in an integrated circuit chip carrier which is non-magnetic and mates to a socket permanently attached to the sample holder. A detailed description of the carrier is shown in Figure 2. Twelve leads are available to bring out the sample signals. This flexibility permits the measurement of several samples during a single low temperature run.

During the first quarter, all features of the UNT Infrared Laser and High Magnetic Field Facility were put into working order. The magnetic field modulation coils were tested by studying the Shubnikov de-Haas effect in a number of different samples: (1) GaSb, (2) MBE-grown HgTe, and (3) superlattices of HgCdTe. The results of the HgTe study were reported at the 1987 U. S. Workshop on the Physics and Chemistry of HgCdTe and in the two published articles<sup>1,2</sup>.

**Task (b)** Two-photon magnetoabsorption (TPMA) spectra have been obtained for the first time for samples of p- and n-type HgCdTe. A variety of samples with x-values between 0.24 and 0.31 have been studied and the results analyzed to extract the energy band structure and temperature dependence of the energy gap of HgCdTe. Detailed information on the samples studied during the first year is given in Table II. Figure 3 shows typical TPMA spectra (high field region) obtained as a function of laser wavelength for sample #1, along with one-photon (OPMA) and impurity (IMA) data seen at lower magnetic fields. The two strong TPMA peaks seen here between 80 kG and 120 kG have also been observed in every sample of HgCdTe studied this year and are identified as the two photon transitions denoted by L1 and L2 in Table III. Theoretical calculations of transition energies versus magnetic field are shown in Figure 4 for each of the magneto-optical effects mentioned above. The magnetic field induced or Landau level energies were calculated using a four level energy band model and the following set of energy band parameters<sup>3</sup>:  $E_p = 19$  eV,  $\Delta = 1.0$  eV,  $\gamma_1 = 3.3$ ,  $\gamma_2 = 0.1$ ,  $\gamma_3 = 0.9$ ,  $\kappa = -0.8$ ,  $F = -0.8$ ,  $q = 0.0$ , and  $N_1 = 0.0$ , and the appropriate one- or two-photon selection rules. The value of the energy gap ( $E_g$ ) was determined by fitting the theoretical energies to the OPMA and TPMA data using  $E_g$  as an adjustable parameter. The transition energy for TPMA are given by

$$2\hbar\omega = E_c^{a,b}(n_c, B) - E_v^{a,b}(n_v, B) \quad (1)$$

where  $\hbar\omega$  is the photon energy of the laser,  $E_c^{a,b}(n_c, B)$  represents the energies of the conduction band Landau Levels of spin state a or b,  $E_v^{a,b}(n_v, B)$  represents the energies of the valence band Landau levels, n is the Landau quantum number, B is the magnetic field, and the zero of energy is defined at the top of the valence band. For a consistent description of both the OPMA and TPMA data, a 2 meV exciton binding energy was added to the OPMA data. The TPMA selection rule dependence was tested by obtaining TPMA spectra using left circularly ( $\sigma_L$ ) and right circularly polarized ( $\sigma_R$ ) laser light. An example of the spectra is shown in Figure 5. According to second order perturbation theory, two-photon absorption transition probabilities are proportional to the

product of two matrix elements. In the "intra-interband" transition picture, one matrix element represents an intraband transition while the other represents an interband one. Thus, two-photon absorption is predicted to be strongest using  $\sigma_L$  polarized light since the controlling intraband transition is cyclotron resonance. It is seen in Figure 5 that the TPMA selection rule  $\Delta n = +2$  for  $\sigma_L$  polarization is confirmed by the clear dependence of the TPMA spectra on polarization.

Finally, the broad peak (long arrows) observed on the high field side of the last OPMA peak is identified as arising from electron transitions from a shallow acceptor to the lowest conduction band Landau level. Comparison of this IMA data with the theoretical predictions yields an acceptor binding energy of 9.8 meV. This energy is consistent with that for Cu acceptors in HgCdTe<sup>4</sup>. A major significance of this result is that IMA spectra provides a new means of detecting the presence of compensating acceptors in n-type material.

Figures 6, 8, 10, 11, and 13 show examples of TPMA spectra obtained for sample #2, #3, #4, #5, and #6, respectively. In each case the two strong TPMA resonances L1 and L2 are observed. In addition, samples #1, #2, and #6 show weak TPMA structure whose identification are given in Table III. Figures 7, 9, and 14 show the comparison of theoretical predictions to the TPMA data for samples #2, #3, and #6. This comparison for samples #4 and #5 are shown in Figure 12, along with a summary of other results. In each case the TPMA data provides a very accurate measure of the energy gap of each sample. As a result, TPMA measurements have been used this year to investigate the temperature dependence of the energy gap of HgCdTe. Examples of the temperature dependence of the TPMA spectra are shown for sample #1 in Figure 15 and sample #3 in figure 16. Also shown in Figure 15 is the temperature dependence of the OPMA spectra. The magnetic field positions of the two strong TPMA resonances are seen to be relatively independent of temperature between 2K and 15K, then shift to lower magnetic field at higher temperatures. The data was analyzed by calculating the TPMA transition energies using the 4-band model with  $E_g$  as the only parameter adjusted in order to fit the experimental data. The resulting values of  $E_g$  versus temperature for samples #1, #3, #4, #5, and #6 are shown in Figure 17 and are compared to the empirical predictions of Hansen, Schmidt, and Casselman (HSC)<sup>5</sup>. The TPMA energy gap result is



seen to be relatively independent of temperature below 15K, increases more rapidly than the predictions of HSC between 20K and 100K, and finally above 100K has a slope that can be explained by the HSC relationship. Thus, TPMA measurements have allowed the first observation of the "flattening" of  $E_g$  vs T in HgCdTe at temperatures less than 20K.

Preprints of the TPMA results presented above are appended to this report. They are entitled "New Laser-Based Magneto-Optical Studies of HgCdTe Alloys" (to be published in Solid State Communications) and "Nonlinear Magneto-Optical Spectroscopy of HgCdTe by Two-Photon Absorption Techniques" (to be published in the Journal of Vacuum Science and Technology).

**Task (c)** As discussed above, the first observation of impurity magnetoabsorption (IMA) in HgCdTe has also been made during the course of this year. Specific levels have been measured and are listed in Table II. Specifically, as discussed in Task (b), electron transitions from a shallow acceptor level to the lowest conduction band Landau level have been observed (see Figure 3, long arrows) and theoretically described (see Figure 4). The transition energies for one photon IMA are given by

$$\hbar\omega = E_c^{a,b}(n_c, B) - E_i, \quad (2)$$

where  $\hbar\omega$  is the laser photon energy and  $E_i$  is the binding or activation energy of the impurity state, as referenced to the top of the valence band. As  $B \rightarrow 0$  kG,  $E_c^{a,b}(n_c, B) \rightarrow E_g$  and the zero field intercept equals  $E_g - E_i$ . For the IMA shown in Figure 3 this analysis yields 9.8 meV for the acceptor binding energy. This identification has been confirmed by the temperature dependence of the IMA peak and the time-resolved behavior of the photoconductive response. Thus, IMA techniques provide a new way to detect the presence of compensating or residual acceptors in n-type material.

Figure 18 shows the wavelength dependence of the TPMA resonances for sample #5. This figure again shows the presence of the two strong TPMA resonances, as indicated by the short arrows. However, at higher magnetic fields, weaker and broader resonances are seen, as indicated

by the long arrows. These resonances cannot be theoretically described by TPMA processes; instead they can only be interpreted as resulting from electron transitions from near mid-gap levels to the lowest conduction band Landau level. The theoretical description for these transitions using Equation 2 is given in Figure 19 (shown also in Figure 12). The transition energy versus magnetic field plots show excellent agreement between the experimental data and the calculated transition energies, yielding activation energies of 94 and 100 meV for the two near-midgap levels.

Finally, new magneto-oscillatory structure has been observed which does not shift with incident photon energy and is thus not magneto-optical in nature. Examples of this structure are seen for sample #1 in Figure 3 and Figure 20. These oscillations are observed only in the photoconductive response at high laser intensities and exhibit a periodicity with inverse magnetic field. Given these features, the following models to explain the data were considered:

- (1) Two-dimensional Shubnikov-de-Haas oscillations
- (2) Impurity-assisted magnetophonon oscillations.
- (3) Magneto-impurity oscillations.

Each of these models and experimental support (or lack thereof) for each is discussed below.

(1) Shubnikov-de-Haas (SdH) oscillations for a two-dimensional electron gas (2DEG) resulting from an electron accumulation layer have been frequently seen on samples of n-HgCdTe. The 2-D layer is usually the result of a passivating oxide layer at the surface of the sample which possesses a large positive fixed charge. However, if the 2DEG exists, the SdH oscillations should be seen in the dark magnetoresistance of the sample since its existence does not depend in any way on optical excitation. In addition, the periodicity (in  $\text{kG}^{-1}$ ) of the SdH oscillation depends strongly on the concentration of the 2DEG thus the sample surface preparation and/or passivation. However, the magneto-oscillatory structure observed has been seen only in the presence of photoexcitation and in a number of samples of widely varied surface preparation and passivation. Thus, there is not a strong case at this point for believing that the structure observed is SdH oscillations arising from a

2DEG.

(2) Impurity-assisted magnetophonon (IMP) oscillations, usually observed under hot electron conditions, arise from a process whereby an electron emits a longitudinal optical (LO) phonon and becomes bound to an impurity. The resonance condition for such a process is given by<sup>6</sup>,

$$n\hbar\omega_c + E_i = \hbar\omega_0, \quad (3)$$

where  $\omega_c$  is the cyclotron frequency and  $\omega_0$  is the LO phonon energy. The hot electrons in this process can be created either by high electric fields in the sample or by strong optical excitation. The oscillatory structure arising from such a process would be periodic in inverse magnetic field and would occur whenever

$$n\hbar\omega_c = \hbar\omega_0 - E_i = \Delta E. \quad (4)$$

Assuming that the impurity involved is the same that was responsible for the IMA resonance seen at higher fields in sample #1 (whose binding energy is 9.8 meV) and, using 17.3 meV for the LO phonon energy<sup>7</sup>, a resonance should occur whenever  $n\hbar\omega_c$  equals  $\Delta E$  or 7.5 meV. From the analysis of the data shown in Figure 20,  $\Delta E$  is  $5.5 \pm 1$  meV, somewhat below the predicted value of 7.5 meV. However, the match of predictions to theory is close enough that the IMP model cannot be ruled out at this time.

(3) Magneto-impurity (MI) oscillations have been typically observed in wide gap semiconductors such as GaAs, InP, and Ge. These oscillations result from an inelastic scattering process whereby a free carrier resonantly exchanges energy with a second carrier bound to a shallow impurity. The MI oscillations are observed under similar conditions to those of IMP oscillations and occur whenever<sup>6</sup>

$$n\hbar\omega_c = E_2 - E_1, \quad (5)$$

where  $E_2$  and  $E_1$  are the energies of two impurity states of the same impurity, one of which is usually the ground state. If a very simple hydrogenic model for the excited states of the acceptor impurity is adopted then oscillations would occur whenever  $\hbar\omega_c$  equals 7.3 meV. This prediction is somewhat closer to the observed  $\Delta E$  of 5.5 meV for the oscillations shown in Figure 20.

At this point it is difficult to confirm or rule out either the IMP or the MI model. Further experimental and theoretical work will focus on ways to delineate between the two mechanisms.

**Task (e) and (f)** Work in these two tasks has proceeded in two areas: (1) The development of a novel method to determine the true minority carrier lifetime in p-type narrow gap materials, and (2) the investigation of laser-induced impurity absorption processes and carrier dynamics in p-type material. Work in the second area is aimed primarily at determining the individual absorption and recombination coefficients of impurity and defect levels along with their respective concentrations. Progress in these areas is summarized below:

During the first year a novel method was developed to determine minority carrier lifetimes. The basis for the method about to be discussed is a technique recently developed at UNT to obtain information about multi-carrier semiconductor systems (see Applied Physics Letters, Volume 51, p. 1916, 1987; a reprint of this article is also appended). The technique employs the measurement and subsequent analysis of the magnetoconductivity (MC) tensor components  $\sigma_{xx}$  and  $\sigma_{xy}$  of a semiconductor. By analyzing the MC tensor components it was shown that the carrier concentration and mobility of both majority and minority carriers could be easily obtained. Although the method was first applied to multi-carrier analysis in dark, thermal equilibrium conditions, it was shown this year to be applicable to the analysis and study of photo-excited carriers under laser excitation (i.e., nonequilibrium) conditions. This permitted the extraction of "true" minority carrier lifetimes in p-type semiconductors.

To test the concept out, samples of p-InSb were first used. Figure 21 shows the  $\sigma_{xy}$  component of the MC tensor versus magnetic field under dark, thermal equilibrium conditions at

four different temperatures. At lower temperatures (77 and 100K), only heavy and light holes can be seen, as expected. However, at 135K, the presence of a relatively small concentration of intrinsic electrons (minority carriers) can be detected. At 160K, however, the number of intrinsic electrons thermally excited across the gap completely dominates the transport of the sample at low magnetic fields. Details of the analysis are given in the appended Applied Physics Letter.

A Tektronix waveform digitizer was used to capture the transient behavior of  $\sigma_{xy}$ , allowing the effect of a  $\text{CO}_2$  laser pulse, (98 nsec full width at half maximum) incident on the sample, to be observed. An example of the effect of laser excitation on  $\sigma_{xy}$  is shown in Figure 22. The laser wavelength (9.25  $\mu\text{m}$ ) was chosen such that two-photon excitation was present and thus the TPMA-generated minority carriers (electrons) could be observed and studied. Figure 22a shows the following four sets of transient data and corresponding theoretical curves: (1) in the dark, at a time before the laser pulse is incident on the sample, (2) at the peak of the signal, at a time 325 ns after the start of the laser pulse, (3) 435 nsec after, and (4) 515 nsec after. Note from Figure 23 that the peak of the signal occurs approximately at the end of the laser pulse. Figures 22b and 22c show how the MC tensor analysis can be used to extract the time-resolved behavior of the minority carrier concentration. Thus, the magnetophotoconductivity (MPC) technique can provide directly the number of photoexcited minority carriers  $\Delta n$  as a function of time and, as a result, the true minority carrier lifetime.

Figure 23 shows the number of photoexcited electrons  $\Delta n$  as a function of time for  $T = 100$  and 160K obtained using the MPC technique. Note that the technique is extremely sensitive to the number of minority carrier electrons (detection limit  $\simeq 4 \times 10^{10} \text{ cm}^{-3}$  electrons in the presence of  $\simeq 2 \times 10^{14} \text{ cm}^{-3}$  holes at 100K). For comparison purposes, the time variation of the photoconductive (PC) response is also plotted. It is seen that the PC response possesses a single stage decay for  $T = 100\text{K}$  and a two-stage decay for  $T = 160\text{K}$ . The electron lifetime at 100K is seen to be much shorter than the lifetime implied by the PC response and follows the first stage of the two-stage PC decay for  $T = 160\text{K}$ . At 100 K, the PC response is known to be dominated by impurity absorption, creating only holes with a long lifetime. The presence of the much smaller concentration of two-

photon created electrons can only be detected by the more sensitive MPC method. At 160K, intrinsic conduction dominates and hence the first stage decay of the PC response is due to a decrease in the number of minority-carrier electrons, in agreement with the results of the MPC analysis. Further details of this work are given in a preprint of a article submitted to Applied Physics Letters, which is appended to this report.

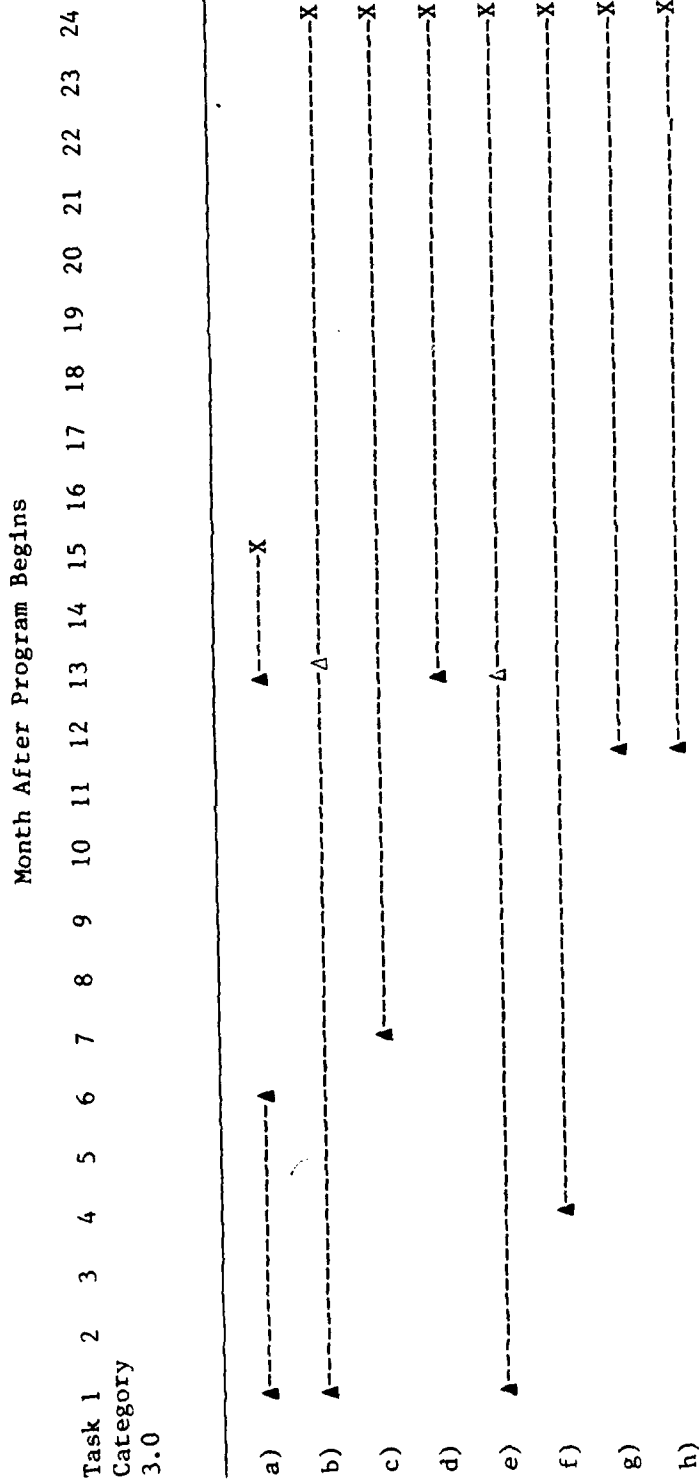
Work is continuing on the analysis of p-HgCdTe samples by the same method. Figure 24 shows the PC response of a p-HgCdTe ( $x=0.307$ ) sample at various temperatures. Complex, two-stage behavior is seen, and at low temperatures, the hyperbolic nature of the transient response indicates that TPMA processes are present. Finally, carrier lifetimes resulting from two-photon excitation have been studied in n-type material. Initial results indicate that the carrier lifetime exhibits resonant behavior at magnetic field positions where resonant TPMA occur.

In summary, significant progress has been made in each category of the first year tasks. All of the progress represents first observations of each type of phenomena, whether magneto-optical, magnetotransport, or lifetime related. The TPAS technique has been sufficiently developed in the first year to assure success in the continuing and new second year tasks of the program.

**References:**

1. R. J. Justice, D. G. Seiler, W. Zawadzki, R. J. Koestner, M. W. Goodwin, and M. A. Kinch, J. Vac. Sci. Technol. A6, 2779 (1988).
2. R. J. Justice, D. G. Seiler, W. Zawadzki, R. J. Koestner, and M. W. Goodwin, Appl. Phys. Lett. 52, 1332 (1988).
3. M. H. Weiler, in Semiconductors and Semimetals (Academic Press, New York, 1981), R. K. Willardson and A. C. Beer, editors, Vol. 16, p. 119.
4. M. C. Chen and J. A. Dodge, Solid State Commun. 53, 449 (1986), and J. H. Tregilgas, J. Appl. Phys. 61, 727 (1987).
5. G. L. Hansen, J. L. Schmit, and T. N. Casselman, J. Appl. Phys. 53, 7099 (1982).
6. L. Eaves and J. C. Portal, J. Phys. C: Solid State Physics 12, 2809 (1979).
7. S. W. Mc Clure, D. G. Seiler, and C. L. Littler, J. Vac. Sci. Technol. A3, 271 (1985).

Table 1: Time Phase Task Schedule



▲ -- Task Started(Completed)

△ -- Task in Progress

X -- Completion Date



Table II. Sample Properties and Magneto-Optical Results

Sample	Manufacturer Nominal Properties			TPA Data		Impurity or Defect Levels Observed
#	$n(77K)$ ( $cm^{-3}$ )	$\mu(77K)$ ( $cm^2/V.sec$ )	$x$	$E_g(meV)$ at 7K	$x$	
#1	$1.4 \times 10^{14}$	$1.6 \times 10^5$	$0.2406 \pm 0.001$	$122.0 \pm 0.5$	$0.2364 \pm 0.0003$	Residual acceptor 9.0 meV above valence band edge
#2	$3.3 \times 10^{14}$	$8.2 \times 10^4$	$0.2450 \pm 0.0017$	$136.0 \pm 0.5$	$0.2448 \pm 0.0003$	Residual acceptor 10.4 meV above valence band edge
#3	$2.8 \times 10^{14}$	$1.2 \times 10^5$	--	$146.0 \pm 0.5$	$0.2508 \pm 0.0003$	--
#4	$1.0 \times 10^{14}$	$7.6 \times 10^4$	$0.2595 \pm 0.0015$	$156.0 \pm 0.5$	$0.2567 \pm 0.0003$	--
#5	$1.4 \times 10^{14}$	$6.6 \times 10^4$	$0.277 \pm 0.001$	$195.0 \pm 0.5$	$0.2801 \pm 0.0003$	Two closely spaced midgap levels seen at 94 and 100 meV above valence band edge
#6	$9.9 \times 10^{13}$	$5.3 \times 10^4$	$0.2995 \pm 0.0035$	$225.0 \pm 0.5$	$0.2976 \pm 0.0003$	--
#7	p-type $1.5 \times 10^{15}$	480	$0.2945 \pm 0.0035$	$222.0 \pm 1.0$	$0.2964 \pm 0.0006$	--

Table III. Two-Photon Magneto Absorption Transitions for  $\text{Hg}_{1-x}\text{Cd}_x\text{Te}$   
Given From Low Energy to Higher Energies.

<u>Designation</u>	<u>Energy Level Transition</u>	<u>Polarization</u>
$R_1$	$a^-(2) \rightarrow a^c(0)$	$\sigma_R$
$R_2$	$b^-(2) \rightarrow b^c(0)$	$\sigma_R$
$\pi_1$	$a^+(0) \rightarrow a^c(0)$	$\pi$ or $\sigma$
$L_1$	$a^+(-1) \rightarrow a^c(1)$	$\sigma_L$
$\pi_2$	$a^-(1) \rightarrow a^c(1)$	$\pi$ or $\sigma$
$R_3$	$a^-(3) \rightarrow a^c(1)$	$\sigma_R$
$\pi_3$	$b^-(1) \rightarrow b^c(1)$	$\pi$ or $\sigma$
$L_2$	$b^+(-1) \rightarrow b^c(1)$	$\sigma_L$
$\pi_4$	$b^+(0) \rightarrow b^c(0)$	$\pi$ or $\sigma$
$\pi_5$	$a^-(2) \rightarrow a^c(2)$	$\pi$ or $\sigma$
$\pi_6$	$b^-(2) \rightarrow b^c(2)$	$\pi$ or $\sigma$
$R_4$	$a^+(2) \rightarrow a^c(0)$	$\sigma_R$
$L_3$	$a^+(0) \rightarrow a^c(2)$	$\sigma_L$
$\pi_7$	$a^+(1) \rightarrow a^c(1)$	$\pi$ or $\sigma$
$\pi_8$	$a^-(3) \rightarrow a^c(3)$	$\pi$ or $\sigma$
$L_4$	$b^+(0) \rightarrow b^c(2)$	$\sigma_L$

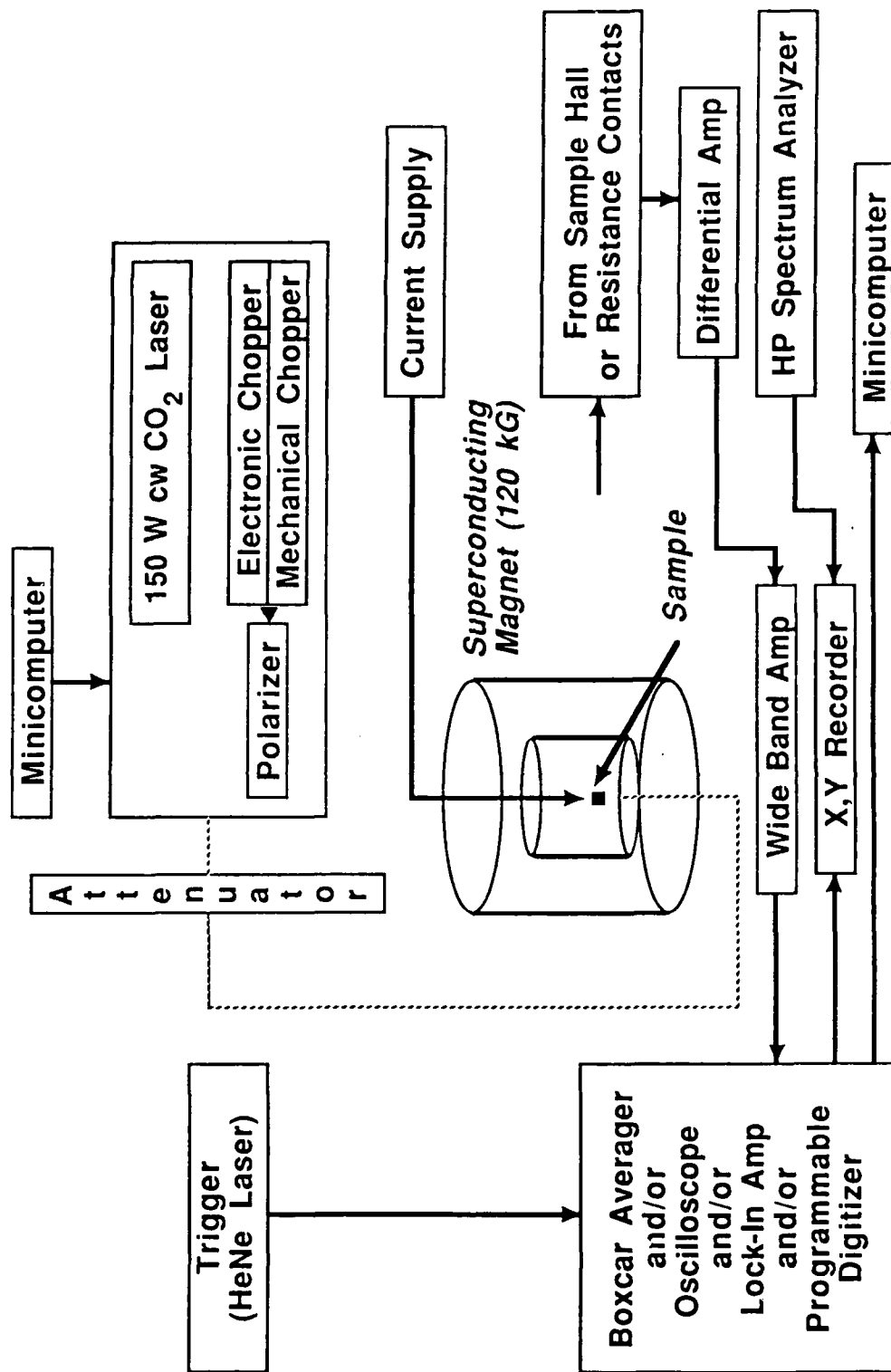


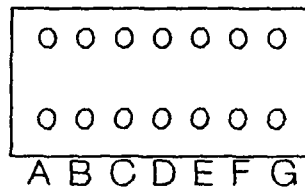
Figure 1. Schematic diagram of experimental apparatus.

# University of North Texas High Magnetic Field Facility

## Sample Holder

AUGAT type 528-AG10D PC terminal connector cut in half

1 2 3 4 5 6 7



← white strip on side  
of terminal connector

Dimensions: 1" by 1" diagonal

## SAMPLE CONFIGURATIONS:

\_ Sample connections \_      \_ Use contact pair \_

current.....(1&7) or (A&G)

resistivity.....(2&6) or (B&F)

resistivity (2nd pair).....(3&5) or (C&E)

Hall .....(2&B) or (3&C) or  
(5&E) or (6&F)

no contacts on 4 and D

Figure 2: Sample Holder Diagram

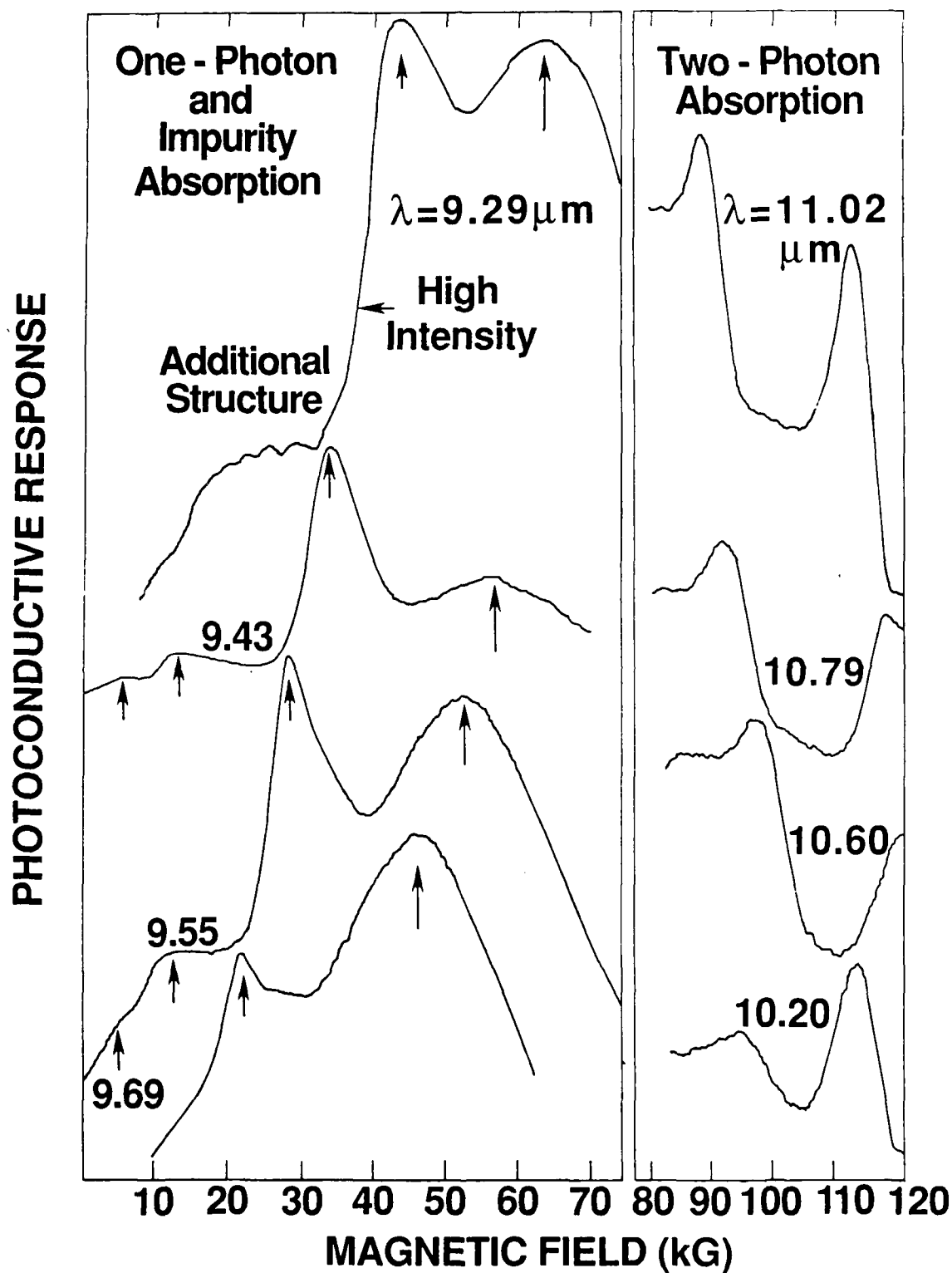


Figure 3. Magneto-Optical spectra at various CO<sub>2</sub> laser wavelengths for sample #1.

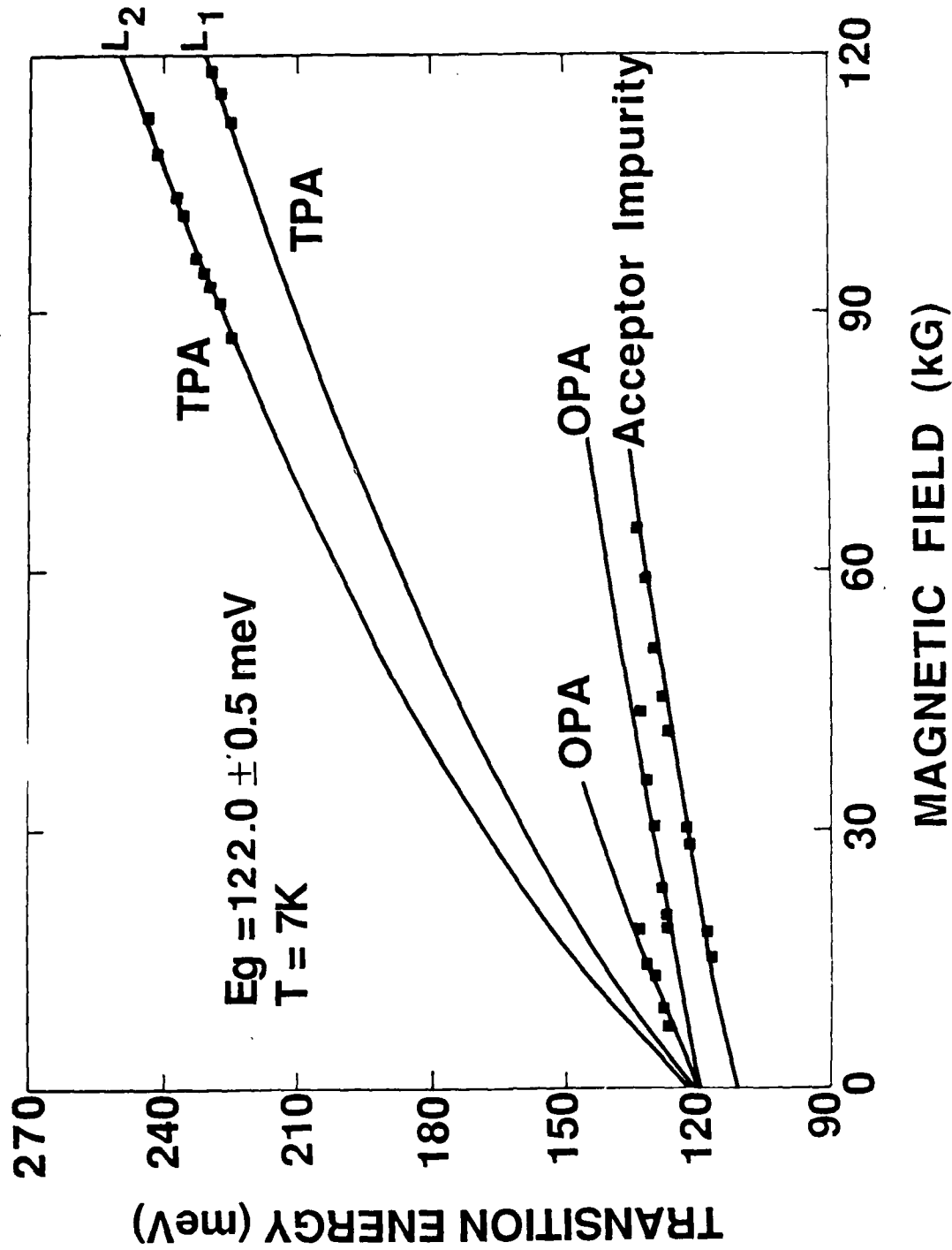


Figure 4. Transition Energy versus Magnetic field showing one-photon absorption (OPA), two-photon absorption (TPA), and acceptor impurity absorption behavior for sample #1.

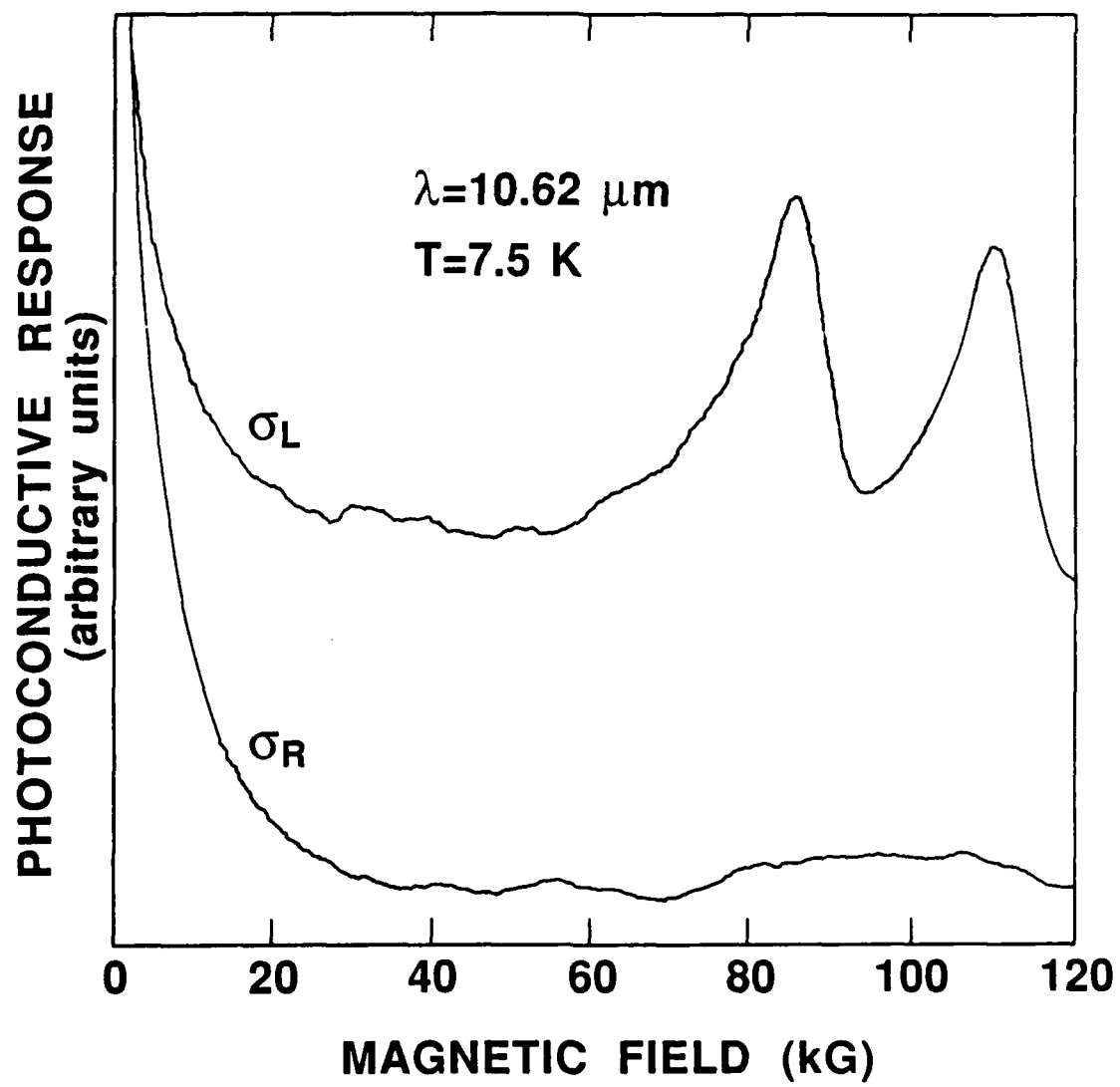


Figure 5. Polarization dependence of TPA spectra.

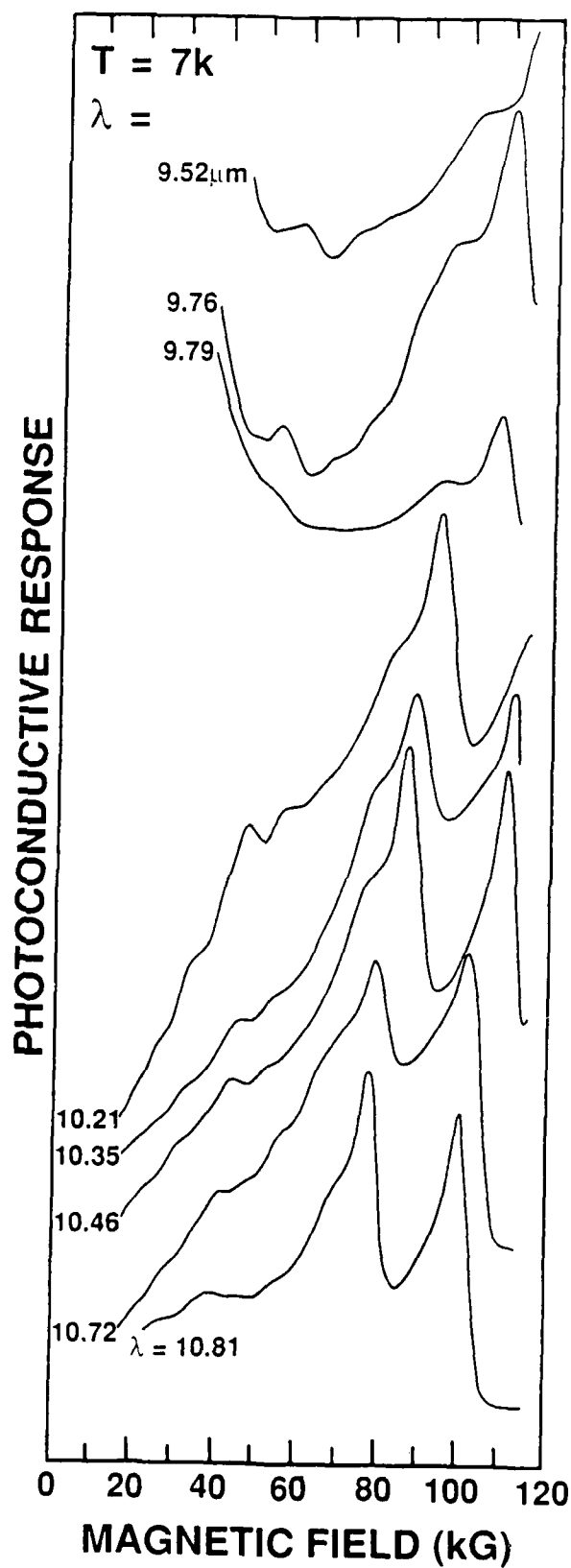


Figure 6. Wavelength dependence of the photoconductive response of sample #2.



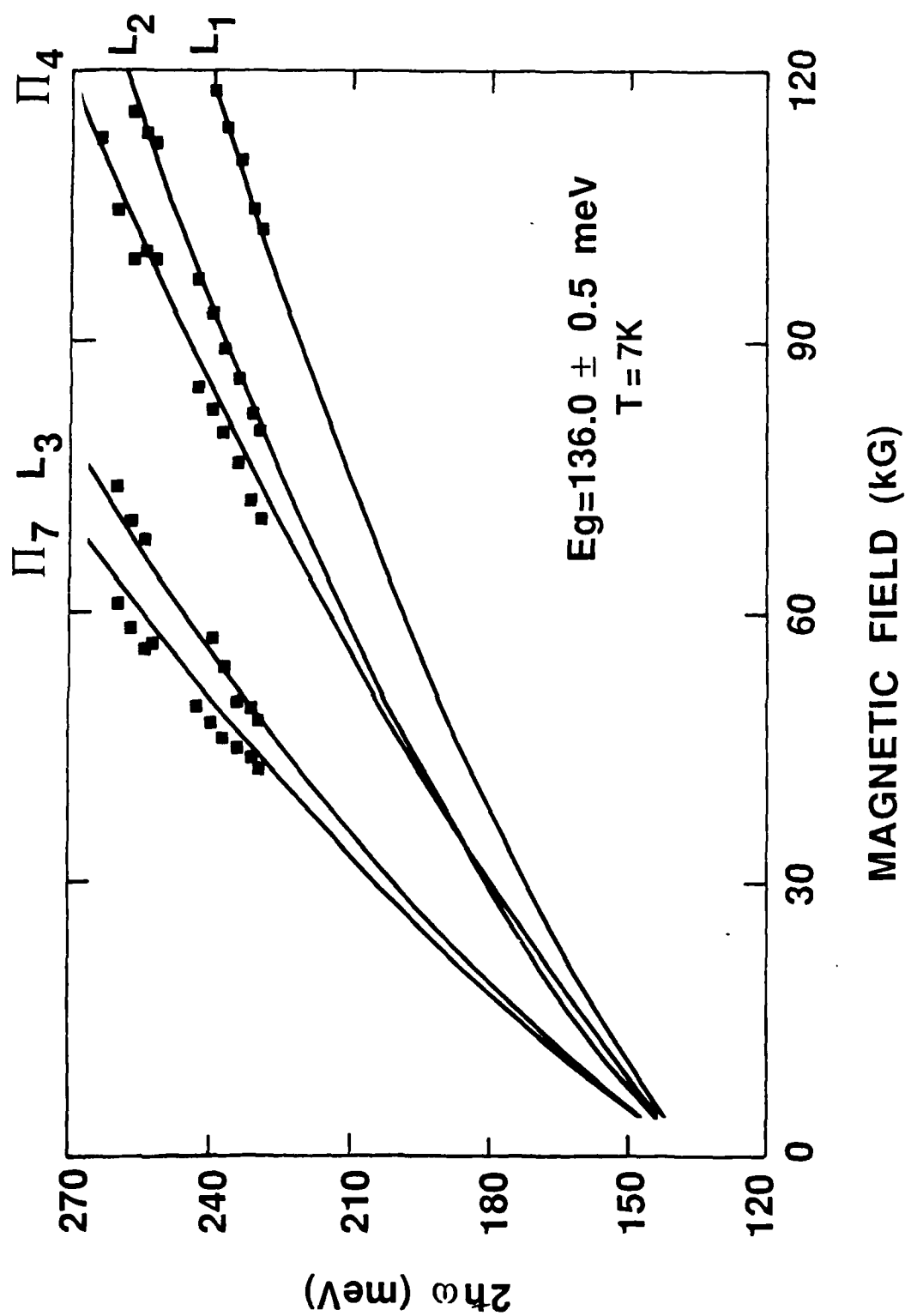


Figure 7. Transition Energy versus magnetic field for sample #2.

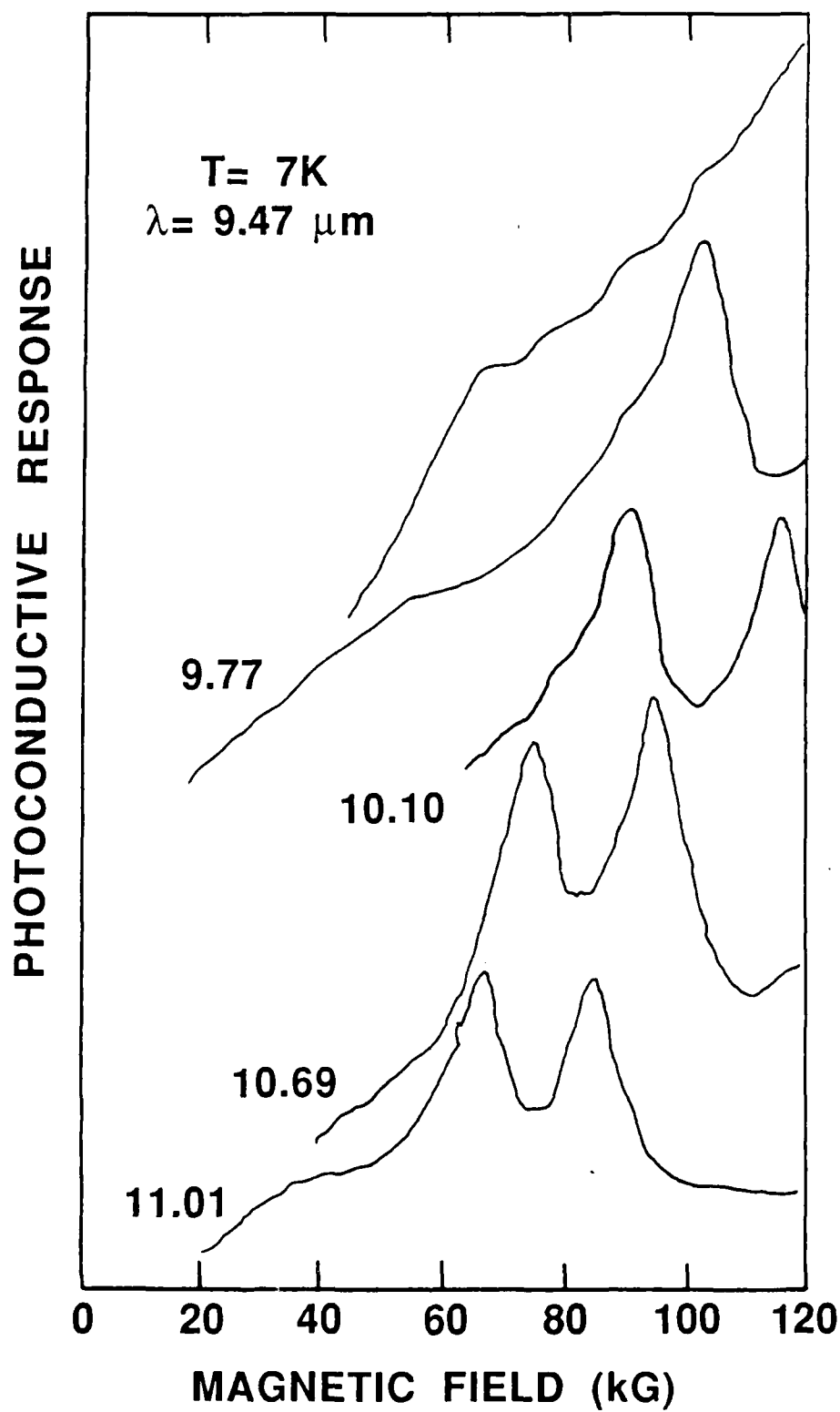


Figure 8. Wavelength dependence of photoconductive response for sample #3.

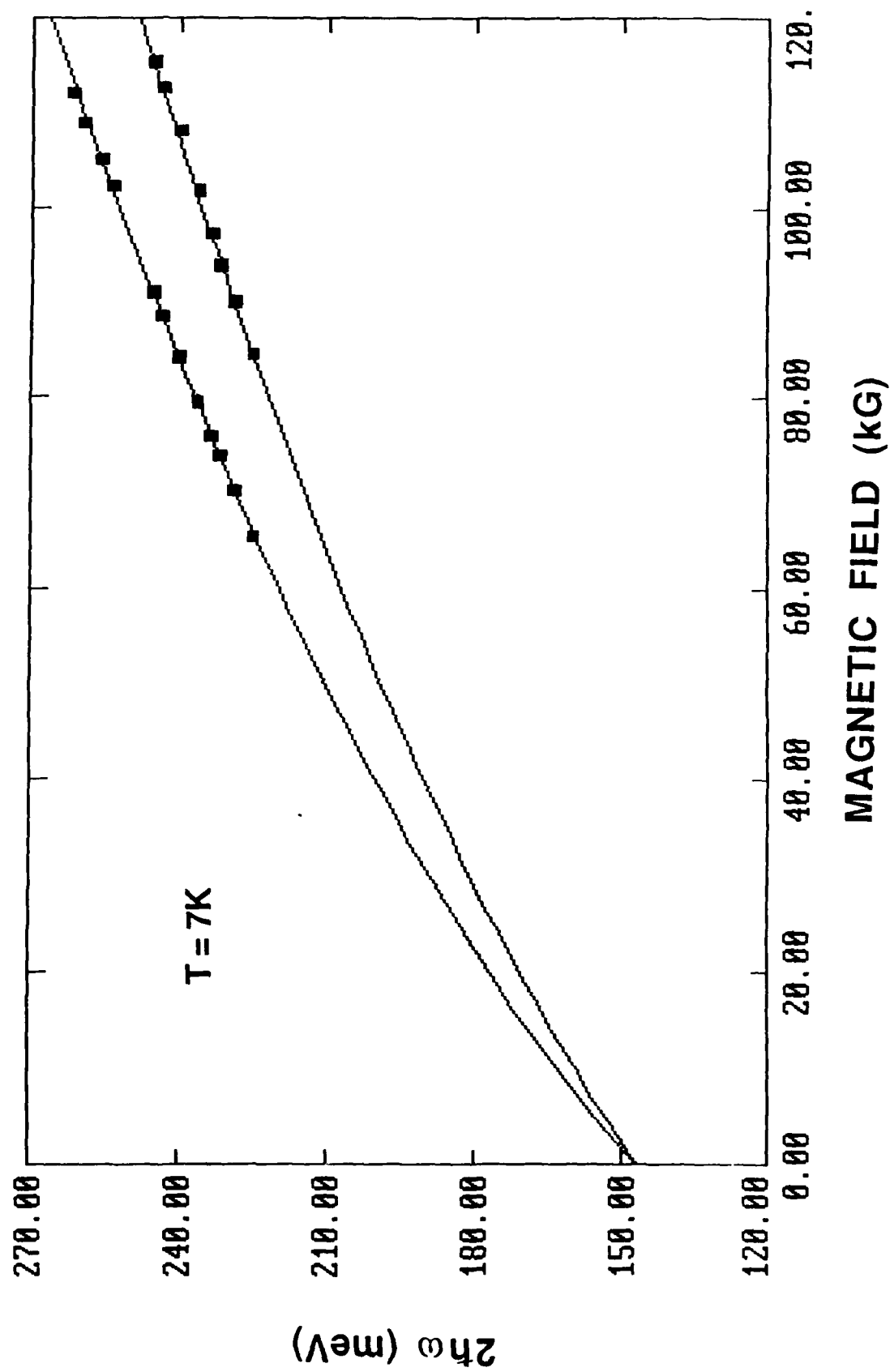


Figure 9. Transition energy vs. magnetic field for the TPMA spectra from the Tl<sub>1</sub>thm sample. The 7K energy gap from the fit of theory (solid lines) to data (solid boxes) is 146.5 meV.

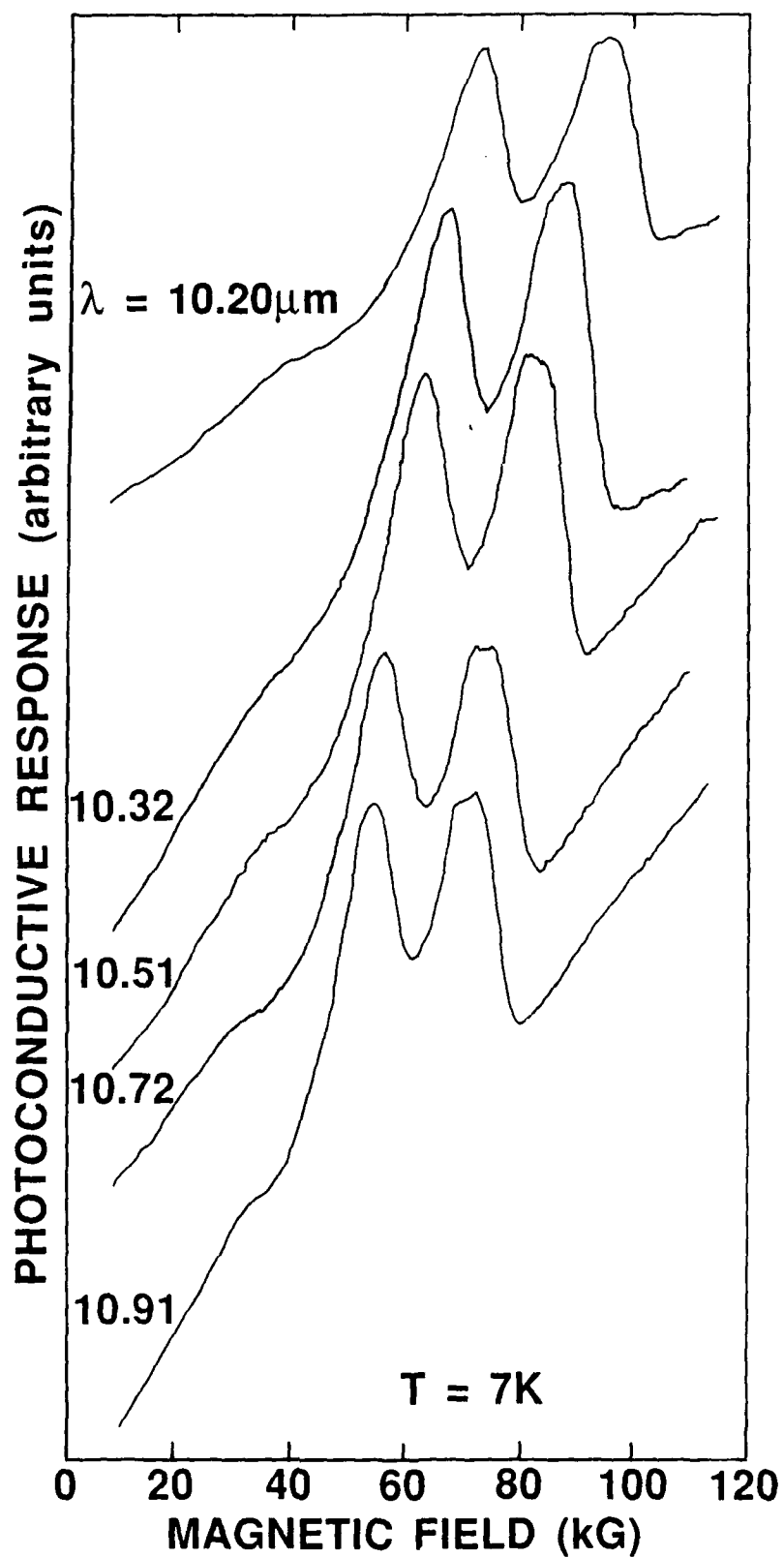


Figure 10. Photoconductive response vs. magnetic field for  $x = 0.26$  sample. Note the two-photon absorption peaks.

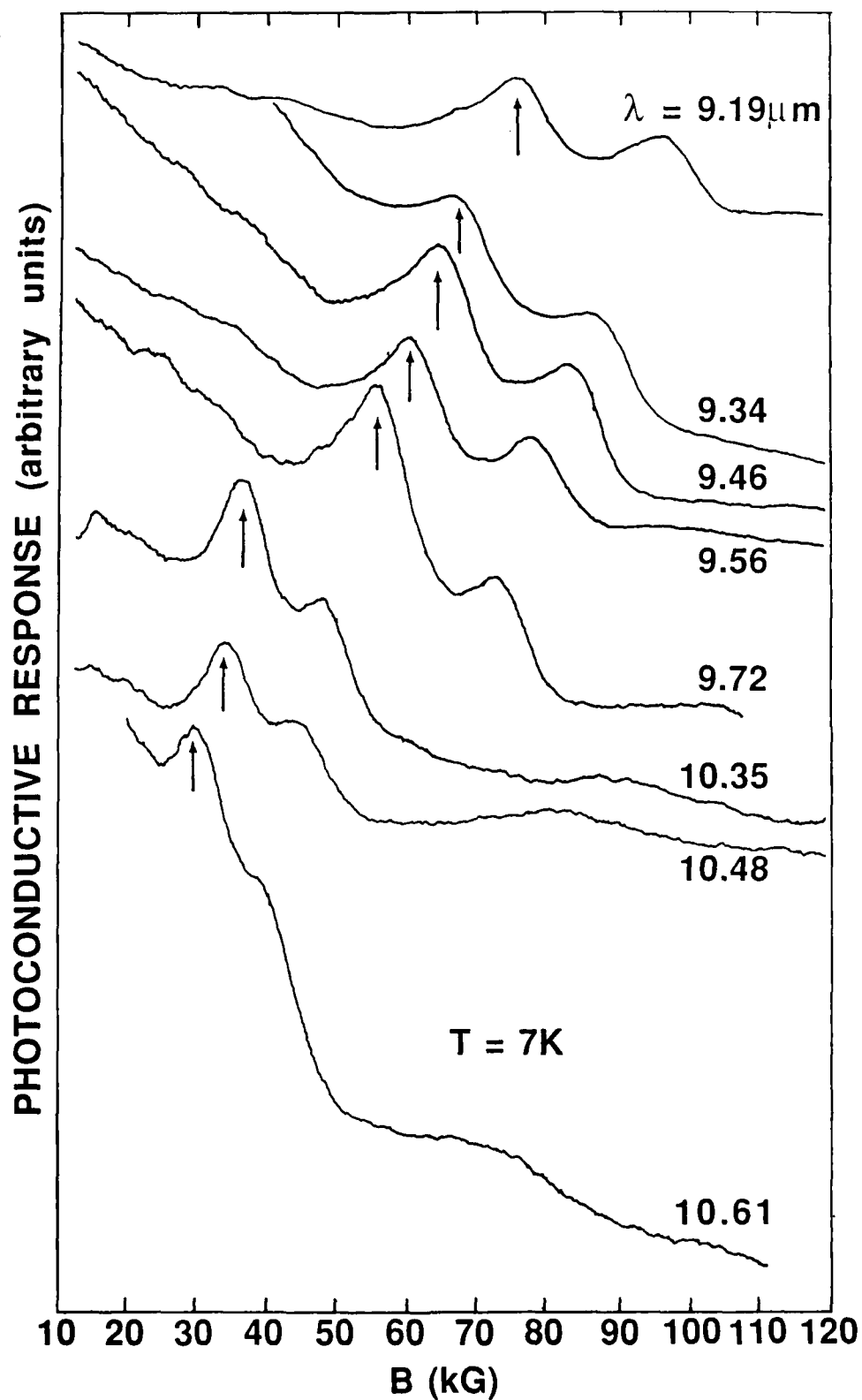


Figure 11. Photoconductive response vs. magnetic field for  $x = 0.27$  sample. Note the two-photon absorption peaks.

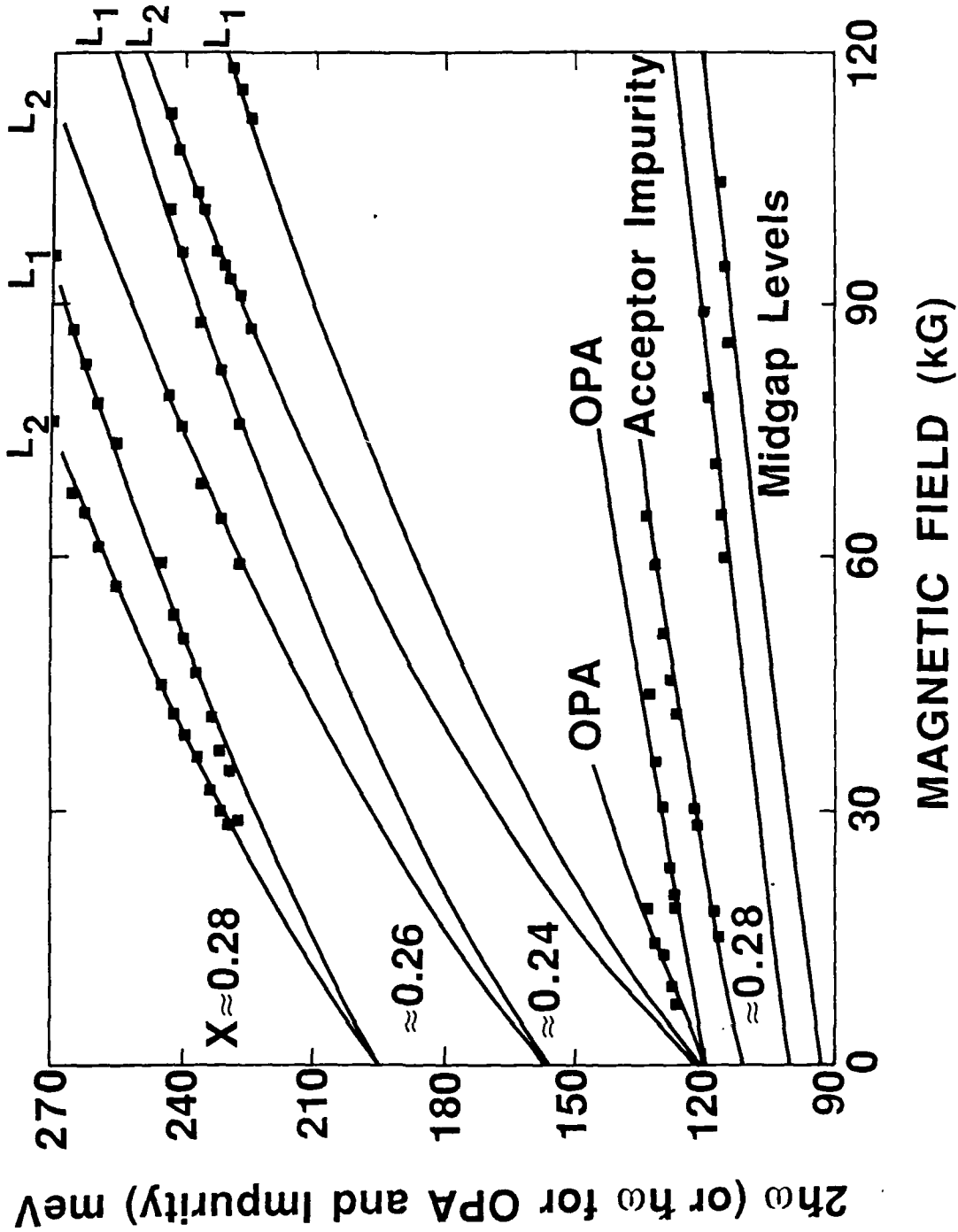


Figure 12. Fan chart plots of one-photon, two-photon, and impurity or defect behavior for samples #1, #4, and #5.

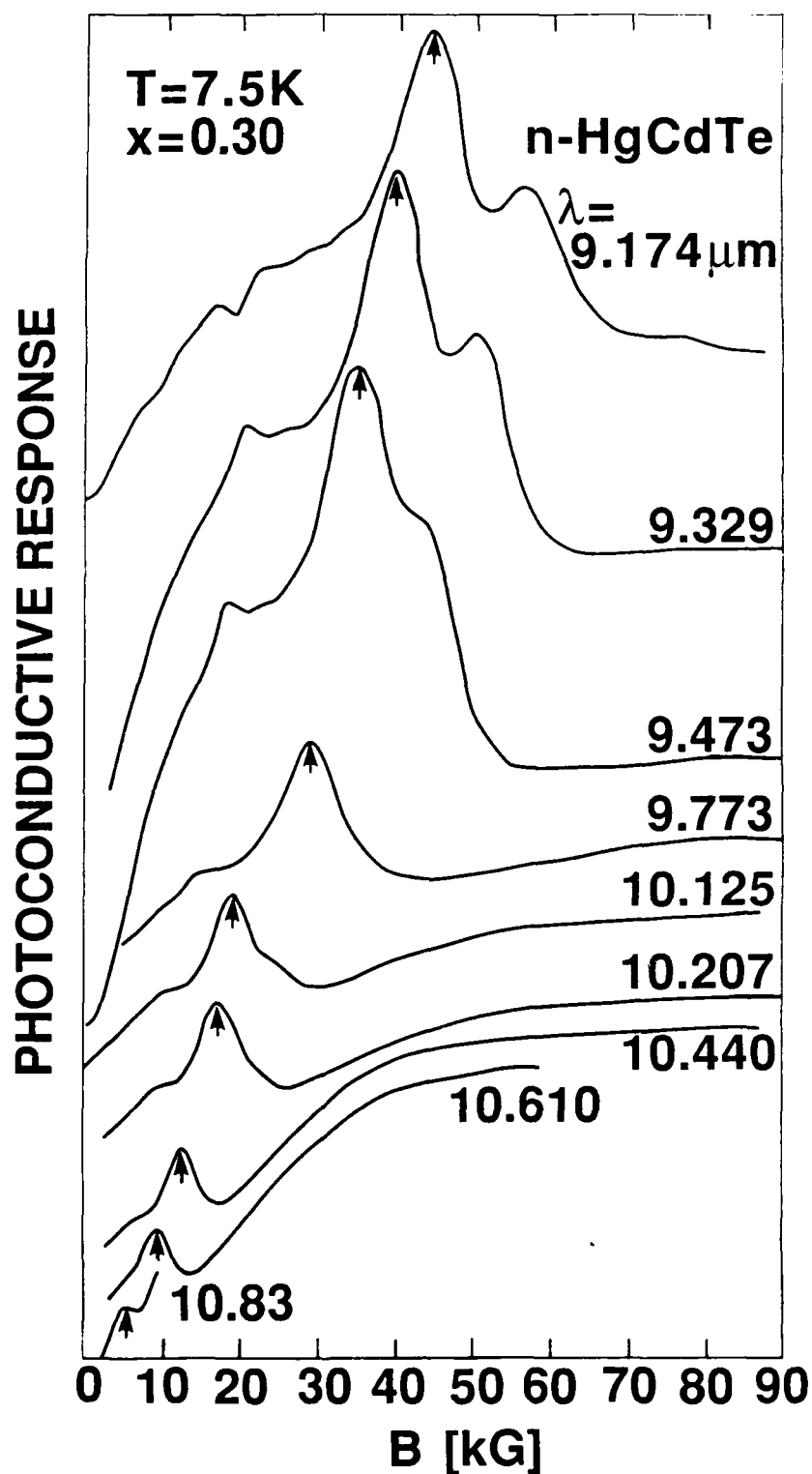


Figure 13. Wavelength dependence of the photoconductive response for sample #6.

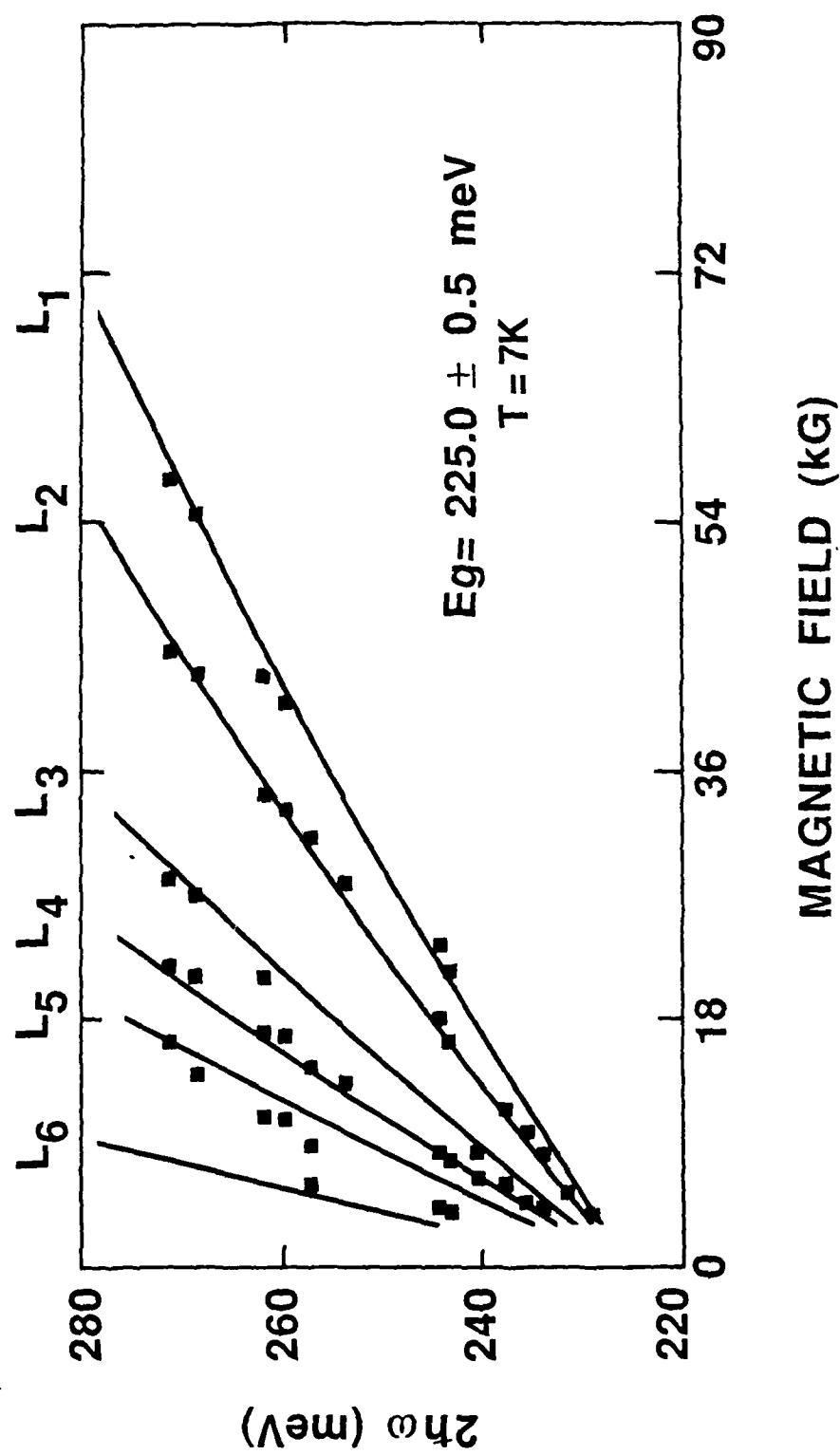


Figure 14. Transition energy versus magnetic field behavior for sample #6.



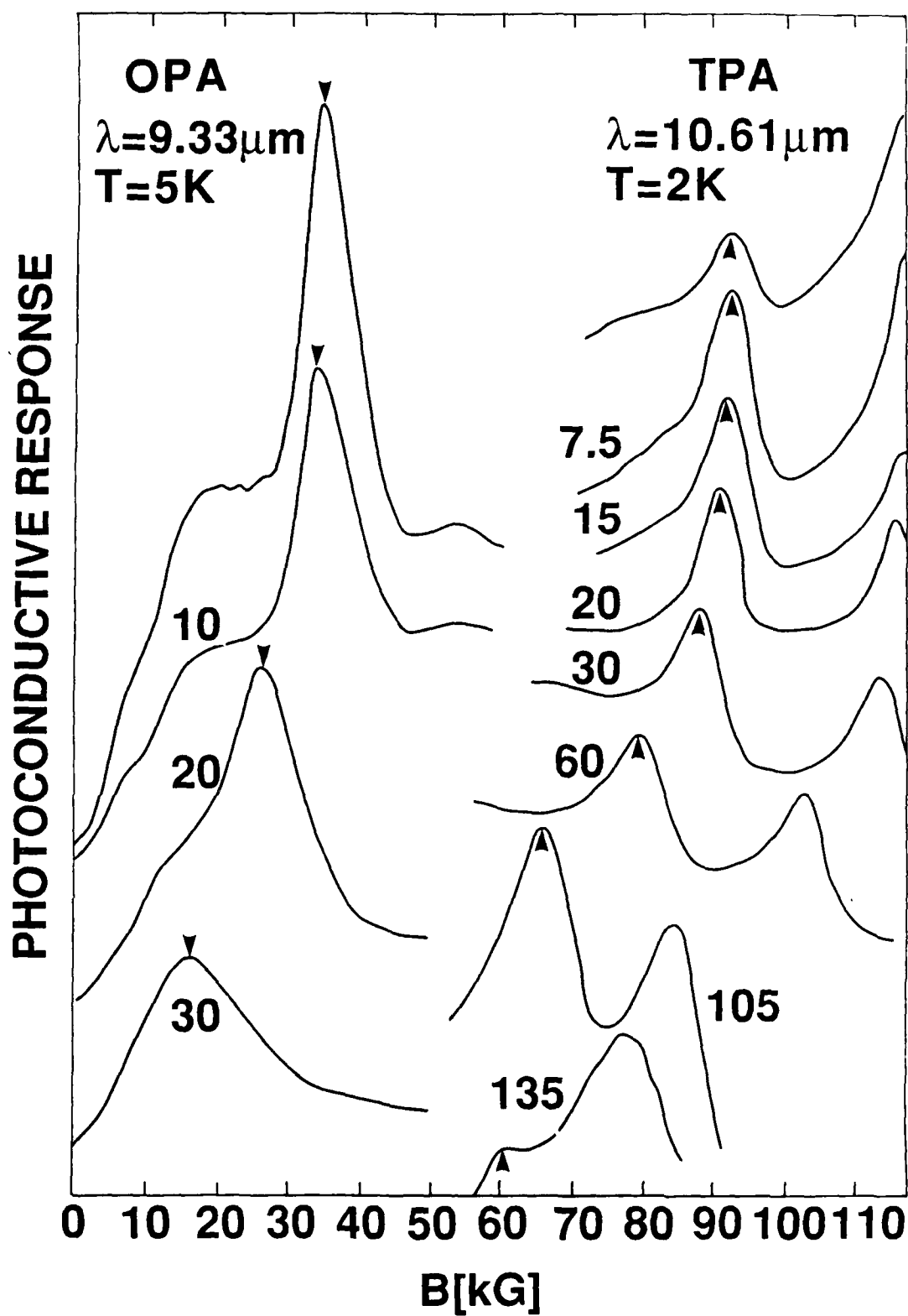


Figure 15. Temperature dependence of the OPA and TPA magneto-optical spectra for sample #1.

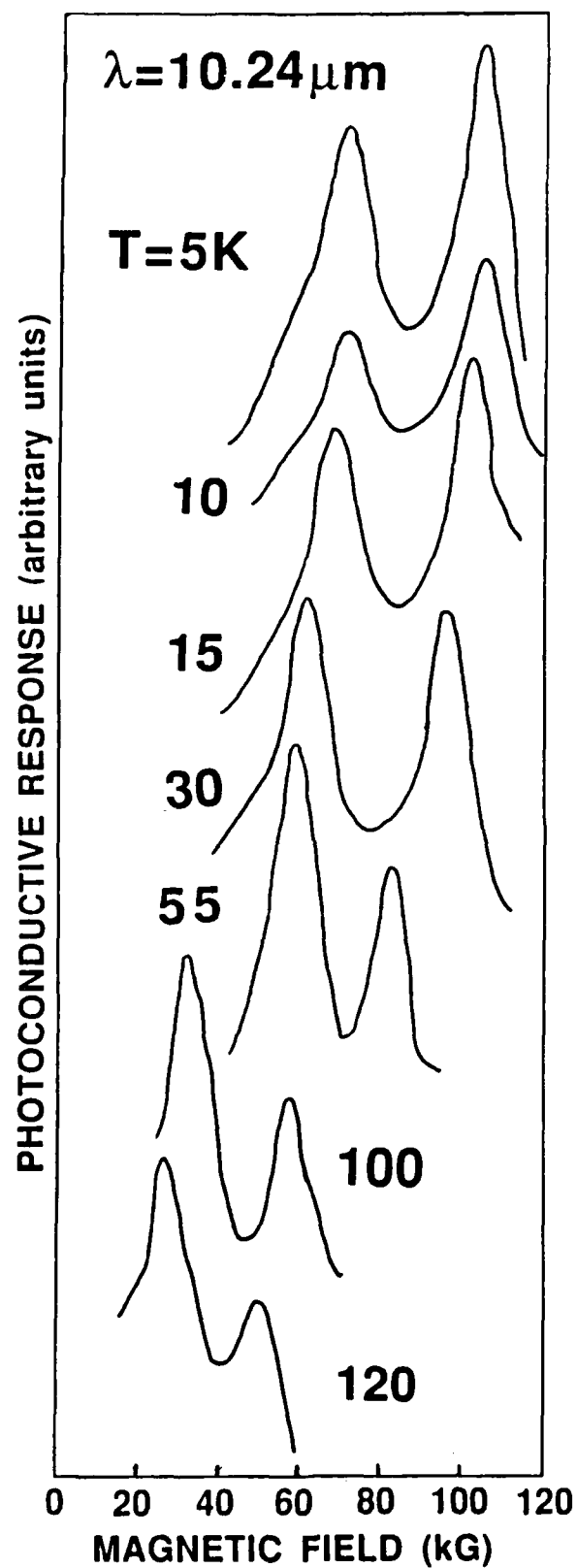
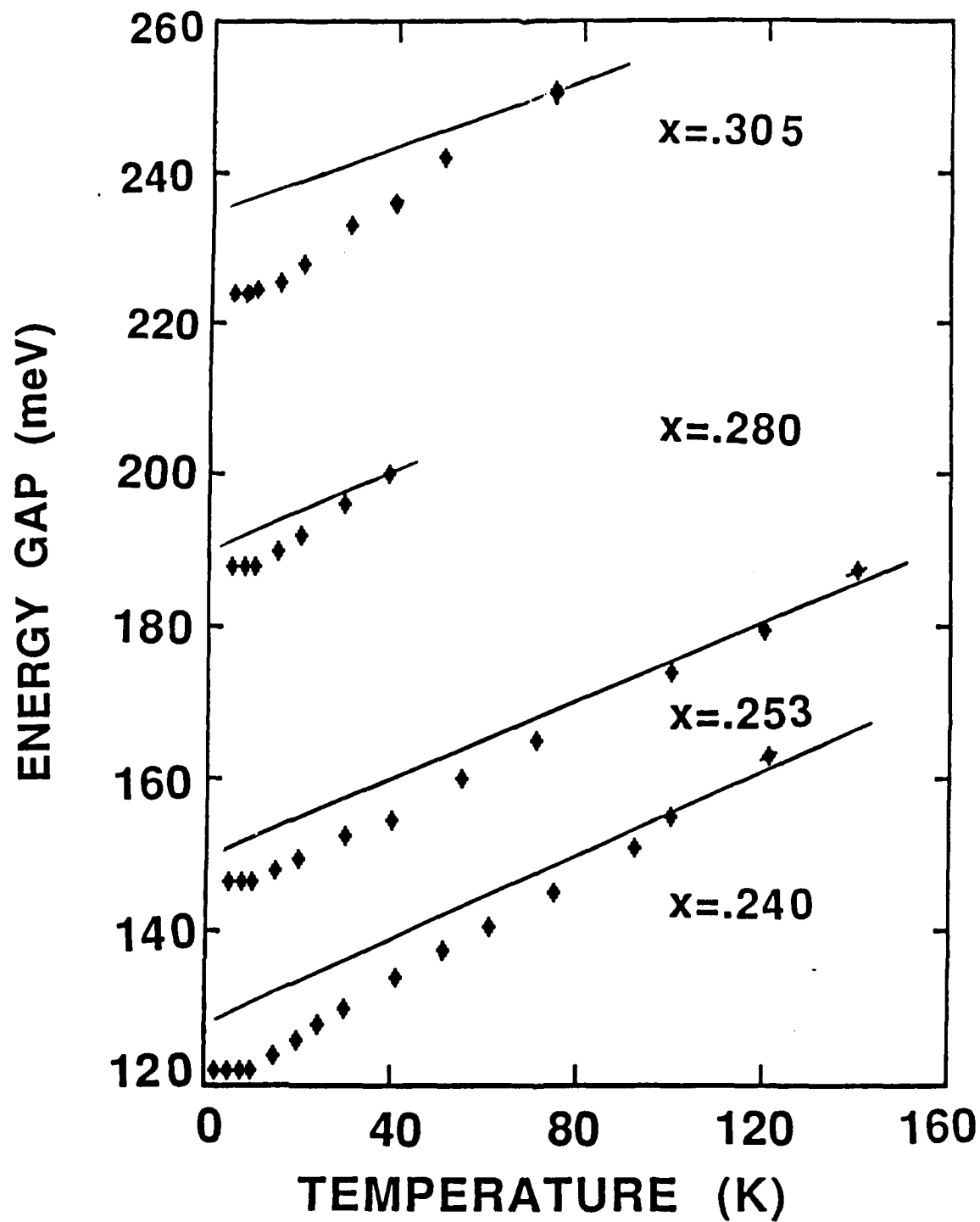


Figure 16. Temperature dependence of the photoconductive spectra for the TI THM sample.

Figure 17. Energy gap dependence on temperature for five samples, ranging in  $x$ -value from 0.240 to 0.305. The  $x$ -values listed are obtained from fit of the HSC relation to the high temperature data.



• Exp. Data  
—HSC



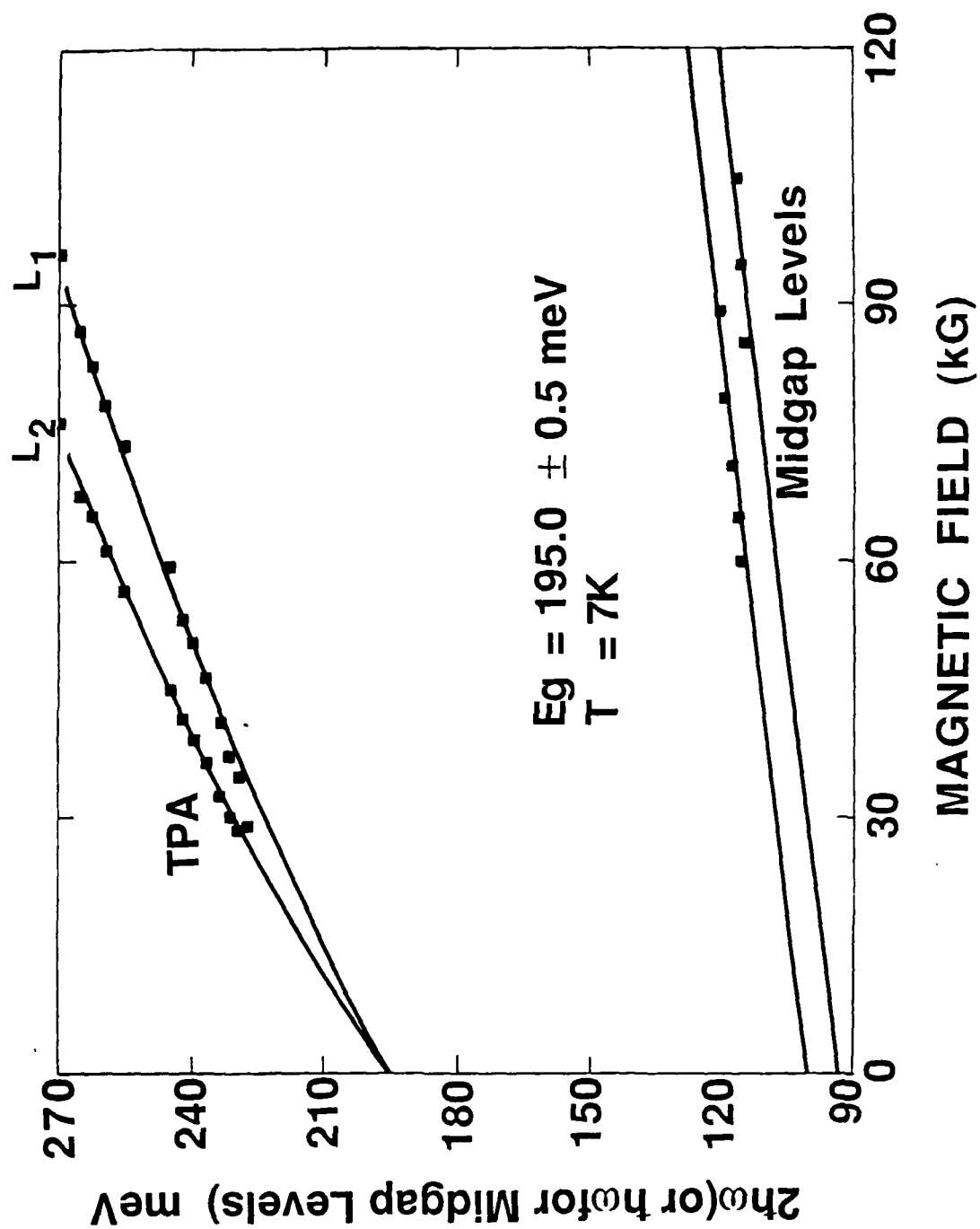


Figure 19. Transition energy versus magnetic field behavior for sample #5.

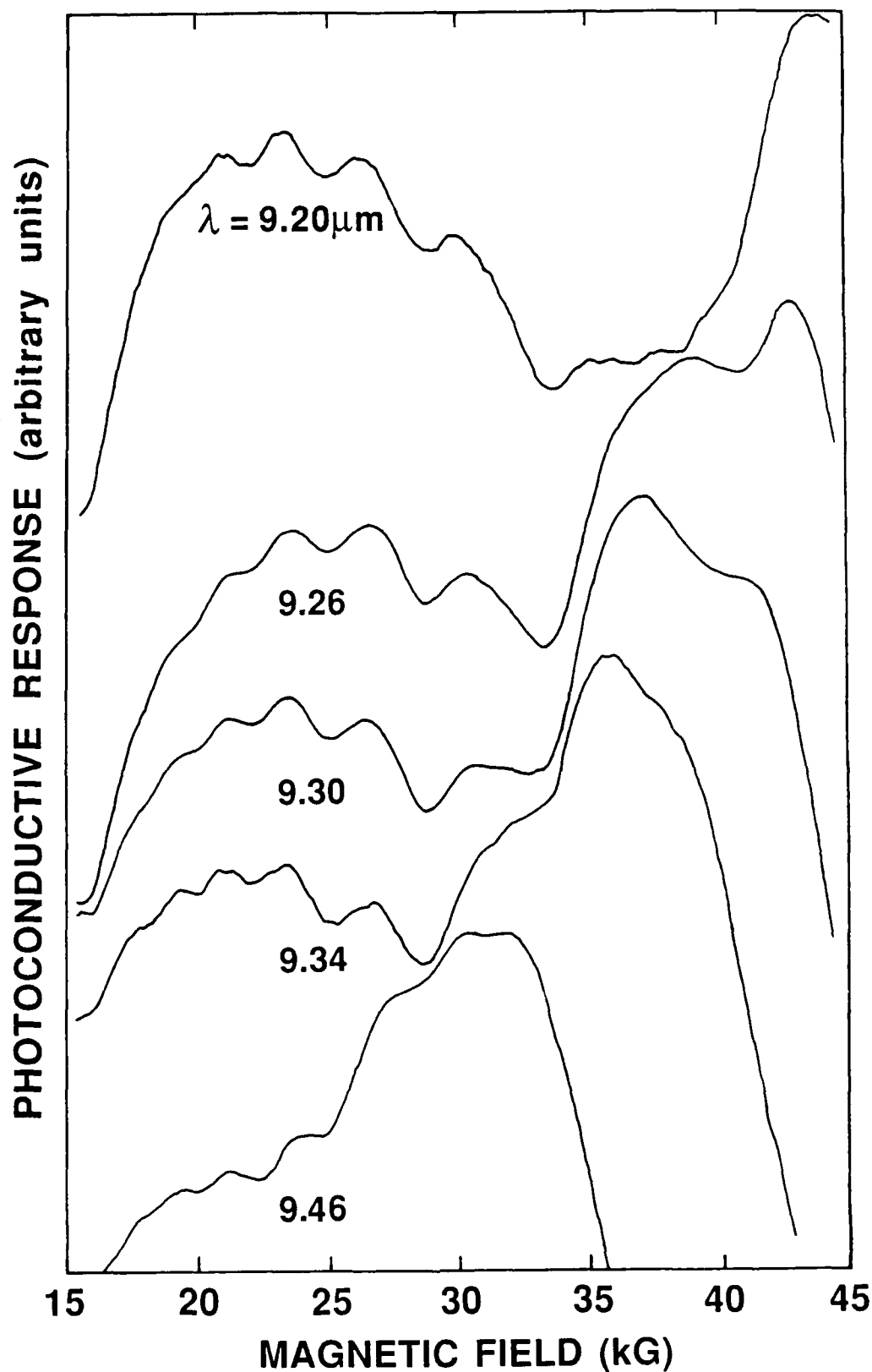


Figure 20. Wavelength dependence of the high intensity structure showing the movement of the one-photon magneto absorption (OPMA) structure against the high intensity structure.

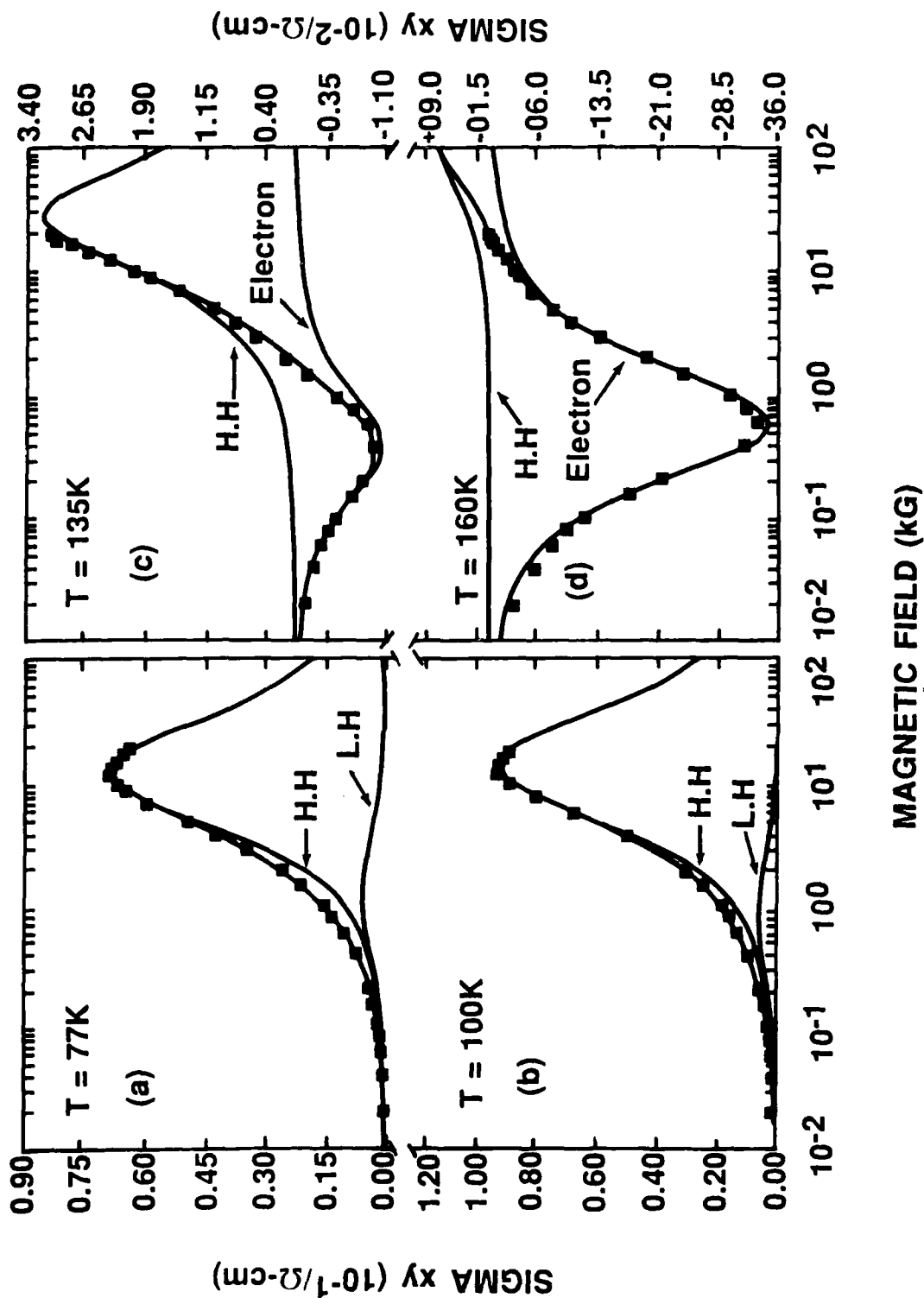
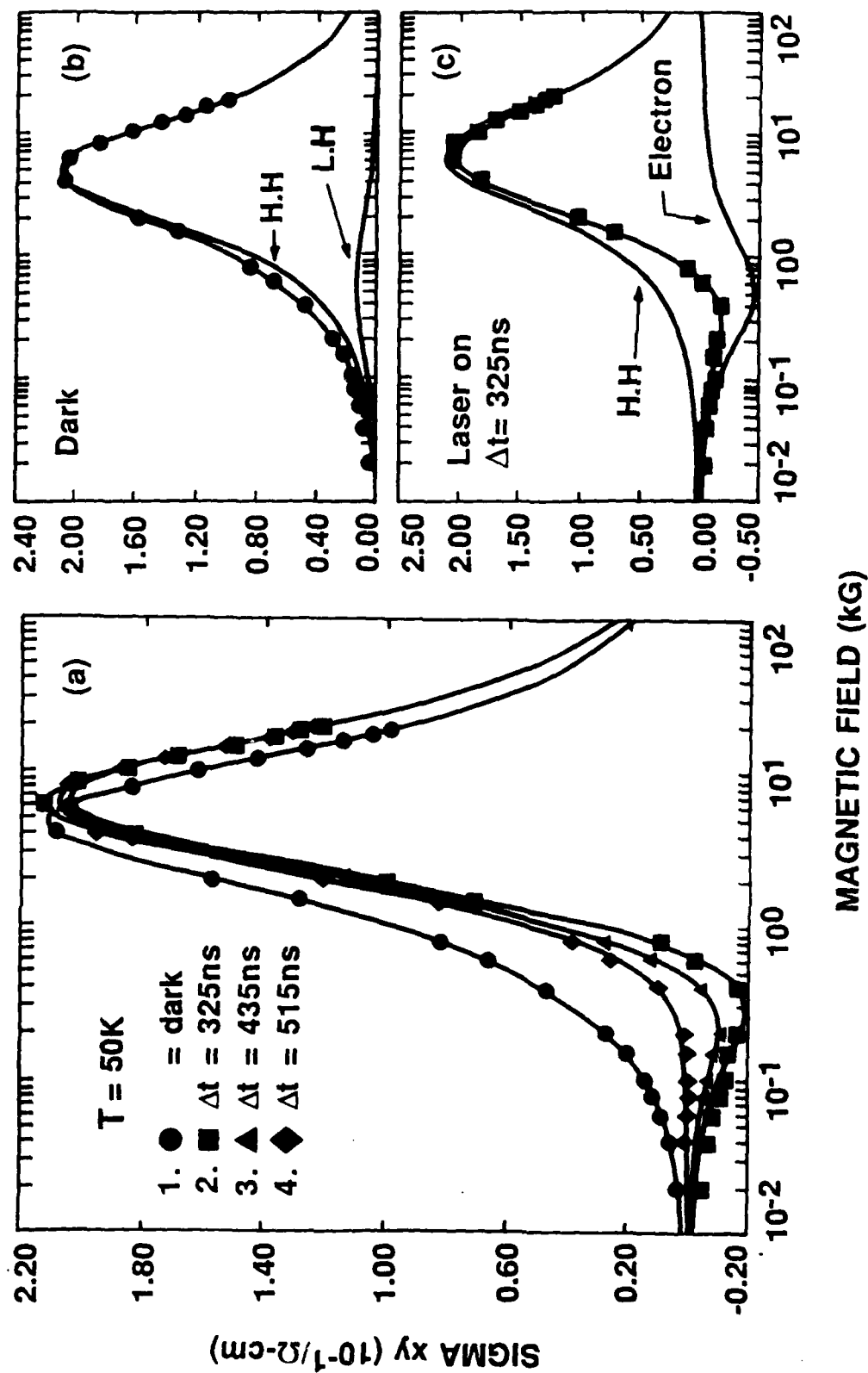


Figure 21.  $\sigma_{xy}$  vs. magnetic field for various temperatures.

Figure 22. Time resolved data:

- a)  $\sigma_{xy}$  response in the dark, 325, 435, and 515 nsec after start of laser pulse.
- b) Response in the dark, before the laser pulse.
- c) Peak signal, corresponding to the peak of the laser pulse.





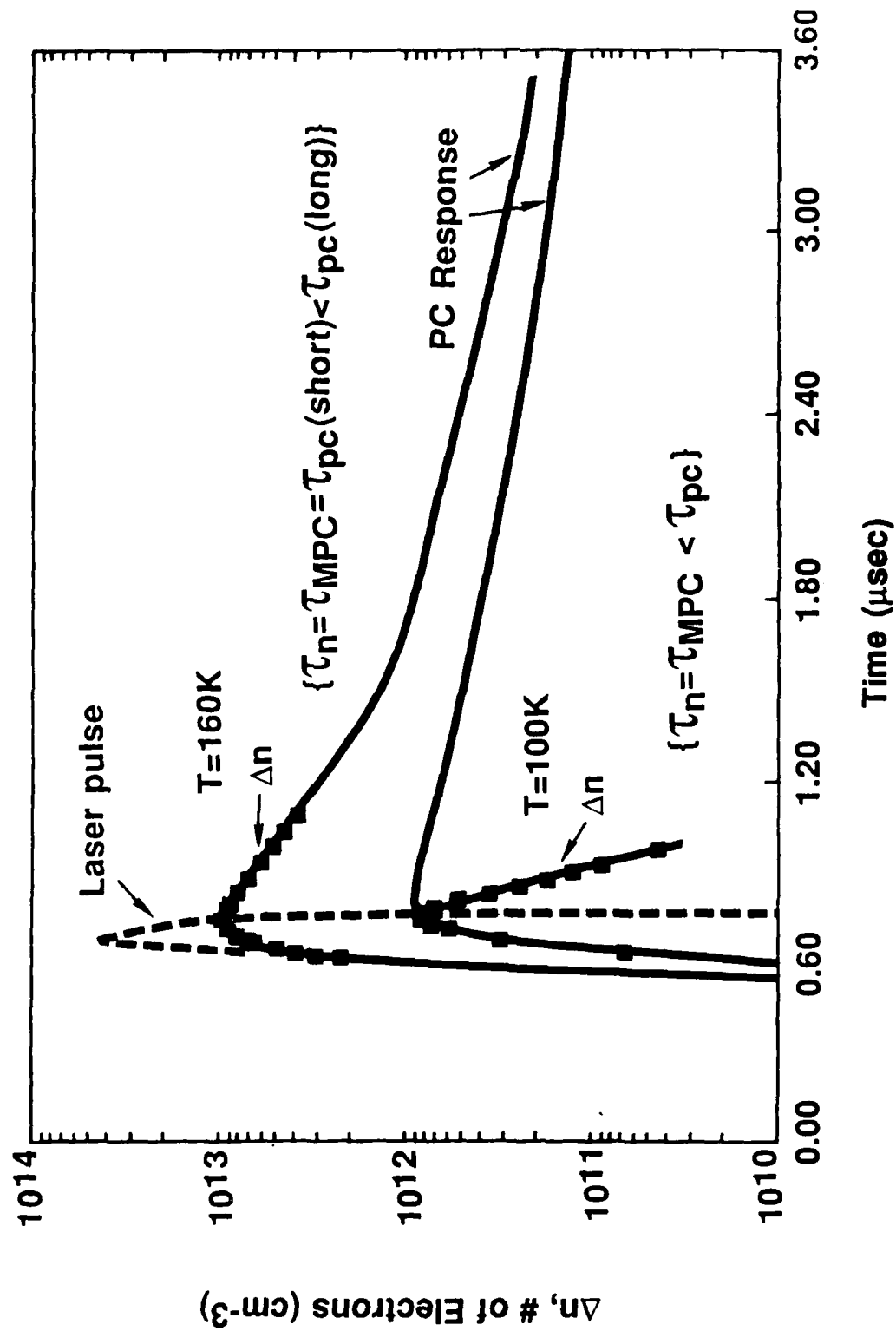


Figure 23. Comparison of the photoconductive and the magneto-photoconductive responses.

# PC Transient Response

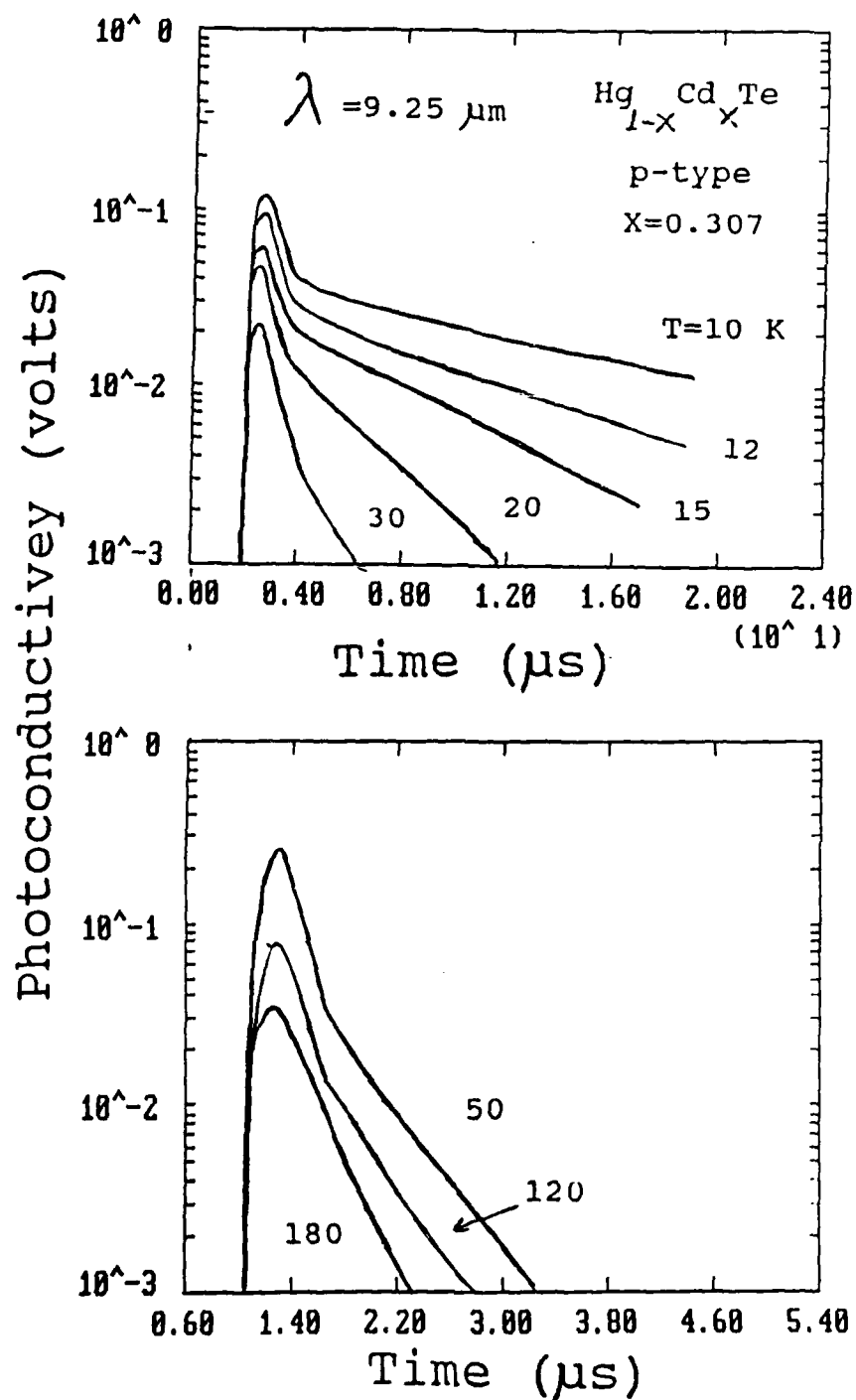


Figure 24. Transient photoconductive response at various temperatures.

**Appendix.** Reprints of publications resulting from the first year's work. They are appended in the following order:

1. "New Method of Characterizing Majority and Minority Carriers in Semiconductors," published in Applied Physics Letters.
2. "Determination of Minority-Carrier Lifetimes in p-type Narrow Band-Gap Semiconductors with Two-Photon Absorption Excitation," published in Applied Physics Letters.
3. "New Laser-Based Magneto-Optical Studies of HgCdTe Alloys," to be published in Solid State Communications.
4. "Nonlinear Magneto-Optical Spectroscopy of HgCdTe By Two-Photon Absorption Techniques," to be published in Journal of Vacuum Science and Technology.

# New method of characterizing majority and minority carriers in semiconductors

D. L. Leslie-Pelecky, D. G. Seiler, and M. R. Loloee

Center for Applied Quantum Electronics, Department of Physics, North Texas State University, Denton, Texas 76203

C. L. Littler

Central Research Laboratories, Texas Instruments, Inc., Dallas, Texas 75265

(Received 13 July 1987; accepted for publication 5 October 1987)

A novel characterization method using magnetoconductivity tensor components to determine the carrier concentration and mobility of majority and minority carriers is presented. Results are given for bulk *n*-HgCdTe (one carrier), liquid phase epitaxial *n*-HgCdTe (two carriers), and *p*-InSb (two or three carriers). Advantages of this method over the standard Hall coefficient analysis are discussed.

Advances in the improvement and application of new semiconducting materials (the use of HgCdTe in infrared detectors, for example) have necessitated an increased interest in the properties of minority carriers. Although Hall coefficient ( $R_H$ ) and magnetoresistance measurements have historically been used to characterize semiconductors by determining the carrier concentration ( $n$ ), mobility ( $\mu$ ), and relaxation time ( $\tau$ ) of the majority carriers, the form of the multicarrier Hall coefficient makes detailed information about minority carriers difficult to obtain. In this letter, we show that the complete magnetic field dependence of the magnetoconductivity provides more information than the traditional  $R_H$  measurement and analysis, allowing us to determine  $n$ ,  $\mu$ , and  $\tau$  for all carriers. Magnetoconductivity tensor components, which have the distinct advantage of being additive in the case of more than one carrier, have previously been used to characterize metals.<sup>1-3</sup> We demonstrate the power and ease of this method through application to bulk *n*-type  $\text{Hg}_{1-x}\text{Cd}_x\text{Te}$  (one carrier conduction), *n*-type liquid phase epitaxial (LPE) HgCdTe (two carriers), and *p*-type InSb (two-carrier conduction at low temperatures and three-carrier conduction at temperatures  $\approx 125$ –140 K).

The solution of the Boltzmann equation using a relaxation time approximation (RTA) has been detailed by Beer and others.<sup>4-6</sup> By finding the current density in terms of the electric field, the conductivity tensor may be identified. For a sample in the standard Hall configuration ( $\mathbf{H} = H\hat{z}$ ), the conductivity tensor components may be written:

$$\sigma_{xx} = \frac{\rho_{xx}}{\rho_{xx}^2 + R_H^2 H^2} \approx \sum_{i=1}^M \frac{n_i |e| H_i}{H_i^2 + H^2}, \quad (1a)$$

$$\sigma_{xy} = \frac{R_H H}{\rho_{xx}^2 + R_H^2 H^2} \approx \sum_{i=1}^M \frac{n_i e H}{H_i^2 + H^2}, \quad (1b)$$

where  $\rho_{xx}$  and  $R_H$  are the standard measured quantities of transverse magnetoresistance and Hall coefficient, respectively,  $M$  is the number of carrier types, the critical magnetic field  $H_i \approx 1/\mu_i = m^*/\tau_i e$ , in which  $\mu_i$  and  $\tau_i$  are average quantities.<sup>7</sup>  $n_i$  is the concentration of carriers of type  $i$  and  $e < 0$  for electrons. The applicability of the relaxation time approximation (RTA) to our mobility considerations might be questioned, since optical phonon scattering (inherently inelastic) is one of the dominant modes in compound semi-

conductors.<sup>8</sup> However, as shown by Pfeffer and Zawadzki<sup>9</sup> for InSb at room temperature, the variational mobility calculation for optic phonon scattering gives almost the same result as the RTA. As the temperature is lowered, the RTA becomes progressively less and less valid, but also the optic phonon contribution to the mobility becomes less important. For example, at 77 K and an electron concentration of  $10^{16} \text{ cm}^{-3}$ , the experimental mobility of electrons in *n*-InSb is  $10^5 \text{ cm}^2/\text{V s}$ , (Ref. 8) while the optic phonon contribution is  $1.5 \times 10^6 \text{ cm}^2/\text{V s}$ .<sup>9</sup> The elastic modes of scattering by ionized impurity and acoustic phonons can be treated by RTA. Thus, within the above approximations, the calculated individual relaxation times have physical meaning.

Note that  $\sigma_{xx}$  is positive for all carriers, while  $\sigma_{xy}$  will be negative for electron conduction and positive for hole conduction. Because of the differences in sign, we choose to fit  $\sigma_{xy}$  data, as differences in types of carriers become obvious upon plotting the experimental data. For  $\sigma_{xy}$ , the maximum value occurs when  $H = H_i$  and is proportional to  $n_i$  ( $\sigma_{xy} = n_i e/2H_i$ ). Because of the simple algebraic form of Eq. (1b) and the ease with which partial derivatives are taken, any nonlinear least-squares fit is sufficient for fitting Eq. (1b) to the experimental  $\sigma_{xy}$  data as determined from the right-hand side of Eq. (1b).

Figure 1 shows  $\sigma_{xy}$  vs  $\ln H$  at 77 K for a bulk *n*-type  $\text{Hg}_{1-x}\text{Cd}_x\text{Te}$  sample, grown by the solid-state recrystallization method ( $x \approx 0.23$ ). The negative values of  $\sigma_{xy}$  indicate that conduction occurs by electrons. From the form of Eq. (1b), where  $M = 1$ , we see that the  $(x, y)$  coordinate describing the peak of the curve corresponds to the pair

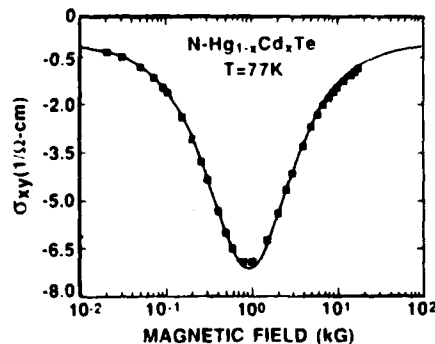


FIG. 1.  $\sigma_{xy}$  vs  $\ln H$  for *n*-type HgCdTe at 77 K.

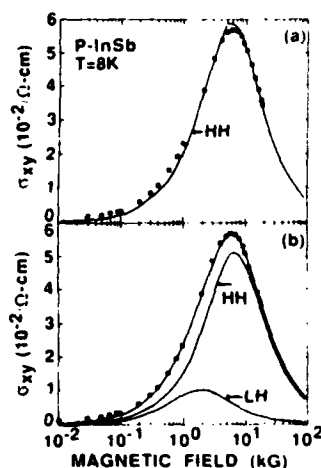


FIG. 2. (a) and (b) *p*-type InSb at 8 K: A simple, one-carrier Hall coefficient analysis finds  $7.04 \times 10^{13}$  carriers/cm<sup>3</sup> with mobilities of  $1.51 \times 10^4$  cm<sup>2</sup>/V s at  $B = 1$  kG and  $7.6 \times 10^{13}$  carriers/cm<sup>3</sup> with mobility of  $1.40 \times 10^4$  cm<sup>2</sup>/V s at  $B = 19$  kG. Note that there is negligible magnetic carrier freeze-out at these low fields (see Fig. 3 also).

$[H_i, \sigma_{xy}(\max)]$ . The coordinates of the peak therefore provide initial guesses for parameters in the curve fitting program. Using a standard nonlinear least-squares fit to Eq. (1b), we find  $n = 8.31 (\pm 0.11) \times 10^{14}$  cm<sup>-3</sup> and  $\mu = 1.08 (\pm 0.12) \times 10^5$  cm<sup>2</sup>/V s. Taking  $m^* = 0.01m_0$ ,  $\tau = 6.14 (\pm 0.68) \times 10^{-13}$  s. The Hall coefficient (at  $B = 1$  kG) yields  $n = 8.83 \times 10^{14}$  cm<sup>-3</sup>,  $\mu = 1.07 \times 10^5$  cm<sup>2</sup>/V s, and  $\tau = 6.08 \times 10^{-13}$  s in good agreement.

Figures 2(a) and 2(b) show  $\sigma_{xy}$  vs  $H$  for a *p*-type InSb sample at 8 K. Figure 2(a) is an attempt to fit the data with a heavy-hole term only. Note that while the fit around the peak is satisfactory, the fit undercuts the data at low magnetic fields. In Fig. 2(b), both heavy- and light-hole carrier terms are included in order to accurately describe the data. By decomposing the fit into its constituent light- and heavy-hole terms, and identifying the peak coordinates,  $n$ ,  $\mu$ , and  $\tau$  may be determined for each type of carrier. Table I summarizes the numerical data found from both fits. In order to calculate  $\tau_i$  the following effective mass values were used:  $m^*$ (light holes) =  $0.015m_0$  and  $m^*$ (heavy holes) =  $0.45m_0$ .<sup>10</sup> Because the terms in the magnetoresistivity are additive,  $\sigma_{xy}$  plots yield much more information in the complex situations often encountered in the laboratory in terms of concentrations and types of carriers than

TABLE I. Summary of numerical data found by one-carrier and two-carrier fits of  $\sigma_{xy}$  data for *p*-type InSb at 8 K to Eq. (1b).

	Fig. 2(a) One-carrier fit	Fig. 2(b) Two-carrier fit
Light holes		
$p$ (cm <sup>-3</sup> )		$2.82 (\pm 0.06) \times 10^{12}$
$\mu$ (cm <sup>2</sup> /V s)		$5.08 (\pm 0.46) \times 10^4$
$\tau$ (s)		$4.32 (\pm 0.39) \times 10^{-13}$
Heavy holes		
$p$ (cm <sup>-3</sup> )	$4.23 (\pm 0.09) \times 10^{11}$	$4.28 (\pm 0.05) \times 10^{11}$
$\mu$ (cm <sup>2</sup> /V s)	$1.81 (\pm 0.36) \times 10^4$	$1.48 (\pm 0.01) \times 10^4$
$\tau$ (s)	$4.62 (\pm 0.92) \times 10^{-12}$	$3.79 (\pm 0.03) \times 10^{-12}$
Standard deviation	$8.20 \times 10^{-5}$	$4.57 \times 10^{-6}$

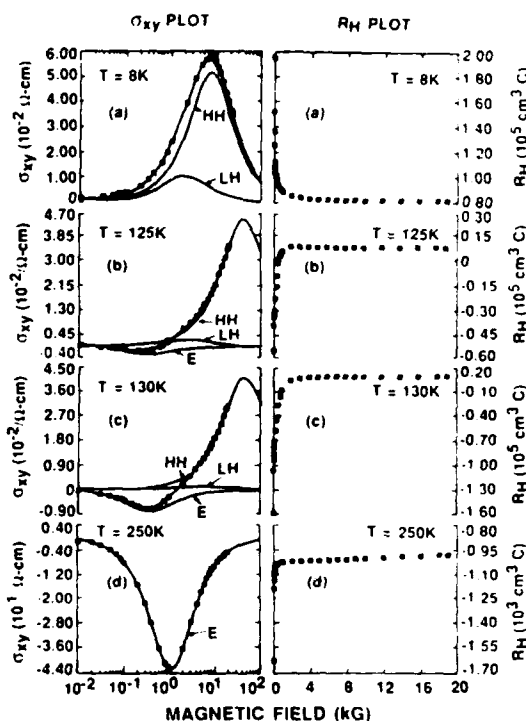


FIG. 3. Comparison of the Hall coefficient and  $\sigma_{xy}$  plots for *p*-type InSb for various temperatures (a) 8 K, (b) 125 K, (c) 130 K, (d) 250 K. Note the sensitivity of the  $\sigma_{xy}$  plot to small changes in temperature.

do standard Hall coefficient plots. An example of this is seen in Fig. 3 where the  $\sigma_{xy}$  plots are compared with their corresponding Hall coefficient plots for a *p*-InSb sample for  $T = 8$ –250 K. The  $\sigma_{xy}$  curve at 8 K indicates that there are both light holes and heavy holes present, as discussed previously. In addition to the light and heavy holes already present, electronic contributions to conduction are apparent as  $\sigma_{xy}$  takes on negative values at low fields at 125 K. Note that the small concentrations of electrons present (on the order of  $10^{11}$  cm<sup>-3</sup>) relative to the concentration of heavy holes present (on the order of  $10^{14}$ ) are much more apparent in the  $\sigma_{xy}$  curve than in the corresponding Hall plot. At 130 K, a temperature change of only 5 K, the  $\sigma_{xy}$  curve has changed noticeably in both the height and critical magnetic field of the electron peak. Because of the large concentration of heavy holes and relatively small change in concentration of

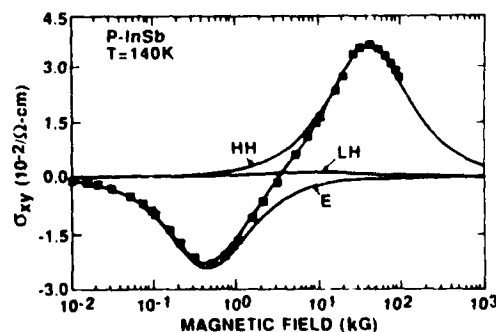


FIG. 4. Three-carrier fit of  $\sigma_{xy}$  data for *p*-type InSb at 125 K. Data taken at Francis Bitter National Magnet Lab.

TABLE II. Numerical data obtained by a three-carrier fit of  $\sigma_{xx}$  data for  $p$ -type InSb at 140 K.

	Electrons	Heavy holes	Light holes
$n(\text{cm}^{-3})$	$1.44(\pm 0.02) \times 10^{12}$	$1.75(\pm 0.02) \times 10^{14}$	$1.50(\pm 1.49) \times 10^{12}$
$\mu(\text{cm}^2/\text{V s})$	$2.18(\pm 0.28) \times 10^5$	$2.52(\pm 0.05) \times 10^5$	$1.14(\pm 0.69) \times 10^4$
$\tau(\text{s})$	$5.57(\pm 0.72) \times 10^{-11}$	$6.44(\pm 0.13) \times 10^{-11}$	$2.91(\pm 1.76) \times 10^{-10}$

electrons, the Hall coefficient curve is not significantly changed. At 250 K, the conduction is mainly due to electrons as shown by the one carrier band fit. Overall, the  $\sigma_{xy}$  components, which can be easily decomposed, are much more illustrative in their description of transport properties than corresponding Hall coefficient plots.

Because of the low mobility of the predominant heavy holes, peaks in the  $\sigma_{xy}$  plots are not always possible to observe with low magnetic fields, thus making quantitative fitting difficult. Figure 4 shows the results of high field measurements made at the Francis Bitter National Magnet Laboratory on a  $p$ -type InSb sample at 140 K that quantitatively demonstrates the sensitivity of our technique. In this sample, we are able to quantitatively characterize light holes, heavy holes, and electrons. Numerical values are summarized in Table II. In calculating  $\tau_i$ , we have used  $m^*$  (light holes) =  $0.015m_0$ ,  $m^*$  (heavy holes) =  $0.45m_0$ , and  $m^*$  (electrons) =  $0.01m_0$ .<sup>10</sup> We find that the value obtained through the fit for the concentration and mobility of light holes is very reasonable compared to the number and mobility of the heavy holes present.

Figures 5(a) and 5(b) show the application of this

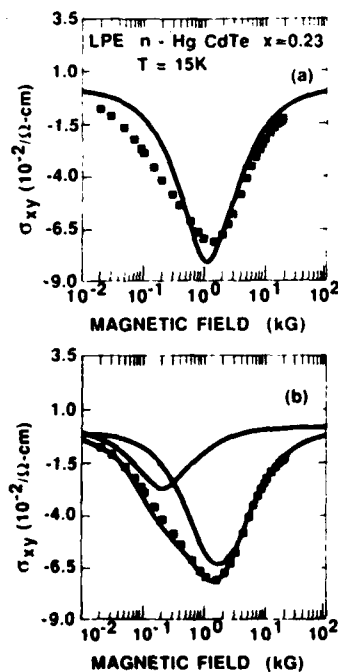


FIG. 5. (a) One-carrier fit. We find  $1.16(\pm 0.08) \times 10^{11} \text{ cm}^{-3}$  electrons with a mobility of  $8.90(\pm 0.58) \times 10^4 \text{ cm}^2/\text{V s}$ . (b) Two-electron fit. We find  $n_1 = 1.35(\pm 0.19) \times 10^{11} \text{ cm}^{-3}$ ,  $\mu_1 = 5.98(\pm 0.14) \times 10^4 \text{ cm}^2/\text{V s}$  and  $n_2 = 8.08(\pm 0.69) \times 10^{11} \text{ cm}^{-3}$ ,  $\mu_2 = 4.43(\pm 0.23) \times 10^5 \text{ cm}^2/\text{V s}$ . The Hall coefficient finds  $5.24 \times 10^{11}$  carriers  $\text{cm}^{-3}$  with mobilities of  $4.5 \times 10^4 \text{ cm}^2/\text{V s}$  at  $B = 1 \text{ kG}$  and  $1.71 \times 10^{14}$  carriers  $\text{cm}^{-3}$  with mobilities of  $1.4 \times 10^5 \text{ cm}^2/\text{V s}$  at  $B = 10 \text{ kG}$ .

method to an epitaxially grown  $n$ -type LPE  $\text{Hg}_{1-x}\text{Cd}_x\text{Te}$  sample ( $x \approx 0.23$ ) at 15 K. This sample exhibited anomalous transport properties, i.e., a low mobility at low temperatures and peaks in both the Hall coefficient and mobility versus temperature data. Figure 5(a) shows an attempt to describe the  $\sigma_{xy}$  data using one carrier (electron), as would be expected for  $n$ -type conduction. It is seen that the conduction mechanisms in this sample are more complicated, as evidenced by the inability of the one-carrier model to adequately describe the  $\sigma_{xy}$  data. Subsequent attempts using combined electron and hole conduction to describe the data were equally unsuccessful. Figure 5(b) shows, however, that the data can be satisfactorily explained by using two electrons of vastly different mobility and concentration. These values are given in the caption of Fig. 5. We note that two-electron conduction has been previously reported by Finkman and Nemirovsky in bulk  $n$ -type  $\text{HgCdTe}$ .<sup>11</sup> In addition, a previous study<sup>12</sup> on LPE  $\text{HgCdTe}$  invoked a model of  $p$ -type inclusions in an  $n$ -type matrix to describe the anomalous carrier transport properties. However, our  $\sigma_{xy}$  data show no evidence of holes contributing to conduction in these anomalous samples.

Because of its simplicity and sensitivity to minority carriers, we predict that magnetoconductivity tensor analysis will join Hall coefficient and magnetoresistance analysis as a standard characterization tool in the semiconductor industry, applicable not only to bulk materials, but also to thin films and the new generations of artificially structure materials.

We acknowledge the partial support of this work by Texas Instruments and a Faculty Research Grant from North Texas State University. We thank Dr. D. Weirauch for providing the LPE samples and Professor Wlodek Zawadzki for his helpful comments.

<sup>1</sup>G. G. Grenier, J. M. Reynolds, and J. R. Sybert, *Phys. Rev.* **132**, 58 (1963).

<sup>2</sup>J. R. Sybert, H. J. Mackey, and K. L. Hathcox, *Phys. Rev.* **166**, 710 (1968).

<sup>3</sup>J. W. McClure, *Phys. Rev.* **112**, 715 (1958).

<sup>4</sup>A. C. Beer, *Galvanomagnetic Effects in Semiconductors* (Academic, New York, 1963).

<sup>5</sup>A. H. Wilson, *The Theory of Metals*, 2nd ed. (Cambridge University, Cambridge, 1953).

<sup>6</sup>B. R. Nag, *Electron Transport in Compound Semiconductors* (Springer, New York, 1980).

<sup>7</sup>Z. Dziuba and R. Kowalczyk, *Phys. Status Solidi B* **119**, K11 (1983).

<sup>8</sup>W. Zawadzki, in *Handbook on Semiconductors*, edited by W. Paul (North-Holland, New York, 1982), Vol. 1, p. 713.

<sup>9</sup>P. Pfeffer and W. Zawadzki, *Phys. Status Solidi B* **88**, 247 (1978).

<sup>10</sup>C. L. Littler, D. G. Seiler, R. Kaplan, and R. J. Wagner, *Phys. Rev. B* **27**, 7473 (1983).

<sup>11</sup>E. Finkman and Y. Nemirovsky, *J. Appl. Phys.* **53**, 1052 (1982).

<sup>12</sup>M. C. Chen, S. G. Parker, and D. F. Weirauch, *J. Appl. Phys.* **58**, 3150 (1985).

# Determination of minority-carrier lifetimes in *p*-type narrow band-gap semiconductors with two-photon absorption excitation

M. R. Loloee, D. G. Seiler,<sup>a)</sup> and G. B. Ward

Center for Applied Quantum Electronics, Department of Physics, University of North Texas, Denton, Texas 76203

(Received 14 July 1988; accepted for publication 22 September 1988)

A novel method for the direct experimental determination of true minority-carrier (electron) lifetimes in *p*-type narrow band-gap semiconductors is presented. Specific results are given for *p*-InSb showing recombination involving a deep level close to midgap as the dominant recombination mechanism.

The minority-carrier lifetime is an important critical parameter in controlling the performance of infrared photodetectors based on narrow gap semiconductors like InSb or  $\text{Hg}_{1-x}\text{Cd}_x\text{Te}$  alloys. In many cases, the minority-carrier lifetime  $\tau$  is limited by deep levels of impurities or defects or traps that are present in the material, and hence a measurement of the temperature dependence of  $\tau$  gives information about these levels. Determinations of  $\tau$  usually rely on photoconductivity decay measurements and lasers with photon energies greater than the band gap of the material [e.g., GaAs diode lasers ( $\lambda = 0.9 \mu\text{m}$ ) or a HeNe laser ( $\lambda = 3.39 \mu\text{m}$ )].<sup>1-3</sup> Unfortunately, the photoconductive decay can be complex showing multistage behavior leading to difficulties in extracting a true value for  $\tau$ . Also, the large photon energies used means that surface effects can play a dominant and misleading role. In this letter, we show how to overcome these difficulties by using (1) a new method—the magneto-photoconductivity (MPC) tensor component method and (2) two-photon absorption (TPA) techniques. Results for high quality samples of *p*-InSb are reported here (electrons are the minority carriers) and are in reasonable agreement with earlier photoelectromagnetic effect studies.<sup>4-8</sup>

We have recently reported the development of a novel characterization method to determine the carrier concentration and mobility of majority and minority carriers in multi-carrier systems using magnetoconductivity tensor (MCT) components.<sup>9</sup> The magnetoconductivity tensor components may be written as:

$$\sigma_{xx} = \frac{\rho_{xx}}{\rho_{xx}^2 + R_H^2 H^2} \approx \sum_{i=1}^M \frac{n_i |e| H_i}{H_i^2 + H^2} \quad (1a)$$

and

$$\sigma_{xy} = \frac{R_H H}{\rho_{xx}^2 + R_H^2 H^2} \approx \sum_{i=1}^M \frac{n_i e H}{H_i^2 + H^2}, \quad (1b)$$

where  $\rho_{xx}$  and  $R_H$  are the standard measured quantities of transverse magnetoresistance and Hall coefficient, respectively,  $M$  is the number of carrier types,  $H_i \approx 1/\mu_i = m^* \tau_i e$  is the critical magnetic field in which  $\mu_i$  and  $\tau_i$  are average quantities, and  $n_i$  is the concentration of carriers of type  $i$  ( $e < 0$  for electrons). Although this method was applied to multicarrier analysis of dark thermal equilibrium carriers, it

is also applicable to analyzing and studying photoexcited carriers under laser excitation conditions. This permits the extraction of true minority-carrier lifetimes in *p*-type semiconductors as opposed to the often ambiguous results obtained by photoconductivity techniques.

The samples used were cut from bulk grown *p*-type InSb having a concentration of  $1.7 \times 10^{14} \text{ cm}^{-3}$  and a Hall mobility of  $1.2 \times 10^4 \text{ cm}^2/\text{Vs}$  at 77 K. The resistivity and Hall contacts were made in a standard configuration to simultaneously measure both the photoconductive (PC) and photo-Hall (PH) responses.  $\text{CO}_2$  laser pulses were obtained from a rotating mirror *Q*-switch arrangement that could provide high intensities (up to  $500 \text{ kW/cm}^2$ ) and had full width at half maximum pulse widths of  $\approx 98 \text{ ns}$ . The laser pulses were focused onto the region of the sample between the potential contacts and a separate pair of Hall contacts. The magneto-photoconductive and photo-Hall transient responses were captured by a Tektronix transient digitizer. Time-resolved PC measurements were taken in order to compare with the results obtained from MPC study. The PC response for different temperatures is shown in Fig. 1 for  $\lambda = 9.25 \mu\text{m}$  and  $I = 50 \text{ kW/cm}^2$ . The PC response has a single exponential decay for  $30 < T < 100 \text{ K}$  and two stages of decay at  $T < 30 \text{ K}$  or  $T > 100 \text{ K}$ . At  $9.25 \mu\text{m}$  ( $2\hbar\omega = 267.9 \text{ meV}$ ), TPA effects occur at all temperatures since  $2\hbar\omega > E_g$ , the energy gap; however, the recombination mechanisms controlling the PC response are very complex, as seen in Fig. 1. In Fig. 2 we

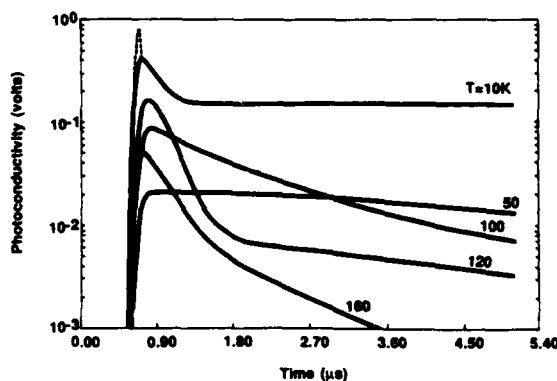


FIG. 1. Temperature dependence of the ac photoconductive response obtained for  $\lambda = 9.25 \mu\text{m}$  and  $I = 50 \text{ kW/cm}^2$ . The waveforms have two stages of decay for  $T < 30 \text{ K}$  and  $T > 110 \text{ K}$ . The dashed line represents the laser pulse.

<sup>a)</sup> Current address: National Institute of Standards and Technology, Materials Technology Group, Semiconductor Electronics Division, Center for Electronics and Electrical Engineering, Gaithersburg, MD 20899.

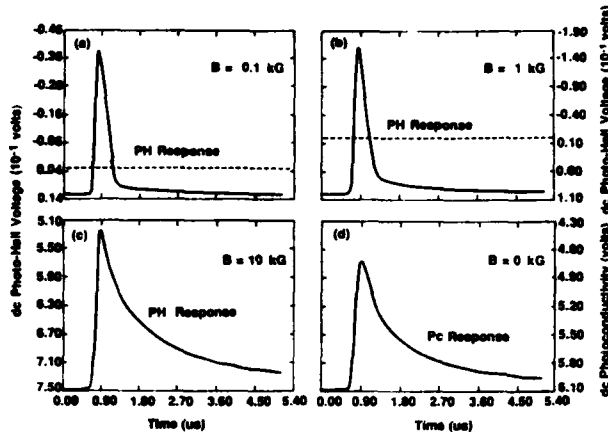


FIG. 2. Time-resolved dc PH and PC responses for  $T = 100$  K. (a) and (b) show the PH response at  $B = 0.1$  and  $1$  kG, whereas (c) and (d) show the similarity of the PH response at  $B = 10$  kG with the PC response at  $B = 0$ .

show that at low magnetic field strengths the PH response behaves differently from the PC response and thus contains additional information about recombination mechanisms, if it can be properly analyzed. In Figs. 2(a) and 2(b) the dc PH response is plotted for  $B = 0.1$  and  $1$  kG. Note that for this low field region, the PH response has negative values over part of the waveform when the laser pulse is incident on the sample. Since  $R_H > 0$  implies hole domination and  $R_H < 0$  electron domination, the switch over from positive  $R_H$  values in the dark to negative  $R_H$  values (as seen by the negative Hall voltages) when laser light is incident on the sample implies photoexcited electrons are observed. Figures 2(c) and 2(d) show the similarity of the PH response at  $B = 10$  kG and the PC response, respectively, where no negative voltage (photoexcited electron contribution) was observed in the PH response. In order to unravel this complex behavior, we now show how the MCT component method can be used to great advantage. The dark  $\sigma_{xy}$  data in Fig. 3 were obtained for four different temperatures by our recently reported method.<sup>9</sup> By using a standard nonlinear least-squares fitting method with Eq. (1b), we are able to separate multicarrier components as well as collecting numerical

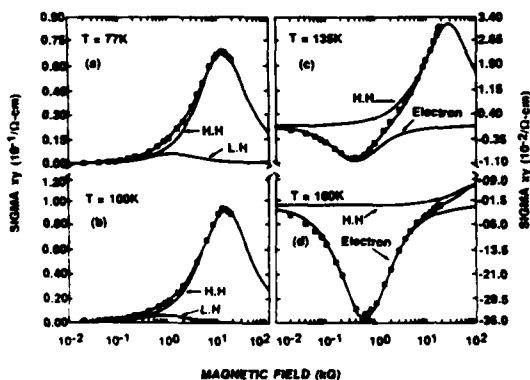


FIG. 3.  $\sigma_{xy}$  vs  $\ln H$  plots in the dark for various temperatures: (a)  $77$  K, (b)  $110$  K, (c)  $135$  K, and (d)  $160$  K. The sensitivity of the  $\sigma_{xy}$  component to small changes in temperature is readily apparent in the figures.

data on individual carrier concentrations and mobilities. For  $77$  and  $100$  K, only heavy holes and light holes are present, while for  $T = 135$  K, the presence of as few as  $5.3 \times 10^{11} \text{ cm}^{-3}$  minority-carrier electrons (thermally excited across the band gap) can be seen. For  $T = 160$  K,  $2.6 \times 10^{13} \text{ cm}^{-3}$  intrinsic electrons thermally excited across the gap totally dominate the transport at low magnetic fields.

Laser excitation with a  $\text{CO}_2$  laser pulse ( $\lambda = 9.25 \mu\text{m}$ ) creates a uniform distribution of electron-hole pairs by TPA processes. Minority-carrier electrons can thus be observed and studied. (Note that for  $T > 50$  K, TPA occurs over the  $9\text{--}10 \mu\text{m}$  range.) Figure 4 shows the results of our TPA photoexcitation studies. The  $T = 50$  K plots of  $\sigma_{xy}$  versus magnetic field in Fig. 4(a) show four sets of data with theoretical curves: (1) in the dark, at a time before the laser pulse is incident on the sample, (2) at the peak of the signal,  $325$  ns after the start of the laser pulse, (3)  $435$  ns after, and (4)  $515$  ns after. The peak of the signal occurs at the end of the laser pulse. Figures 4(b) and 4(c) are the results of nonlinear least-squares fitting in which we find, in the dark,  $p(\text{heavy}) = 1.2 \times 10^{14} \text{ cm}^{-3}$  with  $\mu = 2.2 \times 10^4 \text{ cm}^2/\text{V s}$  and  $p(\text{light}) = 1.1 \times 10^{12} \text{ cm}^{-3}$  with  $\mu = 1.7 \times 10^5 \text{ cm}^2/\text{V s}$ . Under irradiation of intensity  $I = 50 \text{ kW}/\text{cm}^2$ , the number of photoexcited electron minority carriers is  $n = 3.7 \times 10^{12} \text{ cm}^{-3}$  with  $\mu = 1.6 \times 10^4 \text{ cm}^2/\text{V s}$ . These novel measurements and analysis thus provide directly the number of photoexcited minority carriers (electrons in the conduction band)  $\Delta n$  as a function of time. In Fig. 5 we show the number of photoexcited electrons  $\Delta n$  versus time for  $T = 100$  and  $160$  K by using the MPC technique. Note that the technique is extremely sensitive to the number of minority-carrier electrons  $= 4.5 \times 10^{10} \text{ cm}^{-3}$  photoexcited electrons on a background of  $1.7 \times 10^{14} \text{ cm}^{-3}$  holes at  $T = 100$  K. For comparison purposes, we also plot the time variation of the PC response which possesses a single-stage decay for  $T = 100$  K and a two-stage decay for  $T = 160$  K. This semilog plot allows the extraction of an electron lifetime  $\tau_n = 88$  ns at  $T = 100$ , which is much shorter than the lifetime implied by the PC response. At  $T = 160$  K,  $\tau_n = 356$  ns and the time dependence of the photoexcited minority-carrier concentration follows the first (short) stage of the PC response. We

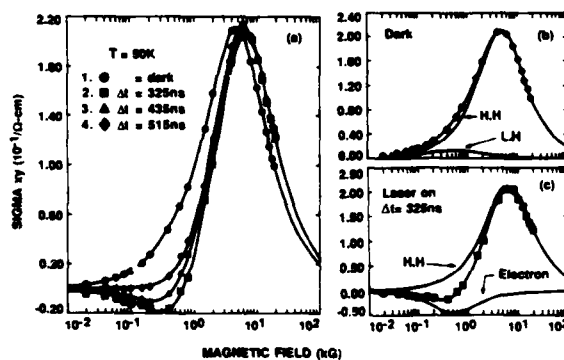


FIG. 4. (a) Time-resolved  $\sigma_{xy}$  data for  $T = 50$  K showing the creation of photoexcited electrons in the conduction band via TPA processes. (1) Dark, (2)  $325$  ns after the start of the laser pulse, (3)  $435$  ns after, and (4)  $515$  ns after. (b) and (c) show two-carrier fits of  $\sigma_{xy}$  data in the dark and  $325$  ns after the start of the laser pulse.



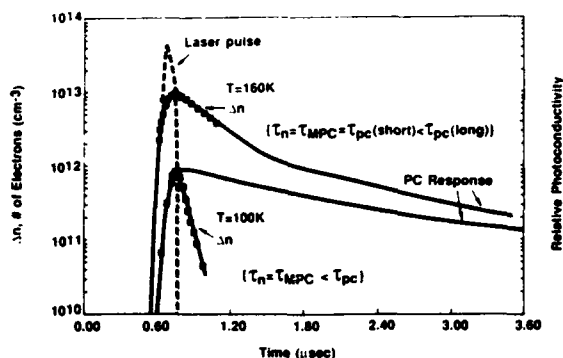


FIG. 5. Time dependence of minority electron concentration ( $\Delta n$ ) obtained by the MPC technique for  $T = 100$  and  $160$  K. For comparison purposes, solid lines show the actual PC response for each temperature.

also note that the magnitude of the PC response is much larger at  $100$  K than at  $160$  K. At  $100$  K, the PC response is dominated by impurity/defect absorption which creates only holes, which have a long lifetime. The presence of the much smaller quantity of minority-carrier electrons produced by TPA processes can only be detected by the much more sensitive MPC method presented here. At  $160$  K, impurity/defect absorption no longer dominates,  $\Delta n \approx \Delta p$ ,  $\mu_e \gg \mu_p$ , and hence the first-stage decay of the PC response is due to the decrease in the number of minority-carrier electrons, in agreement with the MPC method. For both cases at long times, all minority-carrier electrons are trapped, and the PC response is then controlled by hole recombination.

Comparison of the temperature dependence of the minority-carrier lifetime obtained from the MPC method and the lifetime obtained from the first-decay stage of the PC response is shown in Fig. 6. Assuming a single defect level in the energy gap, the minority-carrier lifetime dependence on

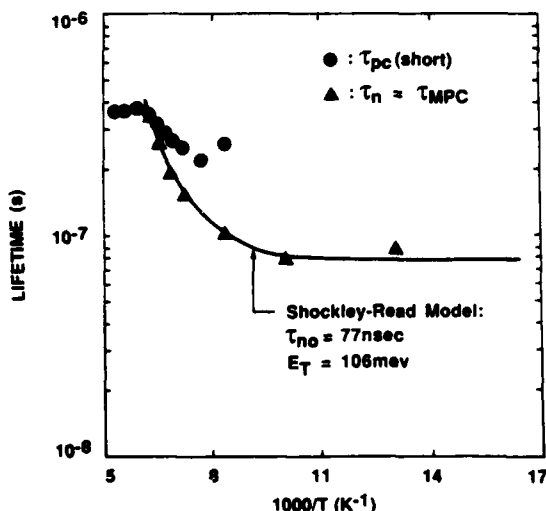


FIG. 6. Lifetime of minority electrons  $\tau_n$ , and the first stage of the PC response  $\tau_{PC}(\text{short})$  for  $T > 110$  K vs temperature. A trap energy of  $106$  meV is indicated by the fit to the Shockley-Read theory.

temperature can be explained by a Shockley-Read lifetime dependence as<sup>10</sup>

$$\tau_{SR} = \tau_n \frac{(n_0 + n_1 + \delta_n)}{n_0 + p_0 + \delta_n} + \tau_p \frac{(p_0 + p_1 + \delta_p)}{n_0 + p_0 + \delta_n}, \quad (2)$$

where  $\tau_n = (C_n N_t)^{-1}$  and  $\tau_p = (C_p N_t)^{-1}$ ,  $N_t$  is the trap density.  $C_n$  and  $C_p$  are the electron and the hole capture coefficient, respectively,  $n_1$  and  $p_1$  are the carrier concentrations for a Fermi level coincident with the trap level and defined as

$$n_1 = n_0 \exp[(E_t - E_f)/kT], \quad (3a)$$

$$p_1 = p_0 \exp[(E_f - E_t)/kT]. \quad (3b)$$

In the simple case where  $p_0 \gg n_0 \gg n_1$ ,  $\tau_p \gg \tau_n$ ,  $p_1 \gg p_0$ , and small  $\delta_n$ ,  $\delta_p$  one can write<sup>1,2</sup>

$$\tau_{SR} = \tau_n \left(1 + \frac{p_1}{p_0}\right) = \tau_n \left[1 + \exp\left(\frac{E_f - E_t}{kT}\right)\right]. \quad (4)$$

If the Fermi level falls below the level of the trap (at low temperatures), the lifetime is constant and equal to  $\tau_n$ . However, for  $E_f > E_t$ , the lifetime increases exponentially with increasing temperature. The energy of the Shockley-Read defect level extracted from the data using Eq. (4), is  $106$  meV above the valence band for a midgap level which agrees closely with the results tabulated by Seiler and Goodwin in Table I.<sup>11</sup> In the absence of the trap level,  $\tau_{MPC} = \tau_n = \tau_{PC}$ , but the experimental inequality of  $\tau_{MPC}$  and  $\tau_{PC}$  for  $T < 160$  K in Fig. 6 indicates that the analysis of the PC response cannot provide detailed information about minority-carrier electrons in  $p$ -type semiconductors.

In summary, we have shown that the magnetophotconductivity tensor component method is appropriate for studying minority-carrier lifetimes and determining carrier concentrations and mobilities of minority and majority carriers in narrow gap semiconductors. Use of different lasers will, of course, allow wider band-gap semiconductors also to be investigated by this method. Our future work will concentrate on samples of  $\text{Hg}_{1-x}\text{Cd}_x\text{Te}$ .

We acknowledge the partial support of this work by the U.S. Army Center for Night Vision and Electro-Optics, contract DAAB07-87-C-F094, and a faculty research grant from the University of North Texas.

<sup>1</sup>D. L. Polla, S. P. Tobin, M. B. Reine, and A. K. Sood, J. Appl. Phys. 52, 5182 (1981).

<sup>2</sup>D. E. Lacklison and P. Capper, Semicond. Sci. Technol. 2, 33 (1987).

<sup>3</sup>S. E. Schacham and E. Finkman, J. Appl. Phys. 57, 2001 (1985).

<sup>4</sup>R. N. Zitter, A. J. Strauss, and A. e. Attard, Phys. Rev. 115, 266 (1959).

<sup>5</sup>R. A. Laff and H. Y. Fan, Phys. Rev. 121, 53 (1961).

<sup>6</sup>D. N. Nasledov and Yu S. Smetannikova, Sov. Phys. Solid State 4, 78 (1962).

<sup>7</sup>J. E. L. Hollis, S. C. Choo, and E. L. Heasell, J. Appl. Phys. 38, 1626 (1967).

<sup>8</sup>A. S. Volkov and V. V. Galavanov, Sov. Phys. Semicond. 1, 129 (1967).

<sup>9</sup>D. L. Lealie-Pelecky, D. G. Seiler, M. R. Loloee, and C. L. Littler, Appl. Phys. Lett. 51, 1916 (1987).

<sup>10</sup>W. Shockley and W. T. Read, Jr., Phys. Rev. 87, 835 (1952).

<sup>11</sup>D. G. Seiler and M. W. Goodwin, J. Appl. Phys. 53, 7505 (1982).

**NEW LASER-BASED MAGNETO-OPTICAL STUDIES OF  $\text{Hg}_{1-x}\text{Cd}_x\text{Te}$  ALLOYS\***

D. G. Seiler, M. R. Loloee, S. A. Milazzo, A. J. Durkin

Center for Applied Quantum Electronics

Department of Physics

University of North Texas

P. O. Box 5368

Denton, Texas 76203

C. L. Littler

Central Research Laboratories

Texas Instruments

Dallas, Texas 75265

Abstract

Several magneto-optical effects are observed for the first time in a number of  $\text{Hg}_{1-x}\text{Cd}_x\text{Te}$  alloys. These include two-photon magnetoabsorption and optical transitions from both shallow acceptor levels and midgap levels to the conduction band. These effects yield accurate information about the energy band structure, the temperature dependence of the energy gap, and the activation energies of impurity and defect states present in the  $\text{Hg}_{1-x}\text{Cd}_x\text{Te}$  alloys.

Detectors fabricated using mercury cadmium telluride ( $\text{Hg}_{1-x}\text{Cd}_x\text{Te}$ ) alloys serve as extremely important components of modern infrared systems. Improvements in the sensitivity and performance of these detectors require a better understanding of the detector material's optical and electronic properties, along with improved sample characterization techniques. Specifically, information about the energy band structure and impurity or defect levels present in  $\text{Hg}_{1-x}\text{Cd}_x\text{Te}$  is essential to understanding and improving the performance of current infrared detectors. Consequently, it is highly desirable to develop and use new, sensitive techniques to aid in the characterization of these alloys.

In this paper we present new and important results on  $\text{Hg}_{1-x}\text{Cd}_x\text{Te}$  alloys using  $\text{CO}_2$  laser-based magneto-optical methods that include: (1) the first observation and analysis of two-photon magneto-absorption (TPMA) spectra; (2) the first observation of magneto-optical transitions of electrons from both midgap levels and shallow acceptor levels to the conduction band; and (3) the first observation of magneto-impurity spectra. In addition, analysis of two-photon spectra obtained at low temperatures reveals a nonlinear variation of the energy gap versus temperature not previously reported. The laser based magneto-optical techniques we present here for  $\text{Hg}_{1-x}\text{Cd}_x\text{Te}$  are generic and can easily be applied to other semiconductor or superlattice systems by using an appropriate combination of laser sources and magnetic fields.

The experiments reported here were carried out on single crystal, bulk grown n-type samples of  $\text{Hg}_{1-x}\text{Cd}_x\text{Te}$  with  $x = 0.236, 0.256$ , and  $0.280$ . All samples were polished, etched, and had indium contacts. They showed the normal temperature dependence of the Hall coefficient and resistivity. The output of a grating tunable cw  $\text{CO}_2$  laser was mechanically chopped into  $20 \mu\text{sec}$  wide pulses which were focused onto the samples mounted in a superconducting magnet in a transverse magnetoresistance geometry.

Photoconductivity (PC) measurements were used since they have been shown<sup>1-4</sup> to provide a sensitive means of determining small changes in absorption due to weak magneto-optical transitions. Boxcar averager techniques were used to record the PC response of the samples vs. magnetic field. An example of the PC spectra for several wavelengths is shown in Fig. 1 for a sample with

$x = 0.236$ . All of the observed resonant structure can be understood by a Landau-level and density-of-states model where peaks in the density-of-states occur at energies corresponding to the bottom of each Landau level. These peaks enhance the optical transition rates or the electron scattering rates. Optically created electrons in the conduction band then increase the conductivity or photoconductive response of the samples. Four different types of structure are observed depending upon which combination of laser wavelength, magnetic field, and laser intensity is used. First, at high magnetic fields, long wavelengths, and high intensities, two strong PC resonances are observed. We have identified these resonances as resulting from specific two-photon interband transitions from initial valence band Landau levels to final conduction band Landau levels. Secondly, at shorter  $\text{CO}_2$  wavelengths, smaller magnetic fields, and low laser intensities, one-photon interband transitions are seen as indicated by the short upward pointing arrows in Fig. 1. Just to the high field side of the largest one-photon absorption (OPA) peak is a broad resonance indicated by the long arrows. We identify this structure as resulting from electron transitions from a shallow acceptor to the lowest conduction band Landau level. The temperature dependence and time-resolved behavior of the PC response support this identification, as does the binding energy of 9.8 meV determined from the photon energy dependence presented in Fig. 2. We rule out bound excitons as a source of this resonance because the large width of the resonance (bound excitons produce a much narrower linewidth than do free excitons). We also note that the binding energy deduced from these experiments for the residual acceptor level in this n-type sample is consistent with that of either As,<sup>5</sup> Cu,<sup>6,7</sup> or Sb<sup>8</sup> residual impurities previously determined in p-type samples. A major significance of the work presented here is that it provides a new means of determining the presence of compensating shallow acceptors in n-type material. Finally, at low fields, shorter wavelengths, and high intensities a new set of structure which is periodic in reciprocal magnetic field and which does not depend upon laser wavelength is observed. This is seen in Fig. 1 on the low field side of the large OPA peak for  $\lambda = 9.29 \mu\text{m}$ . We attribute this structure to magneto-impurity resonances<sup>9</sup> which arise from inelastic scattering processes whereby free carriers resonantly exchange energy with a second carrier bound to a donor or acceptor impurity in the presence of a magnetic field. Hot-electron conditions are nec-

essary for this observation and these conditions are achieved by the photoexcitation of carriers into the conduction band by optical excitation across the band gap.

Theoretical calculations of transition energies versus field, shown in Figure 2 for each magneto-optical effect discussed, are in excellent agreement with the data. The Landau level energies were calculated using a modified Pidgeon-Brown model and the set of band parameters given by Weiler:<sup>10</sup>  $E_p = 19$  eV,  $\Delta = 1$  eV,  $\gamma_1 = 3.3$  eV,  $\gamma_2 = 0.1$ ,  $\gamma_3 = 0.9$ ,  $\kappa = -0.8$ ,  $F = -0.8$ ,  $q = 0.0$ , and  $N_1 = 0.0$ . Using either one or two-photon selection rules the transition energies can be calculated for the pertinent OPA and TPA transitions. The value of  $E_g$  is easily determined by fitting theoretical results to the data using  $E_g$  as an adjustable parameter. Weiler has shown<sup>10</sup> that exciton corrections are necessary to adequately describe OPA data in  $Hg_{1-x}Cd_xTe$ . Since exciton corrections are not expected to be significant for TPA, we sought a consistent description of both the TPA and OPA data while correcting only the OPA data for excitonic effects. By using a free exciton binding energy of 2 meV, satisfactory agreement with the OPA data was achieved.

Two-photon magneto-optical methods are the best means for accurately determining the energy gap of a semiconductor. For example, the high quality of the TPMA data shown in Fig. 1 and the corresponding analysis gives  $E_g = 121.8 \pm 0.5$  meV. Using the Hansen, Schmit, Casselman relation<sup>11</sup> and this value for  $E_g$ , we find  $x = 0.2360 \pm 0.0003$  for this sample. With this means to accurately determine  $E_g$ , we have measured the temperature dependence of  $E_g$  and found a nonlinear variation of  $E_g$  with  $T$  below 15 K, with  $E_g$  becoming independent of  $T$ .

We have observed TPA structure in a wide variety of samples with other  $x$ -values and even in p-type samples. Fig. 3 shows results for samples with  $x \approx 0.26$  and  $x \approx 0.28$ . The same two dominant TPA peaks seen in the  $x \approx 0.24$  sample are also characteristic features of the spectra. Once again theoretical calculations of  $2\hbar\omega$  versus  $B$  accurately describe these data as seen also in Fig. 2 with  $E_g = 155$  meV and  $E_g = 195$  meV for the two samples. In addition, polarization studies have been performed on the samples, verifying the  $\sigma_L$  selection rule dependence of this structure and thus confirming the TPA interpretation. Finally, a new feature is seen for  $x \approx 0.28$  sample--at higher fields two new resonances occur which can not theoretically be described by TPA processes.

We interpret these resonances as resulting from electron transitions to the conduction band from midgap impurity or defect levels known to be present in samples of  $\text{Hg}_{1-x}\text{Cd}_x\text{Te}$ .<sup>12</sup> Electron transitions from the midgap levels to the lowest conduction band Landau level were calculated and plotted in Fig. 2, yielding activation energies of 100 meV and 94 meV below the conduction band edge.

In summary, we report the first observations and analysis of several different types of magneto-optical transitions in samples of  $\text{Hg}_{1-x}\text{Cd}_x\text{Te}$ . These transitions arise from (1) TPMA processes, (2) shallow acceptor to conduction band absorption, (3) midgap defect or impurity levels to conduction band absorption. This is the first time that these magneto-optical effects have been observed and studied in  $\text{Hg}_{1-x}\text{Cd}_x\text{Te}$  alloys. In addition, magneto-impurity oscillations have been observed. The techniques presented here are accurate, convenient to use, and could be developed into routine tools for not only characterizing bulk samples of  $\text{Hg}_{1-x}\text{Cd}_x\text{Te}$ , but thin films and superlattices as well. These magneto-optical methods are completely general, and with appropriate choices of laser sources and magnetic fields, can be used to study a wide variety of semiconductor materials.

## References

Work at UNT supported in part by the U. S. Army Night Vision and Electro-Optics Center, Contract #DAA B07-87-C-F094.

1. D. G. Seiler, M. W. Goodwin, and M. H. Weiler, Phys. Rev. B 23, 6806 (1981).
2. M. W. Goodwin, D. G. Seiler, and M. H. Weiler, Phys. Rev. B 25, 6300 (1982).
3. D. G. Seiler and M. W. Goodwin, J. Appl. Phys. 53, 7505 (1982).
4. D. G. Seiler, K. H. Littler, and C. L. Littler, Semicond. Sci. Technol. 1, 383 (1986).
5. M. H. Kalisher, J. Crystal Growth 70, 369 (1984).
6. F. J. Bartoli, C. A. Hoffman, and J. R. Meyer, J. Vac. Sci. Technol. A 4, 2047 (1986).
7. M. C. Chen and J. H. Tregilgas, J. Appl. Phys. 61, 787 (1987).
8. M. C. Chen and J. A. Dodge, Sol. State Commun. 59, 449 (1986).
9. See for example, L. Eaves and J. C. Portal, J. Phys. C: Solid State Phys. 12, 2809 (1979).
10. M. H. Weiler, in Semiconductors and Semimetals (Academic Press, New York, 1981), R. K. Willardson and A. C. Beer, editors, Vol. 16, p. 119.
11. G. L. Hansen, J. L. Schmit, and T. N. Casselman, J. Appl. Phys. 53, 7099 (1982).
12. M. C. Chen, M. W. Goodwin, and T. L. Polgreen, J. Crystal Growth 86, 484 (1988).

Figure 1. Magneto optical spectra for a sample of  $\text{Hg}_{1-x}\text{Cd}_x\text{Te}$  with  $x = 0.236$ . At high fields and long wavelengths TPMA resonant structure is seen. At lower fields and lower wavelengths both one-photon magnetoabsorption (short arrows) and a much broader resonance (longer arrows) due to transitions from a shallow acceptor level to the conduction band are seen. Additional structure seen for  $\lambda = 9.29 \mu\text{m}$  and arises from the magneto-impurity effect.

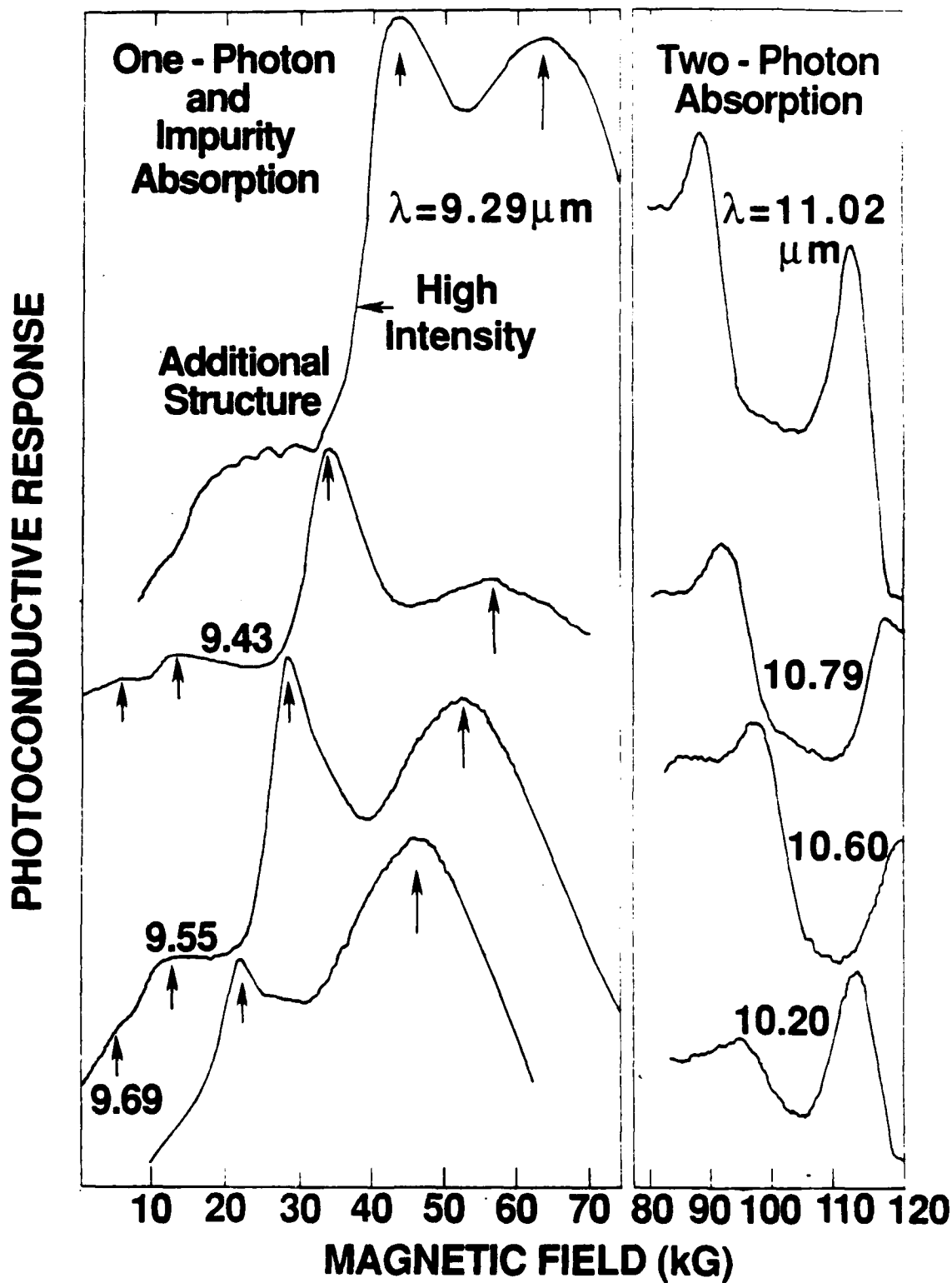




Figure 2. Fan chart plots of either one-photon ( $\hbar\omega$ ) or two-photon ( $2\hbar\omega$ ) transition energies versus magnetic field for three  $\text{Hg}_{1-x}\text{Cd}_x\text{Te}$  samples of different  $x$ -values. The three pairs of transitions in the upper half arise from two-photon absorption. In addition to the OPA and TPA transition energies shown, fan charts for shallow impurity-to-conduction and midgap level-to-conduction band transitions are shown. The activation energies are 9.8 meV above the valence band for the shallow acceptor level present in the  $x \approx 0.24$  sample and 94 and 100 meV below the conduction band for the  $x \approx 0.28$  sample.

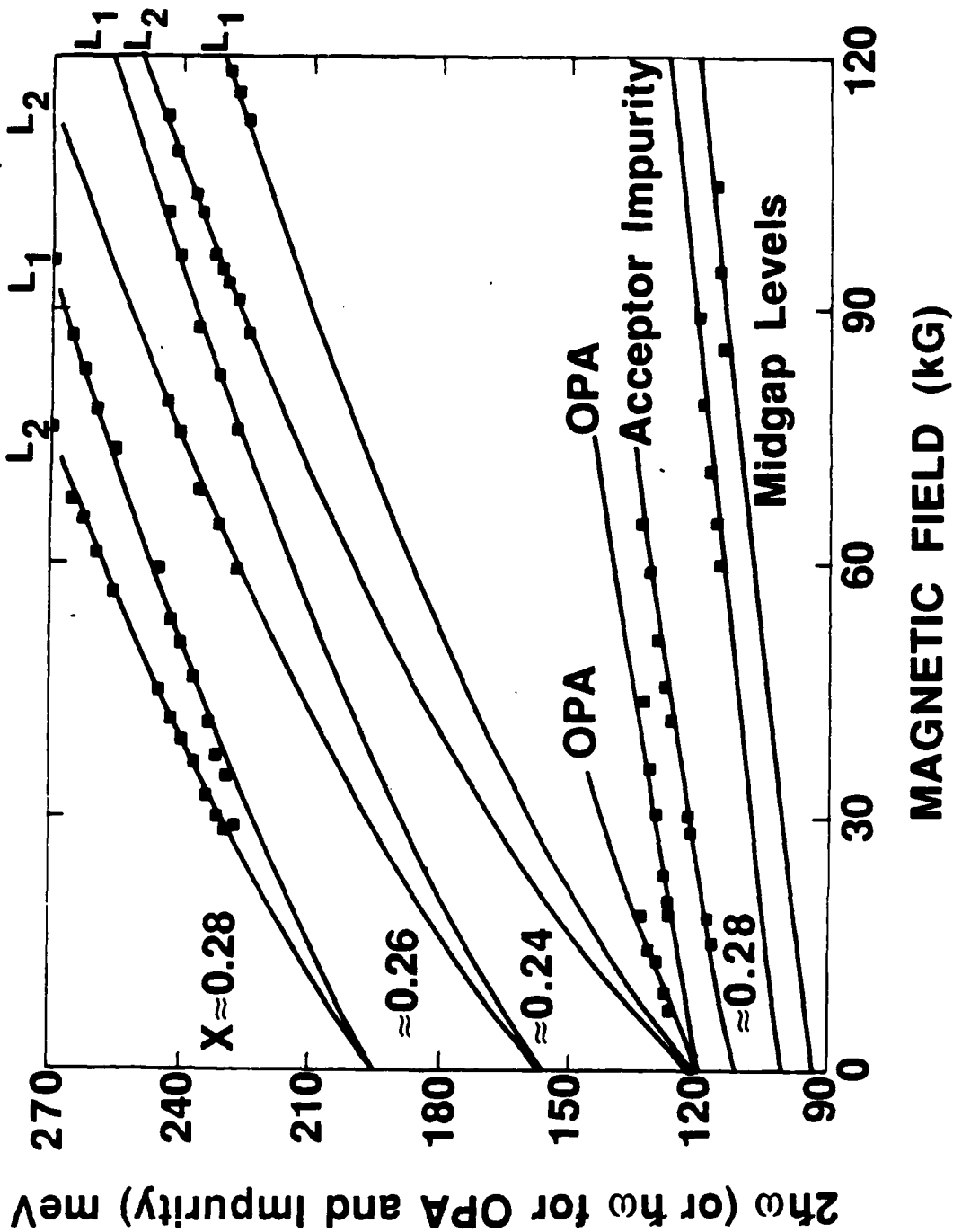
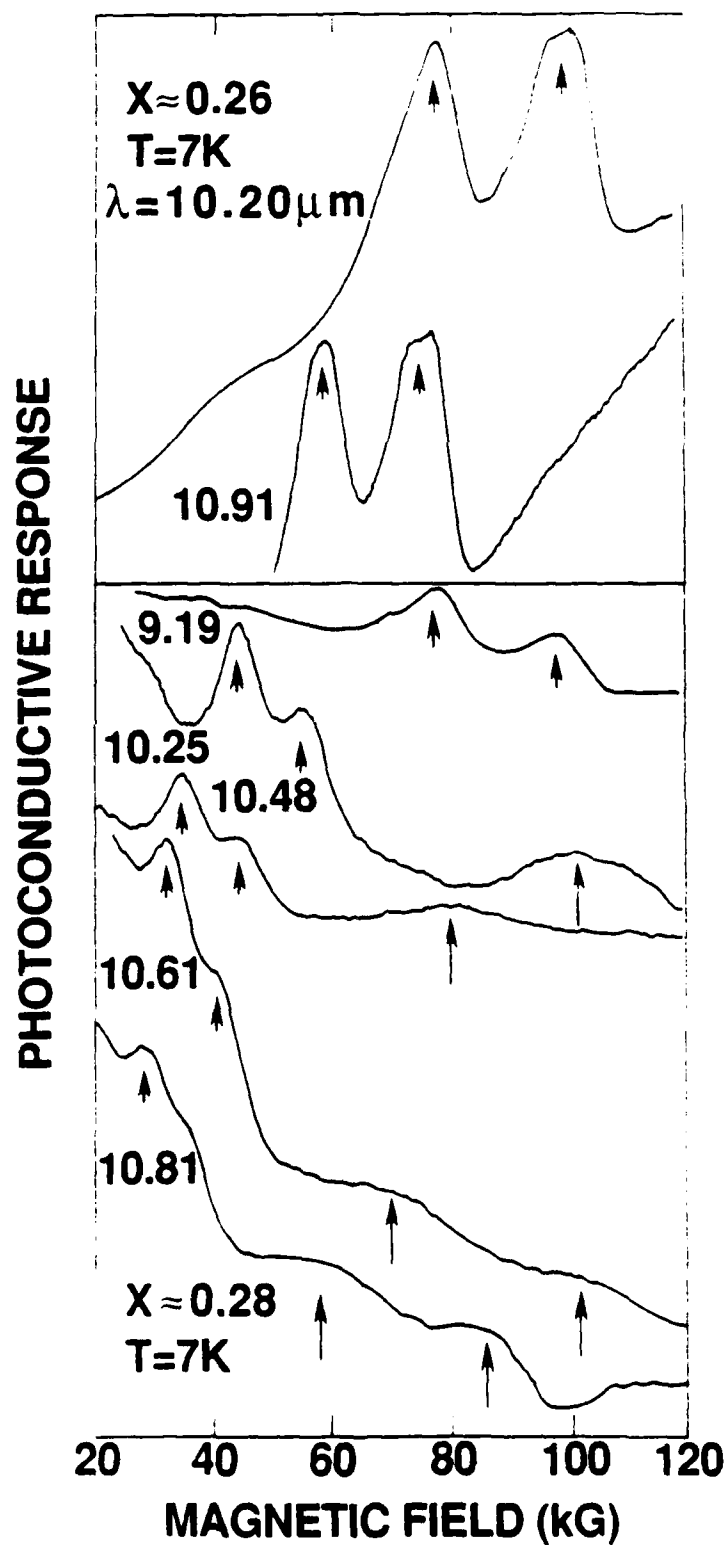


Figure 3. Magneto-optical spectra in two samples of  $\text{Hg}_{1-x}\text{Cd}_x\text{Te}$  with  $x \approx 0.26$  and  $x \approx 0.28$  showing TPA structure (short arrows) and midgap level to conduction band transitions (long arrows).



NONLINEAR MAGNETO-OPTICAL SPECTROSCOPY OF  $\text{Hg}_{1-x}\text{Cd}_x\text{Te}$   
BY TWO-PHOTON ABSORPTION TECHNIQUES

D. G. Seiler<sup>\*</sup>, C. L. Littler<sup>†</sup>, S. A. Milazzo, M. R. Loloee, A. J. Durkin

Center for Applied Quantum Electronics

Department of Physics

University of North Texas

Denton, Texas 76203

<sup>†</sup>Central Research Laboratories

Texas Instruments

Dallas, Texas 75265

In this paper we present new and important results on  $\text{Hg}_{1-x}\text{Cd}_x\text{Te}$  alloys using  $\text{CO}_2$  laser-based magneto-optical methods that include: (1) the observation and analysis of two-photon magneto absorption spectra in a variety of samples from  $x \approx 0.24$  to  $x \approx 0.30$ , and (2) the observation of magneto-optical transitions of electrons from both midgap levels and shallow acceptor levels to the conduction band Landau levels. These measurements allow the most accurate determination of the energy gap and binding energies associated with impurities and defects. In addition, analysis of the temperature dependence of two-photon spectra obtained on all samples investigated reveals a non-linear variation of the energy gap versus temperature not previously reported. The temperature dependence of the energy gap below 100 K cannot be explained by any of the currently used empirical relationships. The laser based magneto-optical techniques we present here for  $\text{Hg}_{1-x}\text{Cd}_x\text{Te}$  are generic and can easily be applied to other semiconductor or superlattice systems by using an appropriate combination of laser sources and magnetic fields.

### Introduction and Background

Mercury cadmium telluride ( $\text{Hg}_{1-x}\text{Cd}_x\text{Te}$ ) detectors serve as extremely important components of modern infrared detector systems. Improvements in sensitivity and performance require a better understanding of the alloy's optical and electronic properties, along with improved sample characterization techniques. New information about the energy band structure and impurity or defect levels present in  $\text{Hg}_{1-x}\text{Cd}_x\text{Te}$  is essential to understanding and improving the performance of current infrared detectors along with the development of future novel devices. Consequently, it is highly desirable to develop and use new, sensitive techniques such as the magneto-optical ones reported here to aid in the characterization of these alloys.

Over the past several decades magneto-optical studies of semiconductors have proven capable of accurately determining energy band parameters and impurity level information because of the optical transitions that occur between magnetically quantized electronic or impurity states. The use of lasers has now opened up the realm of nonlinear spectroscopy as a useful method for studying and characterizing semiconductors. Two-photon absorption (TPA) is one of the numerous nonlinear optical effects arising from  $\chi^3$ , the electric susceptibility tensor of the third order. In a previous study,<sup>1,2</sup> we have shown that two-photon absorption techniques can be used to determine TPA cut-off wavelengths and carrier lifetimes for samples of n- $\text{Hg}_{1-x}\text{Cd}_x\text{Te}$  with  $x \approx 0.31$ . In this paper we report extensive nonlinear magneto-optical results on  $\text{Hg}_{1-x}\text{Cd}_x\text{Te}$  alloys using TPA techniques. Resonant two-photon magnetoabsorption (TPMA) spectra are observed and studied in various n-type samples (from  $x \approx 0.24$  to  $x \approx 0.30$ ) and a p-type sample ( $x \approx 0.30$ ). The TPMA results provide the most accurate values of the fundamental energy gap, allowing the first observation of the "flattening" of  $E_g$  vs.  $T$  at temperatures less than 20K in  $\text{Hg}_{1-x}\text{Cd}_x\text{Te}$  alloys, a phenomena observed in most semiconductors.

The detection and identification of impurities or defects in semiconductor materials has long been a topic of technological importance. Of particular interest is their location within the forbidden energy gap region. Magneto-optical measurements have proven capable of locating both shallow<sup>3</sup> and deep<sup>4-6</sup> levels in n- or p-type InSb. We demonstrate in this paper that magneto-

optical measurements can also be used to detect and locate shallow and deep levels in  $\text{Hg}_{1-x}\text{Cd}_x\text{Te}$  alloys. Observation of one-photon and/or two-photon interband transitions aids in the identification of these levels.

### Experimental Work

The measurements reported here were carried out on single crystal samples of  $\text{Hg}_{1-x}\text{Cd}_x\text{Te}$  grown by solid-state recrystallization. A summary of the sample properties are given in Table I. The samples were rectangular slabs  $\approx 8 \text{ mm} \times 1 \text{ mm} \times 0.2 \text{ mm}$ , whose surfaces were lapped using alumina grit and then chem-mechanically polished using a 2% bromine-methanol solution. Electrical contacts were made to the samples using pure indium. The samples were electrically characterized prior to the magneto-optical measurements and showed the normal temperature dependence of the Hall coefficient and resistivity.

Figure 1 is a schematic diagram of the experimental apparatus used for the magneto-optical studies presented here. The output of a grating tunable cw  $\text{CO}_2$  laser was mechanically chopped into 20  $\mu\text{sec}$  wide pulses with a low duty cycle to prevent lattice heating effects. A zero-order waveplate was used to produce circularly polarized light and experimentally confirm the selection rule dependence of the observed two-photon magneto-optical resonances. The laser light was focused onto a sample placed in the solenoid of a superconducting magnet capable of producing DC magnetic fields as high as 120 kG. The direction of propagation of the laser light was parallel to the magnetic field, while the samples were mounted in a transverse magnetoresistance geometry with  $\vec{B} \parallel (111)$  crystal direction. The photoconductive (PC) response of the samples versus magnetic field, obtained under constant current, ohmic conditions, was monitored using a boxcar averager. The resulting magneto-optical spectra were then recorded on an x-y recorder.

### Results and Analysis

Figure 2 shows the PC response of an n-type sample #2 with  $x \approx 0.245$  for several  $\text{CO}_2$  laser wavelengths. Several absorption resonances are clearly resolved in the spectra. We identify the

structure as arising from two-photon absorption between specific valence band Landau levels and conduction band Landau levels. A modified Pidgeon-Brown energy-band model was used to calculate the valence energies for the two-photon or impurity/defect transitions observed. The transition energies for TPMA are given by

$$2 \hbar \omega = E_C^{a,b}(n_C, B) - E_V^{a,b}(n_V, B),$$

where  $\hbar \omega$  is the photon energy of the laser,  $E_C^{a,b}(n_C, B)$  represents the energies of the conduction band Landau levels in different spin states a or b.  $E_V^{a,b}(n_V, B)$  represents the energies of the valence band Landau levels, n is the Landau level number, B is the magnetic field, and the zero of energy is at the top of the valence band. The TPMA spherical selection rules are  $\Delta n = 0, \pm 2$  where  $\Delta n$  is the change in Landau level quantum number for a given transition.

A strong selection rule dependence of the TPMA transitions was experimentally found using left circularly polarized ( $\sigma_L$ ) and right circularly polarized ( $\sigma_R$ ) laser light as shown in Figure 3. Two-photon absorption is strongest for  $\Delta n = +2$  using left circularly polarized light. According to second order perturbation theory, the TPA transition probabilities are proportional to the product of two matrix elements. In the "intra-inter band" scenario, one matrix element represents an intraband transition, while the other, an interband one. Thus the strong resonances for  $\sigma_L$  polarization are not unexpected since the strongest intraband matrix element would be for the  $\sigma_L$  or cyclotron resonance case.

Figure 4 shows a comparison of theoretically calculated and experimentally determined two-photon transition energies versus magnetic field B. Various possible TPMA transitions are given in Table II along with the polarization needed for their observation, and symbols designating these transitions. Hereafter we shall use the designations given in Table II to describe the transitions. We obtain excellent agreement between theory and experiment using Weiler's<sup>7</sup> set of energy band parameters:  $E_p = 19.0$  eV,  $\Delta = 1.0$  eV,  $\gamma_1 = 3.3$ ,  $\gamma_2 = 0.1$ ,  $\gamma_3 = 0.9$ ,  $F = -0.8$ ,  $q = 0$ ,  $N_1 = 0$ , and

$\kappa = -0.8$ . The energy gap extracted from Figure 4 for this sample was  $E_g = 136.0 \pm 0.5$  meV, which yields  $x = 0.2448$  using the Hansen, Schmit, and Casselman<sup>8</sup> (HSC) relation. We see from Figure 4 that TPMA provides a very accurate means for measuring the energy gap of  $\text{Hg}_{1-x}\text{Cd}_x\text{Te}$ ; the two strongest transitions  $L_1$  and  $L_2$  are well described by the theoretical model. As a result, we have studied the temperature dependence of  $E_g$  for a variety of  $x$ -value samples. An example of the temperature dependence of the TPMA spectra for sample #1 ( $x \approx 0.236$ ) is shown in Figure 5. We see that the magnetic field positions of the two strong TPMA resonances are relatively independent of temperature from 2K to 15K, and shift to lower magnetic field at higher temperatures. This data was analyzed using the Pidgeon-Brown energy band model by adjusting only the value of  $E_g$  in order to fit the TPMA transition energy versus magnetic field positions. The TPMA results for the energy gap dependence on temperature are shown in Figure 6, and compared to the predictions of HSC.<sup>8</sup> We see that the energy gap data is relatively independent of temperature between 2K and 15K, increases more rapidly than predicted from the HSC relation between 20 to 100K, and finally above 100K has a slope that can be explained by the HSC relation.

Figure 5 also shows one-photon magnetoabsorption (OPMA) spectra at lower magnetic fields obtained with  $\lambda = 9.33 \mu\text{m}$ . This data also shows directly that the OPMA resonance positions are independent of temperature below  $\approx 15$  K, indicating that the  $E_g$  versus  $T$  dependence becomes independent of temperature. A more detailed calculation and analysis of this OPMA data using a modified Pidgeon-Brown energy-band model and one-photon selection rules to calculate the one-photon transition energies gives quantitative agreement with the TPMA results presented in Fig. 6.

The wavelength dependence of the TPMA structure for sample #1 ( $x \approx 0.236$ ) is shown in Figure 7. As seen for sample #2 (Fig. 2), two strong resonances at high fields are clearly observed and are related to  $\sigma_L$  transitions  $L_1$  and  $L_2$ . The wavelength independent structure is ascribed to magneto-impurity resonances resulting from inelastic scattering processes involving the TPA produced carriers. A similar sort of wavelength independent structure can also be seen for one-photon excitation conditions as shown in Fig. 8 for shorter wavelengths and lower magnetic fields. In both cases these magneto-impurity resonances arise from inelastic scattering processes whereby free car-

riers resonantly exchange energy with a second carrier bound to a donor or acceptor impurity in the presence of a magnetic field. Hot-electron conditions are necessary for the observation of these resonances, which are obtained here by photoexcitation of carriers into the conduction band by optical excitation (either one or two-photon) across the band gap. Two other resonances are also seen in Fig. 8: one-photon magnetoabsorption resonances are indicated by the short arrows and a broad absorption peak by the long arrow. In the case of the broad peak, the temperature dependence and time-resolved behavior of the PC response indicate that this absorption peak results from electron transitions from a shallow acceptor or Hg vacancy level to the lowest conduction band Landau level, as does the activation energy of  $9.8^{9-12}$  meV extracted from the calculations presented in Figure 9. This activation energy is consistent with both shallow acceptor impurities and the lowest Hg vacancy level<sup>10</sup> in  $\text{Hg}_{1-x}\text{Cd}_x\text{Te}$ . Figure 9 also shows a comparison of theoretical calculations for the TPMA ( $L_1$  and  $L_2$  structure) and OPMA transitions versus magnetic field with the data all obtained on sample #1. Excellent agreement between theory and data is clearly seen for both the TPMA and OPMA results. Since exciton corrections have been shown previously<sup>7</sup> to be necessary to describe OPMA data in  $\text{HgCdTe}$  and are not significant for TPMA, we obtained a consistent description of both sets of data by using a free exciton binding energy of 2 meV to describe the OPMA data.

Figure 10 shows the wavelength dependence of the PC response for sample #5 ( $x \simeq 0.280$ ). This figure depicts the most striking feature of TPMA in the  $\text{Hg}_{1-x}\text{Cd}_x\text{Te}$  alloy system: the two strong  $\sigma_L$  resonances as shown earlier for samples #1 and #2. In addition, at higher fields, weaker and broader resonances are seen which can not theoretically be described by TPMA processes. Instead, we interpret these resonances as resulting from electron transitions from near-midgap levels to the lowest conduction band Landau level. The transition energy versus magnetic field plots shown in Fig. 11 show excellent agreement between the experimental data and the calculated transition energies, confirming the TPMA and midgap level interpretation of the data. An energy gap of  $195.0 \pm 0.5$  meV is found, along with activation energies of 94 and 100 meV below the conduction band edge for the two midgap levels. The transition energies for the one photon midgap case are



described by  $\hbar\omega = E_c(0,B) - E_i$ , where  $E_i$  is the energy of a midgap level above the valence band. As  $B \rightarrow 0$ ,  $E_c(0,B) \rightarrow E_g$  and hence  $\hbar\omega \rightarrow E_g - E_i$ , the  $B = 0$  intercept.

Finally, in Fig. 12, we show the photoconductive response of sample #6 ( $x \approx 0.300$ ) for various  $\text{CO}_2$  laser wavelengths using left circular polarized light,  $\sigma_L$ . Once again, two strong  $\sigma_L$  TPMA transitions are observed as in the other samples. Other TPMA resonances are also seen at lower fields and are also attributed to transitions with selection rules associated with the  $\sigma_L$  polarization. Figure 13 shows the transition energy data and theoretical calculations giving good agreement with  $E_g = 225.0 \pm 0.5$  meV. TPMA spectra have also been seen in a p-type sample with  $x \approx 0.30$  that look quantitatively the same as the data shown in Fig. 12 for n-type samples.

### Summary

Two-photon magneto absorption structure has been observed and studied in a wide variety of samples of both n- and p-type HgCdTe. Our studies demonstrate the uniqueness and importance of TPMA methods as tools to characterize HgCdTe. For example, we have accurately determined the temperature dependence of the band gap and found distinct deviations from the Hansen, Schmit, Casselman relation with  $dE_g/dT \rightarrow 0$  below 20K.

Finally, these laser based studies have allowed the observation of impurity (or defect)-to-conduction band transitions from midgap levels and transitions from shallow acceptors to the conduction band.

### Acknowledgements

We acknowledge the support of this work by the U. S. Army Center for Night Vision and Electro-Optics, Contract #DAAB07-87-C-FO94.

### References

- \* Current address: National Institute of Standards and Technology, Materials Technology Group, Semiconductor Electronics Division, Center for Electronics and Electrical Engineering, Gaithersburg, Maryland 20899.
- 1. D. G. Seiler, S. W. McClure, R. J. Justice M. R. Loloee, and D. A. Nelson, Appl. Phys. Lett. 48, 1159 (1986).
- 2. D. G. Seiler, S. W. McClure, R. J. Justice, M. R. Loloee, and D. A. Nelson, J. Vac. Sci. Technol. A4, 2034 (1986).
- 3. C. L. Littler, D. G. Seiler, R. Kaplan, and R. J. Wagner, Phys. Rev. B27, 7473 (1983).
- 4. D. G. Seiler and M. W. Goodwin, J. Appl. Phys. 53, 7505 (1982).
- 5. C. L. Littler, D. G. Seiler, R. Kaplan, and R. J. Wagner, Appl. Phys. Lett. 41, 880 (1982).
- 6. D. G. Seiler, K. H. Littler, and C. L. Littler, Semicond. Sci. Technol. 1, 383 (1986).
- 7. M. H. Weiler, in Semiconductors and Semimetals (Academic Press, New York, 1981), R. K. Willardson and A. C. Beer, editors, Vol. 16, p 119.
- 8. G. L. Hansen, J. L. Schmit, and T. N. Casselman, J. Appl. Phys. 53, 7099 (1982).
- 9. M. H. Kalisher, J. Crystal Growth 70, 369 (1984).
- 10. F. J. Bartoli, C. A. Hoffman, and J. R. Meyer, J. Vac. Sci. Technol. A4, 2047 (1986).
- 11. M. C. Chen and J. H. Tregilgas, J. Appl. Phys. 61, 787 (1987).
- 12. M. C. Chen and J. A. Dodge, Sol. State Commun. 53, 449 (1986).

Table I. Sample Properties and Magneto-Optical Results

Sample	Manufacturer Nominal Properties			TPA Data		Impurity or Defect Levels Observed
#	n(77K) (cm <sup>-3</sup> )	$\mu$ (77K) (cm <sup>2</sup> /V.sec)	x	E <sub>g</sub> (meV) at 7K	x	
#1	1.4x10 <sup>14</sup>	1.6x10 <sup>5</sup>	0.2406 ±0.001	122.0 ±0.5	0.2364 ±0.0003	Residual acceptor 9.0 meV above valence band edge
#2	3.3x10 <sup>14</sup>	8.2x10 <sup>4</sup>	0.2450 ±0.0017	136.0 ±0.5	0.2448 ±0.0003	Residual acceptor 10.4 meV above valence band edge
#3	2.8x10 <sup>14</sup>	1.2x10 <sup>5</sup>	--	146.0 ±0.5	0.2508 ±0.0003	--
#4	1.0x10 <sup>14</sup>	7.6x10 <sup>4</sup>	0.2595 ±0.0015	156.0 ±0.5	0.2567 ±0.0003	--
#5	1.4x10 <sup>14</sup>	6.6x10 <sup>4</sup>	0.277 ±0.001	195.0 ±0.5	0.2801 ±0.0003	Two closely spaced midgap levels seen at 94 and 100 meV above valence band edge
#6	9.9x10 <sup>13</sup>	5.3x10 <sup>4</sup>	0.2995 ±0.0035	225.0 ±0.5	0.2976 ±0.0003	--
#7	p-type 1.5x10 <sup>18</sup>	480	0.2945 ±0.0035	222.0 ±1.0	0.2964 ±0.0006	--

Table II. Two-Photon Magnetoabsorption Transition Assignments

Designation	Energy Level Transition	Polarization
$\pi_1$	$a^+(0) \rightarrow a^c(0)$	$\sigma$ or $\pi$
$L_1$	$a^+(-1) \rightarrow a^c(1)$	$\sigma_L$
$\pi_2$	$a^-(1) \rightarrow a^c(1)$	$\sigma$ or $\pi$
$\pi_3$	$b^-(1) \rightarrow b^c(1)$	$\sigma$ or $\pi$
$L_2$	$b^+(-1) \rightarrow b^c(1)$	$\sigma_L$
$\pi_4$	$b^+(0) \rightarrow b^c(0)$	$\sigma$ or $\pi$
$\pi_5$	$a^-(2) \rightarrow a^c(2)$	$\sigma$ or $\pi$
$\pi_6$	$b^-(2) \rightarrow b^c(2)$	$\sigma$ or $\pi$
$L_3$	$a^+(0) \rightarrow a^c(2)$	$\sigma_L$
$\pi_7$	$a^+(1) \rightarrow a^c(1)$	$\sigma$ or $\pi$
$\pi_8$	$a^-(3) \rightarrow a^c(3)$	$\sigma$ or $\pi$
$L_4$	$b^+(0) \rightarrow b^c(2)$	$\sigma_L$
$L_5$	$a^-(2) \rightarrow a^c(2)$	$\sigma_L$
$L_6$	$b^-(2) \rightarrow b^c(2)$	$\sigma_L$

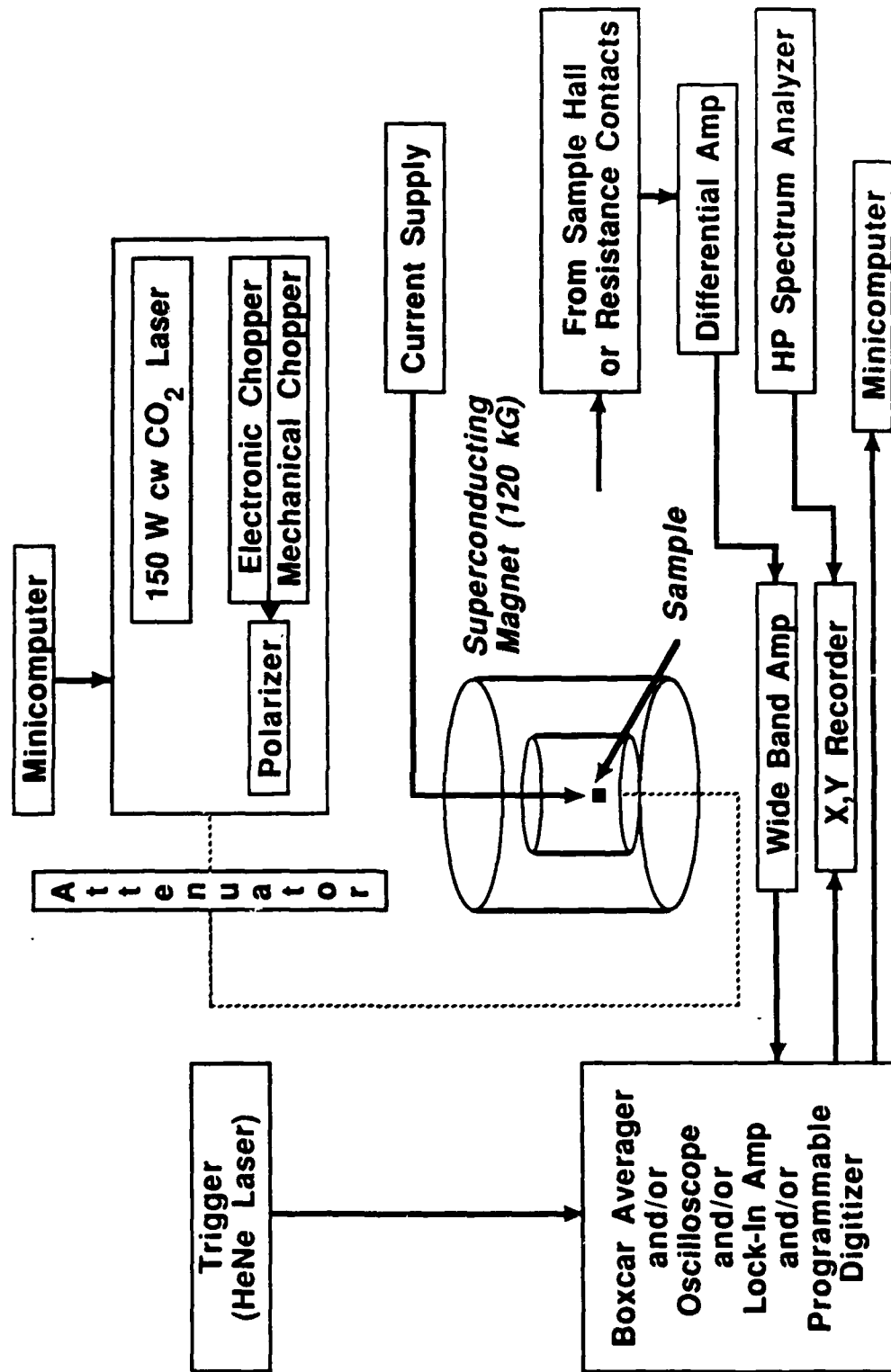


Figure 1. Schematic diagram of magneto-optical experimental apparatus.

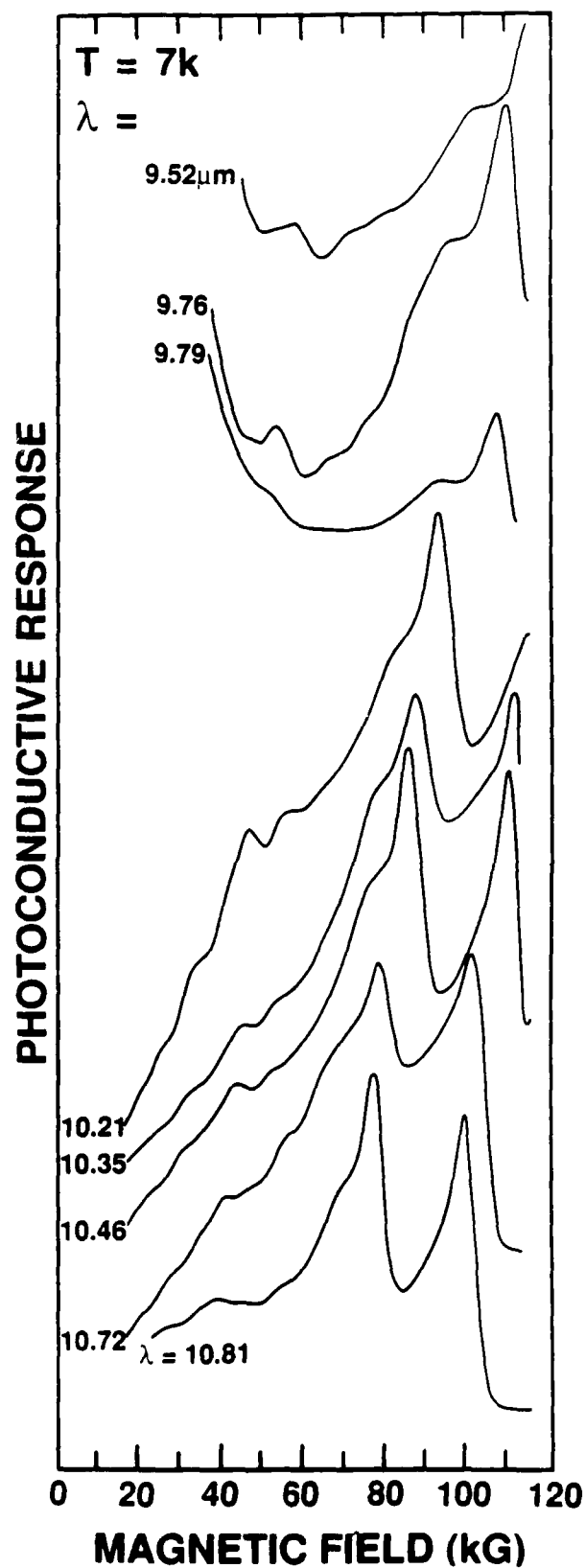


Figure 2. Wavelength dependence of the photoconductive response for an n-type sample #2 with  $x \approx 0.245$ . The two large resonances at high field arise from two-photon absorption processes. Unpolarized light was used.

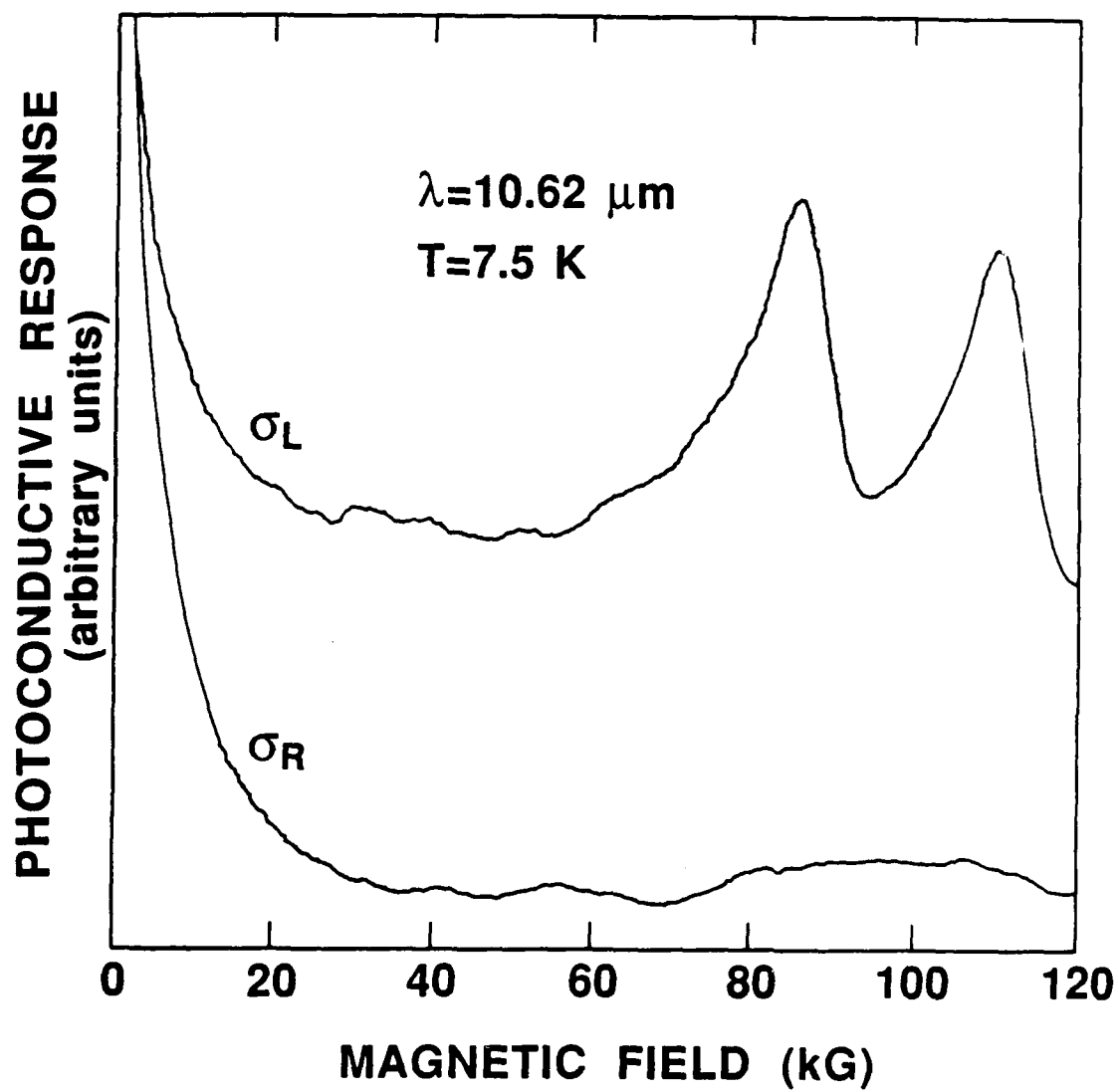


Figure 3. Polarization dependence of the photoconductive response for sample #2. Note that only the magnetic field direction was reversed upon going from  $\sigma_L$  (left) to  $\sigma_R$  (right) circular polarization.

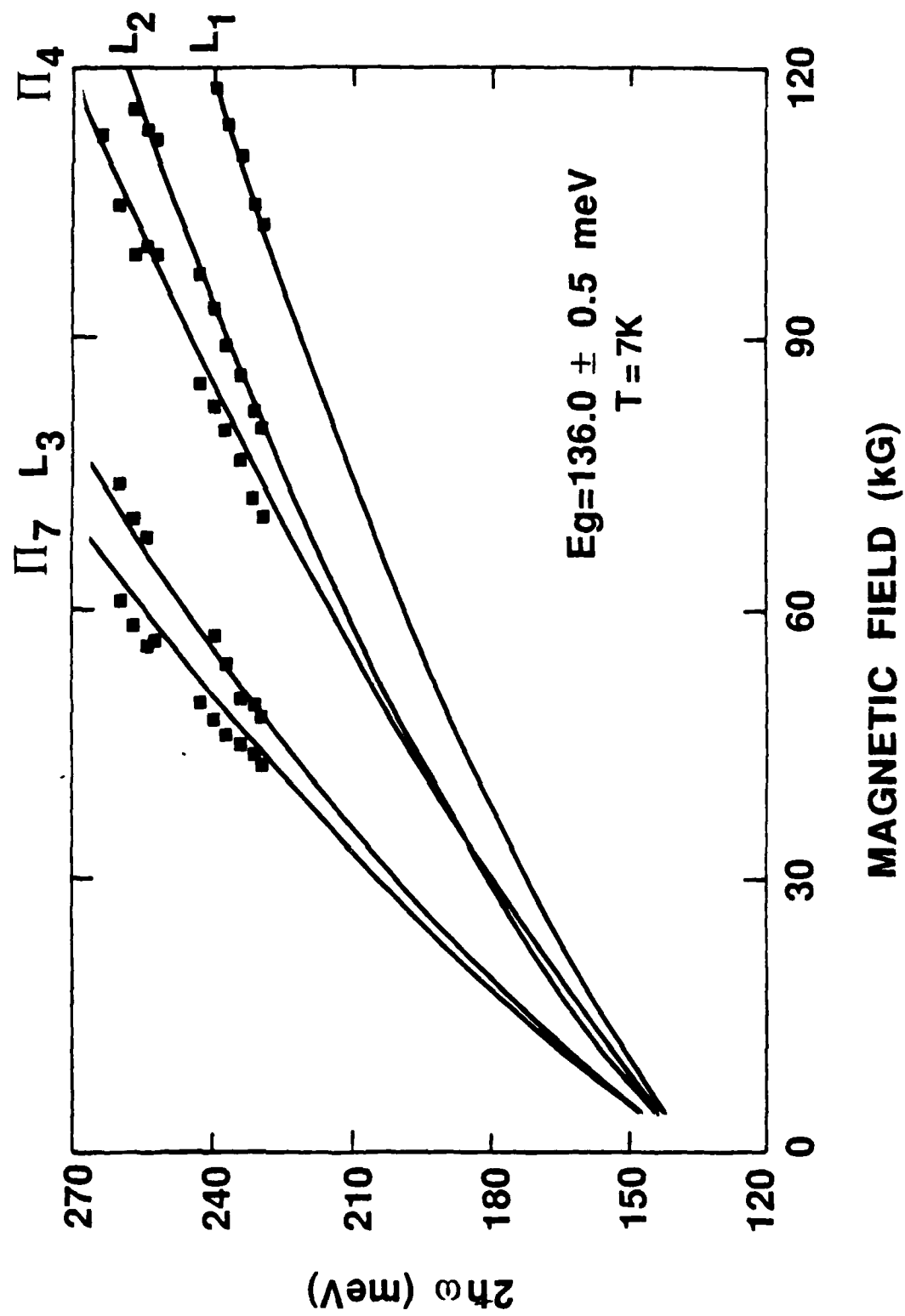


Figure 4. Transition energy vs. magnetic field for sample #2 ( $x \approx 0.245$ ). The energy gap is 136.0 meV.



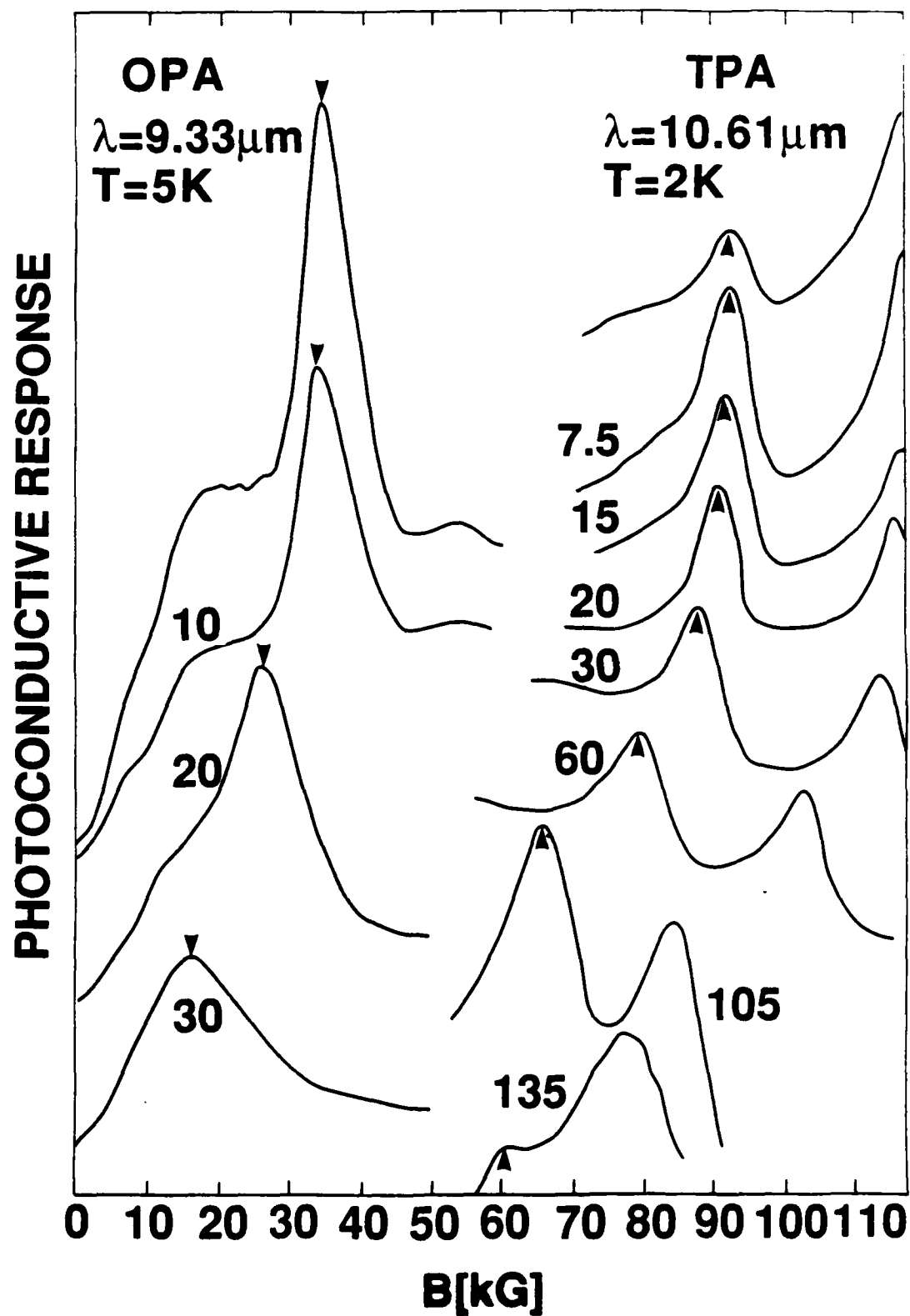


Figure 5. Temperature dependence of the photoconductive response of sample #1 ( $x \approx 0.236$ ).

# **Eg vs. Temperature** **HgCdTe $x=.239$**

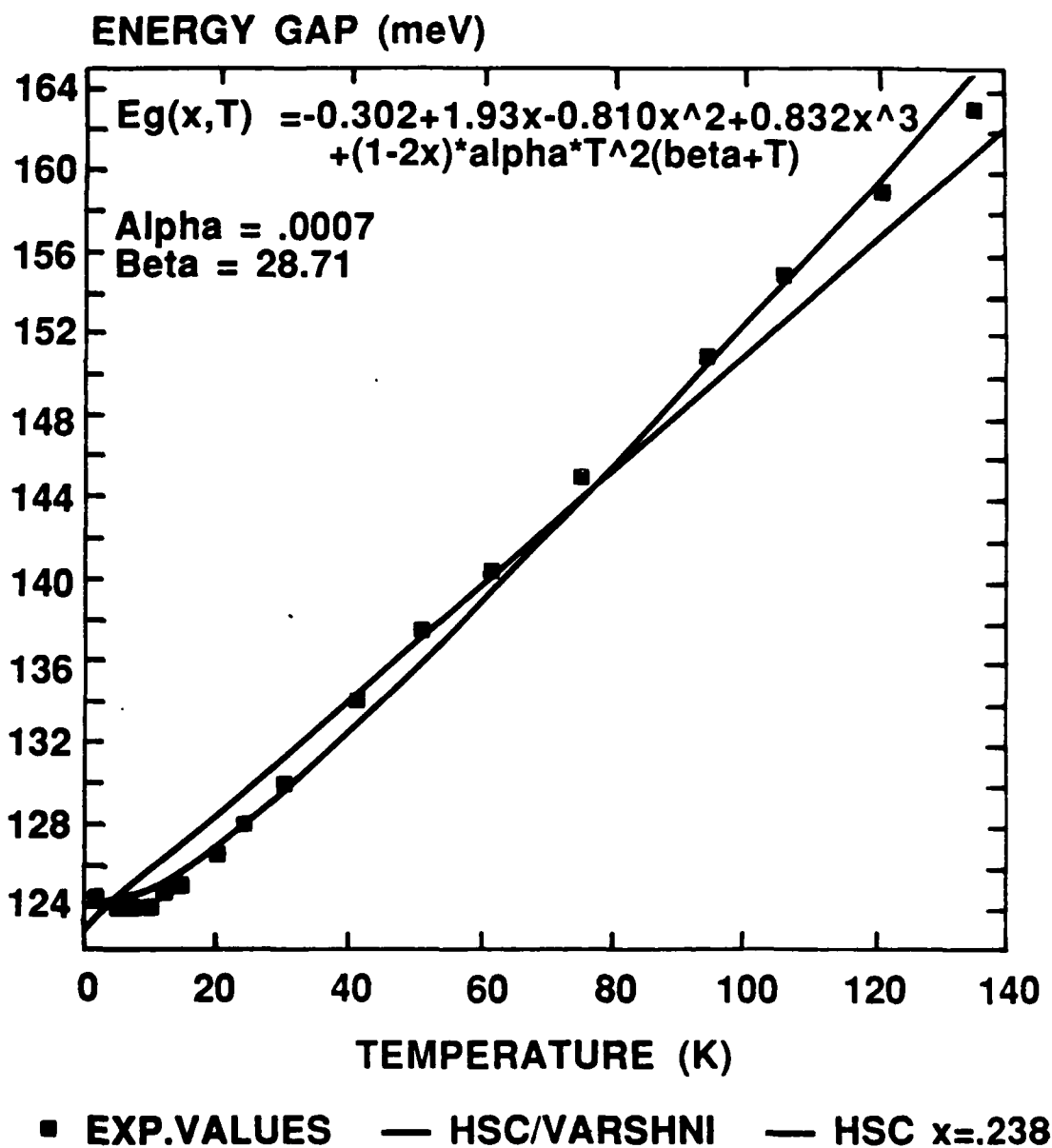


Figure 6. Energy gap vs. temperature for sample #1 ( $x \approx 0.236$ ). Note the "flattening" at low temperatures.

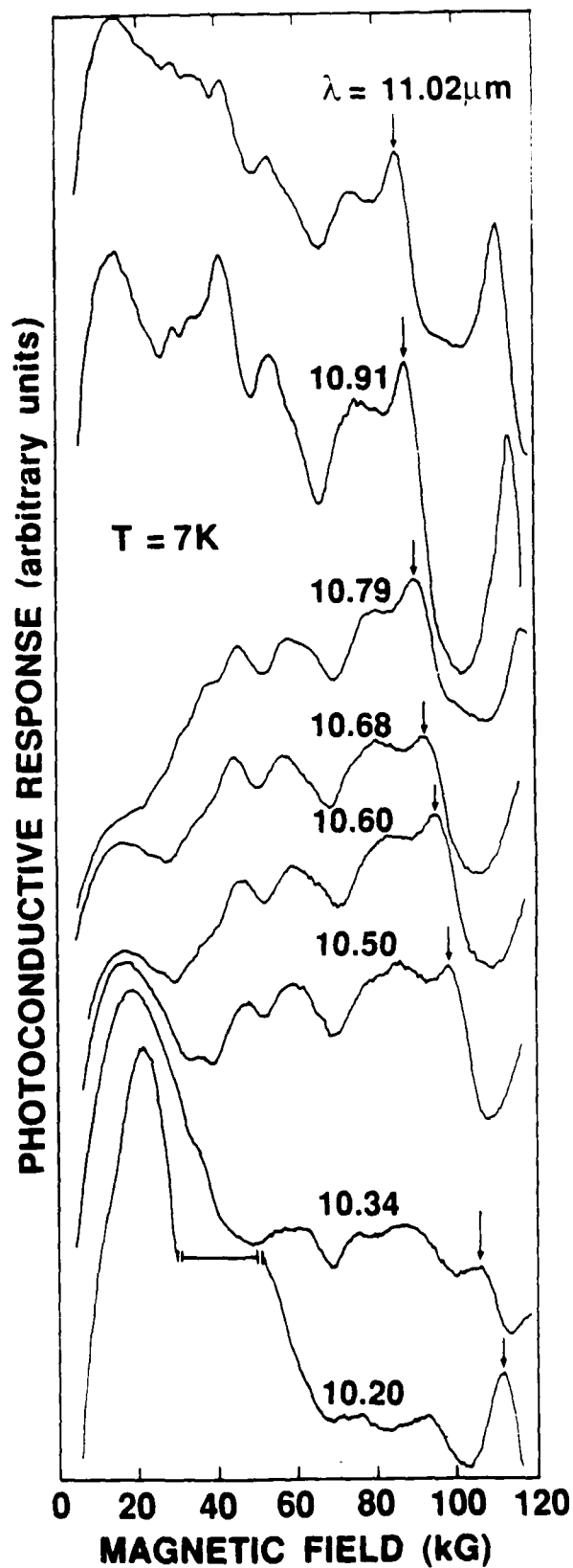


Figure 7. Photoconductive response at high laser intensities for sample #1 ( $x \approx 0.236$ ). The arrow shows how a TPMA resonance shifts with photon energy. Note unusual, wavelength independent structure observed for  $\lambda = 10.34$  to  $10.79\mu\text{m}$ .

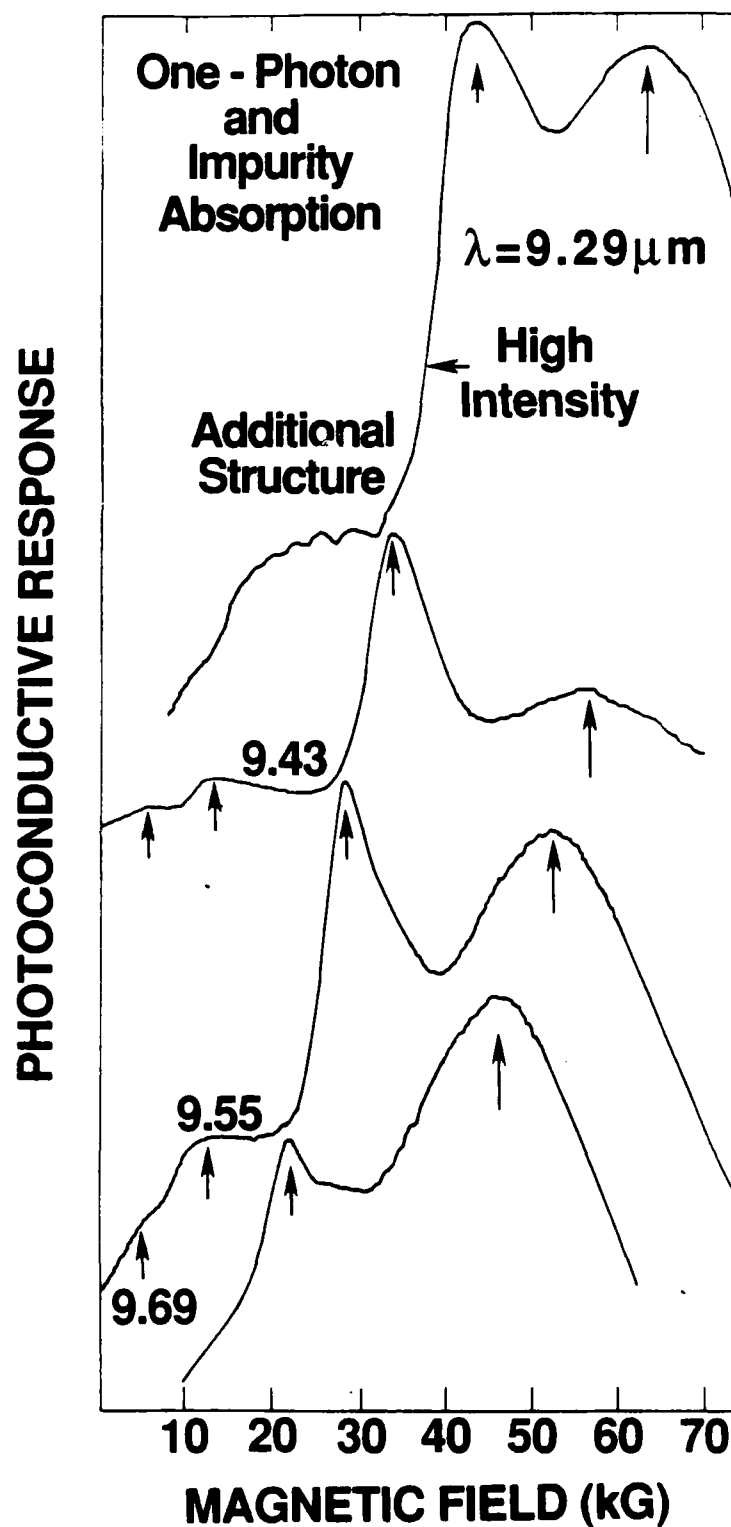


Figure 8. Intensity dependence of the photoconductive response for sample #1 showing three types of structure: (1) short arrows denote one-photon magnetoabsorption resonances, (2) long arrows, acceptor level to lowest conduction band Landau level, and (3) the additional, high intensity structure attributed to magneto-impurity resonances.

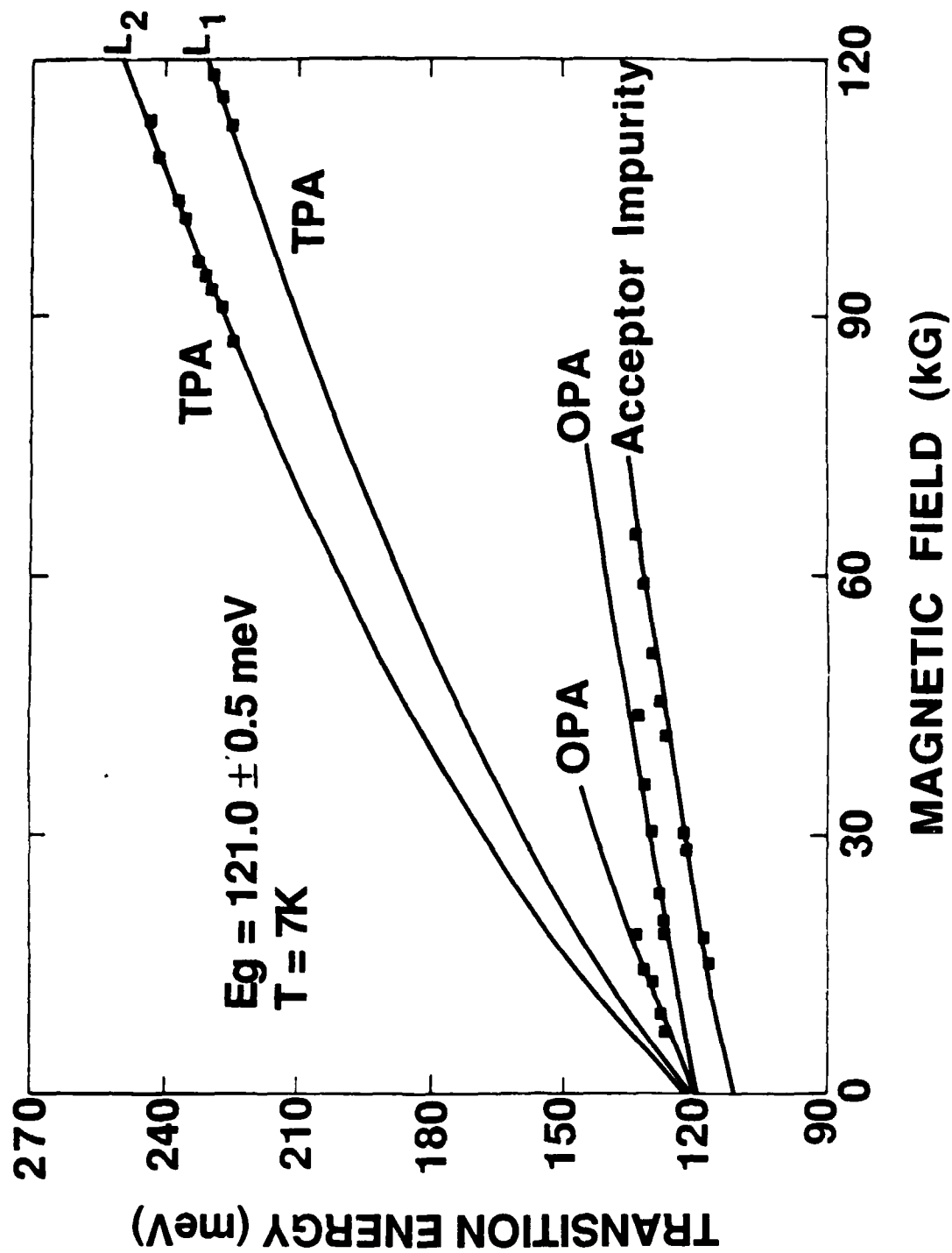


Figure 9. Transition energy vs. magnetic field showing one-photon (OPA), two-photon (TPA), and acceptor impurity behavior for sample #1. The  $x$ -value is obtained from the Hansen, Schmit, Casselman relation (Ref. 8) at 7 K using the TPMA determined gap.

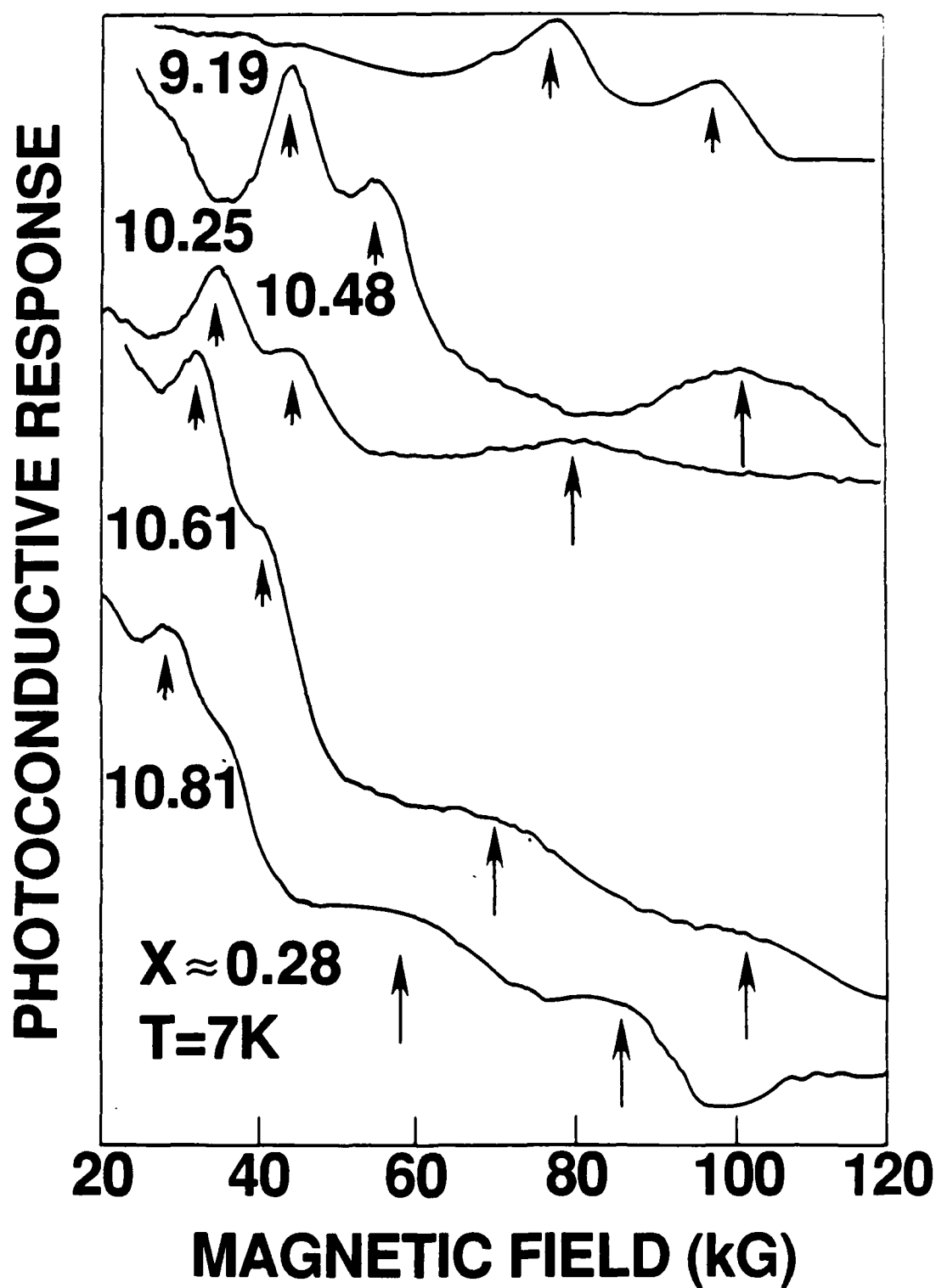


Figure 10. Wavelength dependence of the photoconductive response for sample #5 ( $x \approx 0.28$ ).

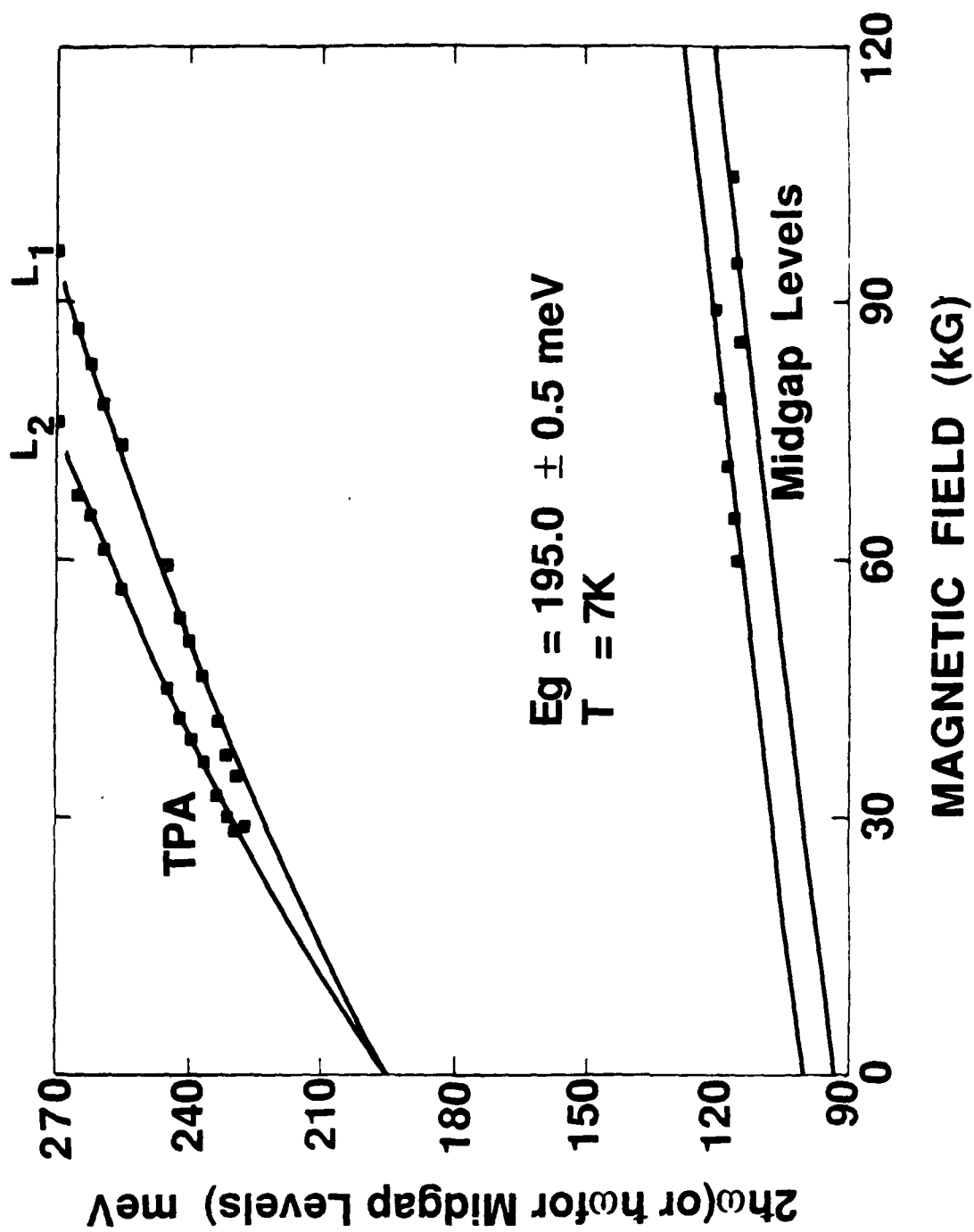


Figure 11. Transition energy vs. magnetic field showing two-photon (TPA) and midgap level transitions for sample #5 ( $\kappa \approx 0.280$ ).

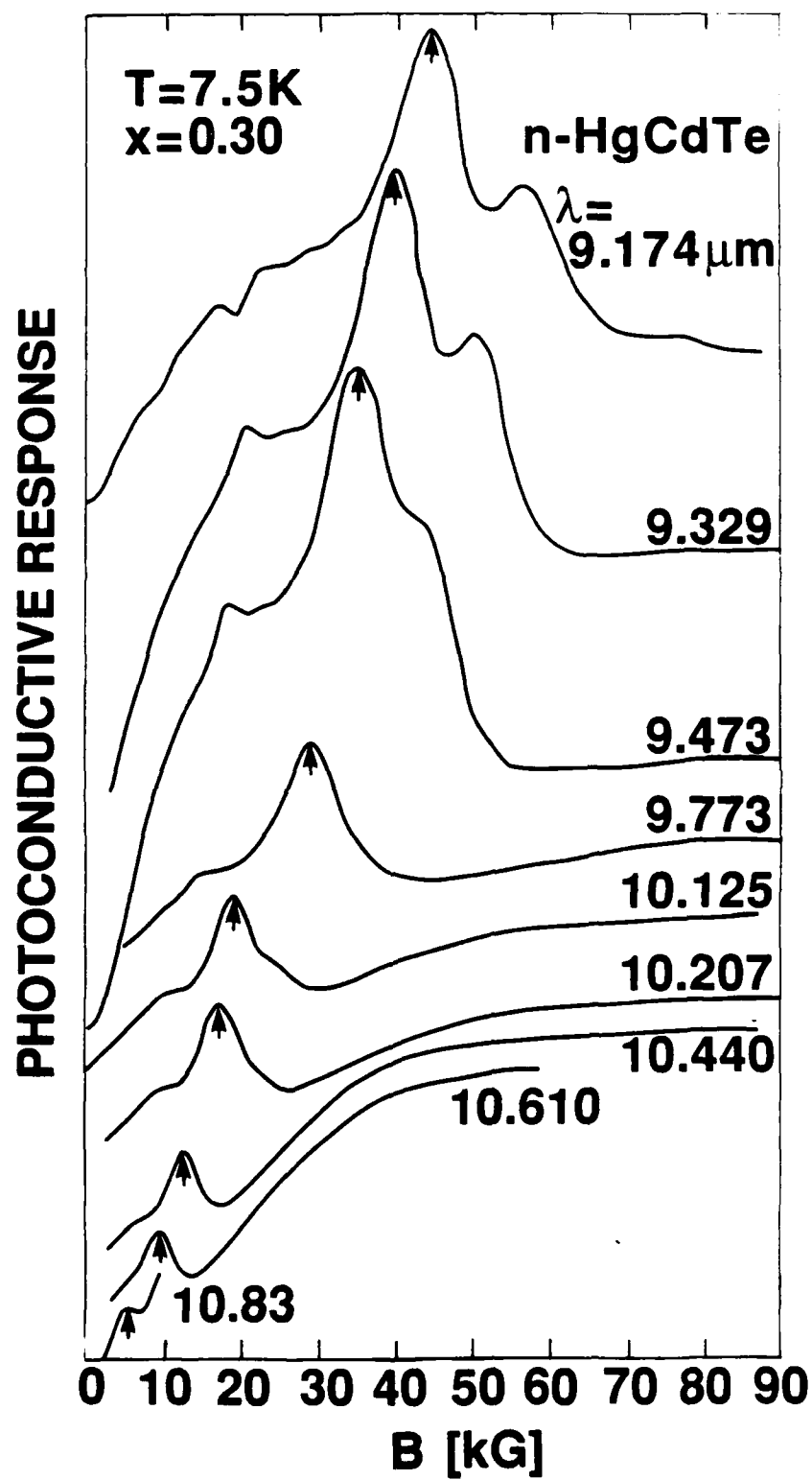


Figure 12. Wavelength dependence of the photoconductive response for sample #6 ( $x \approx 0.300$ ) using  $\sigma_L$  (left circular polarized) laser light.



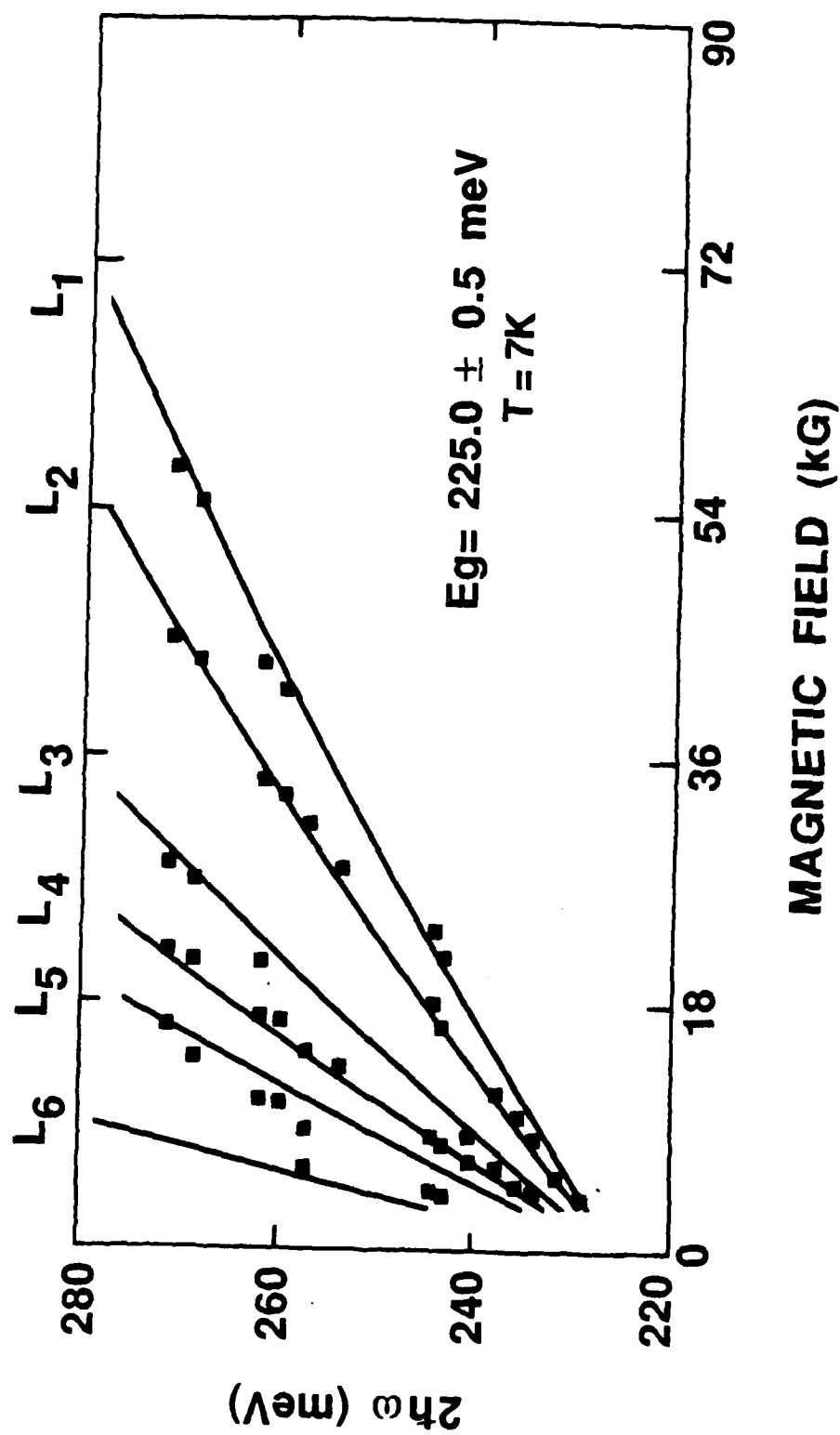


Figure 13. Transition energy vs. magnetic field for sample #6 ( $x \approx 0.300$ ). The band gap is determined to be 225.0 meV.